Probing Quantum Thermalization and Localization in Bose-Hubbard Systems

Antonio Rubio Abadal

München 2020

Probing Quantum Thermalization and Localization in Bose-Hubbard Systems

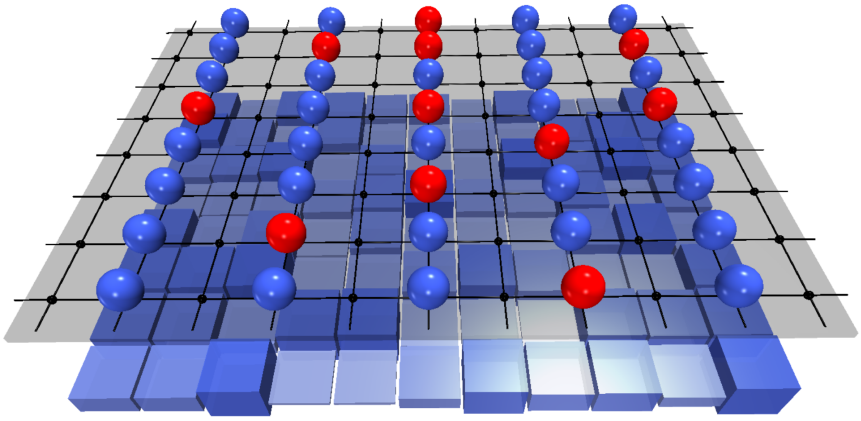

Dissertation an der Fakultät für Physik
der Ludwig–Maximilians–Universität München

vorgelegt von

Antonio Rubio Abadal

geboren in Palma, Spanien

München, April 2020

Erstgutachter:
Prof. Immanuel Bloch

Zweitgutachter:
Prof. Norman Yao

Weitere Prüfungskomissionmitglieder:
Prof. Ulrich Schollwöck, Prof. Dieter Braun

Tag der mündlichen Prüfung:
23. Juni 2020

Zusammenfassung

Die experimentelle Kontrolle und Beobachtung von Quantenvielteilchensystemen ist durch das Aufkommen ultrakalter Quantenmaterie Realität geworden. Das hohe Maß an Isolation in diesen Experimenten, zusammen mit der Entwicklung neuartiger Messmethoden, hat eine Grundsatzdebatte über die Thermalisierung in isolierten Quantensystemen, die "Quantenthermalisierung", wieder aufleben lassen. In dieser Doktorarbeit nutzen wir ein Quantengasmikroskop um die Thermalisierungsdynamik in hochgradig isolierten Systemen ultrakalter bosonischer Atome zu erforschen. Die Fähigkeit, Quantensysteme hunderter Atome zu realisieren und zu kontrollieren, ermöglicht die Untersuchung von Prozessen, die eine Herausforderung für klassische numerische Simulationen darstellen.

Einer der Hauptteile dieser Dissertation behandelt Bose-Hubbard-Systeme in Gegenwart von Unordnung. Wir beginnen mit einer Untersuchung der mikroskopischen Eigenschaften der Phasen nahe dem Gleichgewicht. Durch eine kontrollierbare Stärke der Unordnung beobachten wir Merkmale, die vereinbar mit der Entstehung einer sogenannten Bose-Glas Phase sind. Anschließend realisieren wir Zustände fern vom Gleichgewicht und untersuchen deren Quantenvielteilchendynamik. Insbesondere beobachten wir hierbei Hinweise für das Phänomen der "Vielteilchenlokalisierung", eine Ausnahme der Quantenthermalisierung. Darüber hinaus untersuchen wir, ob die Kopplung an ein Wärmebad mit nur wenigen Freiheitsgraden, d.h. ein Quantenbad, einen lokalisierten Zustand thermalisieren kann. Hierfür realisieren wir eine Mischung zweier wechselwirkender atomarer Spezien, wobei eine als Bad, und die andere als lokalisierendes System agieren. Wir beobachten delokalisierende Dynamik für ein ausreichend großes Bad, wobei Lokalisierungsmerkmale bei schwacher Kopplung für extrem lange Zeiten überleben können.

Der zweite Schwerpunkt dieser Doktorarbeit ist die Thermalisierung von periodisch getriebenen Vielteilchensystemen, die sogenannte Floquet-Thermalisierung. In diesen Systemen gilt keine Energieerhaltung, was jeden Anfangszustand irgendwann in einen Zustand unendlicher Temperatur uberführt. Für ausreichend hohe Frequenzen kann dieser Thermalisierungsprozess beliebig lange dauern, was die Realisierung exotischer, langlebiger, prethermischer Zustände erlaubt. Die experimentelle Untersuchung dieser Zustände wird in unserem System durch den hohen Grad an Isolation und die Sensitivität der Quantengasmikroskopie ermöglicht. Dadurch können wir die Heizraten für ein weites Spektrum an Antriebsfrequenzen und Wechselwirkungsstärken messen. Unsere Ergebnisse zeigen eine starke Unterdrückung der Heizraten mit ansteigender Antriebsfrequenz, welche konsistent sind mit den theoretischen Erwartungen.

Abstract

The experimental control and observation of quantum many-body systems has become a reality with the advent of ultracold quantum matter. The high level of isolation of these experiments, together with the development of novel measurement techniques, has revived a fundamental debate concerning the thermal equilibration of isolated quantum systems, commonly named "quantum thermalization". In this thesis we make use of a quantum-gas microscope to explore the thermalizing dynamics of highly isolated systems of ultracold bosonic atoms in optical lattices. The ability to prepare and control quantum systems made up of hundreds of atoms makes it possible to explore regimes that represent a challenge for classical numeric simulations.

A major part of this dissertation deals with Bose-Hubbard systems in the presence of quenched disorder. We begin by studying the microscopic properties of its phases near equilibrium, where by tuning the strength of the disorder, observe features consistent with the emergence of a so-called Bose-glass phase. We then continue by preparing states far from equilibrium and exploring their quantum many-body dynamics. In particular, we observe signatures of the phenomenon of "many-body localization", which implies a breakdown of quantum thermalization. In addition, we study whether localized systems can be thermalized via the coupling to a bath of few degrees of freedom, i.e. a quantum bath. We do so by preparing a mixture of two interacting atomic species, where one acts as the bath and the other as the localized system. We do observe delocalizing dynamics for large enough baths, though in regimes of weak coupling localization can survive for extremely long times.

The second main topic of this thesis is the thermalization of periodically driven many-body systems, so-called Floquet thermalization. In these systems, the absence of energy conservation eventually brings any initial state into a featureless infinite-temperature one. However, for sufficiently high frequencies this thermalization process can take arbitrarily long times, which can enable the engineering of exotic long-lived prethermal states. We use the high isolation of our system, together with the high sensitivity of quantum-gas microscopy, to measure the heating rates for a range of driving frequencies and interaction regimes. Our results show a dramatic suppression of the heating as the frequency of the drive is increased, which is consistent with theoretical expectations.

Contents

A tota la meva família

Chapter 1
Introduction

The last three decades have witnessed how ultracold atoms have extended from the field of atomic physics onto the one of condensed matter. The low temperatures at which dilute atomic gases can be cooled, enable the study of many-body properties emerging from their intrinsic quantum statistics. Beginning with the milestone of atomic Bose-Einstein condensates [1, 2], a series of developments have extended our understanding of bosonic as well as fermionic degenerate quantum gases [3].

The landmark achievement of bringing quantum gases into the strongly correlated regime was enabled by the implementation of many novel experimental tools. In particular, by loading ultracold atoms into optical lattices, i.e. dipole potentials based on interfering laser beams, one can reach a strong confinement and an enhancement of the atomic interactions. This has allowed for the realization of low-dimensional systems [4–6] as well as lattice models such as the Bose- and the Fermi-Hubbard [7, 8]. In addition, recent progress in combining cooling and imaging techniques has led to the arrival of *quantum-gas microscopy*. This enables one to resolve at the single-atom level the occupations in the lattice sites of two-dimensional systems of bosons [9, 10] or fermions [11–14]. These microscopes have made it possible to measure density correlations [15] as well as spin correlations, essential for the study of quantum magnetism [16–18]. The opportunity of experimentally realizing fundamental models of condensed matter, together with the high degree of control and tunability in these systems, has put them in the frontier of analog quantum simulation [19–21].

While many of these experimental studies have focused on the study of ground-state properties and phases of matter, one can go one step further and explore *out-of-equilibrium dynamics* [22] as well. By performing a quench in the system, one can subsequently track its complex many-body dynamics. Two landmark experiments in this field are the observation of coherent collapse and revival dynamics [23] and of momentum-space oscillations in a 1D Bose gas [24]. A vast amount of experiments have followed soon after in distinct quantum-gas setups, as for example the dynamics of ferromagnetic spinor condensates [25], the relaxation of density waves [26] and phase coherence [27], coherent oscillations in Ising models [28] or the decay of spin waves in Heisenberg models [29].

Some of these experiments display an almost perfect isolation from their environment, which has sparked discussion on many fundamental topics concerning the equilibration of isolated quantum systems [30–33]. While in the absence of an external heat bath it might seem unlikely for a system to locally reach thermal equilibrium, the coupling of small subsystems with the rest of the system can resemble the coupling to an effective reservoir [34]. The developments of these and many other ideas have pushed forward the field of *quantum thermalization*, with major new concepts like the *eigenstate thermalization hypothesis* [35–38], which implies that the individual many-body eigenstates are, in a way, already thermal.

While most generic systems seem to follow this quantum version of thermalization, as also shown by experimental evidence [39], a failure of equilibration has been predicted in some disordered systems. The presence of quenched disorder is known to lead to a breakdown of transport properties [40], which has been shown to survive even in the presence of finite interactions [41, 42]. This phenomenon, dubbed *many-body localization* (MBL), has lately attracted much attention, in part due to its incompatibility with quantum statistical mechanics, but also as a path to enable the realization of ordered phases out of equilibrium [34].

In experiments with ultracold atoms, disorder can be implemented by the generation of random or quasiperiodic dipole potentials, which makes them great candidates for the study of the non-ergodic phenomenon of MBL. So far, several studies have looked at interacting disordered gases in one-dimensional [43–45] as well as in higher-dimensional systems [46–48]. Many of these experiments have shown signatures of localization, mostly based on transport properties, for sufficiently strong disorder. A major part of the present thesis will deal with experiments of disordered bosons in a two-dimensional square optical lattice.

A quite different scenario for the study of out-of-equilibrium dynamics is that of periodically driven systems, i.e. *Floquet* systems. This field has also captured much attention over the last few years, in part for the possibility of implementing phases of matter that would otherwise not exist in non-driven systems [49]. However, a constant exchange of energy with the drive eventually brings Floquet systems into an infinite-temperature state, a consequence of quantum thermalization. This hinders the realization of any long-lived exotic models. A solution can be found by considering Floquet MBL systems, which can stabilize such phases for indefinite times, by preventing the thermalization of the system. This approach is, however, restricted to models with some specific conditions, such as the presence of disorder or the interaction range. A different path is that opened by *Floquet prethermalization*, namely the suppression of the thermalization rates for high-frequency drives [50, 51]. This allows one to prepare exotic states for exponentially long times even in generic systems without disorder, and thereby prepare the preparation of prethermal phases of matter [52]. This phe-

nomenon will also be explored in this thesis, via the implementation of a periodically modulated lattice.

Outline of the thesis

In this thesis, a bosonic quantum-gas microscope has been used to explore some of the out-of-equilibrium phenomena discussed in the previous section, including many aspects that had been only explored theoretically until now.

In Part I we summarize the main ideas and tools that make it possible to microscopically study the Bose-Hubbard model in two dimensions. In Ch. 2 we introduce the Bose-Hubbard Hamiltonian together with its ground-state phases and phenomenology. We then show that it accurately describes the physics of ultracold bosonic atoms loaded in optical lattices. In Ch. 3 we describe our experimental setup, emphasizing the site-resolved imaging and addressability.

In Part II we focus on one of the core contents of the dissertation: the study of disordered many-body systems. We begin in Ch. 4 by introducing the ground-state phases of the disordered Bose-Hubbard model, and comparing previous experiment with our implementation of programmable quenched disorder. We observe how disorder induces the emergence of a compressible and non-superfluid state, consistent with a Bose glass phase. In Ch. 5 we shift into the field of out-of-equilibrium dynamics, and we introduce the theoretical basis behind the concepts of ergodicity, quantum thermalization and many-body localization, which are experimentally explored in the following two chapters. In Ch. 6 we start by introducing our scheme to generate far-from-equilibrium states, which is based on a quench of the optical lattice. We then present measurements of the quench dynamics for systems with increasing disorder strengths and also distinct prepared initial states. Based on the measurement of density imbalances, we identify dynamics compatible either with the thermalization of the system or many-body-localization. In Ch. 7 we address the question of whether a localized disordered system can thermalize via coupling to a thermal bath with few degrees of freedom. We do this by studying a mixture of two atomic species, in which one displays disorder-induced localization, while the other plays the role of a disorder-insensitive quantum bath. The results indicate that for large enough baths, an efficient delocalization of the system can take place, while for small sizes of the thermal component, localization remains even for the longest measured times.

Part III deals with the thermalization of driven (Floquet) quantum many-body systems. Ch. 8 summarizes the main ideas and motivation behind the study of periodically driven systems, and explains the emergence of Floquet thermalization, which eventually takes a driven system into a featureless infinite-temperature state. We then discuss how high-frequency drives can extend the lifetime of such driven systems be-

fore thermalization takes place, so-called Floquet prethermalization. Evidence of this phenomenon is experimentally observed in Ch. 9, in which we measure the heating dynamics of an atomic cloud under the periodic modulation of the optical lattices. The use of a sensitive thermometry technique allows us to identify an exponential-in-frequency suppression of the heating rates, the signature of Floquet prethermalization.

In a final chapter, we summarize the contents and results presented in this thesis and present an outlook, in which we discuss possible extensions of the experiments performed so far.

List of publications

The following articles have been published in refereed journals in the context of this thesis. The articles most relevant for this thesis are shown in bold font.

- ***Exploring the many-body localization transition in two dimensions.***
  J.-y. Choi, S. Hild, J. Zeiher, P. Schauß, A. Rubio-Abadal, T. Yefsah, V. Khemani, D. A. Huse, I. Bloch and C. Gross.
  Science **352**, 1547-1552 (2016).

- *Coherent many-body spin dynamics in a long-range interacting Ising chain.*
  J. Zeiher, J.-y. Choi, A. Rubio-Abadal, T. Pohl, R. v. Bijnen, I. Bloch and C. Gross.
  Phys. Rev. X **7**, 041063 (2017).

- ***Many-body delocalization in the presence of a quantum bath.***
  A. Rubio-Abadal, J.-y. Choi, J. Zeiher, S. Hollerith, J. Rui, I. Bloch and C. Gross.
  Phys. Rev. X **9**, 041014 (2019).

- *Quantum gas microscopy of Rydberg macrodimers.*
  S. Hollerith, J. Zeiher, J. Rui, A. Rubio-Abadal, V. Walther, T. Pohl, D. M. Stamper-Kurn, I. Bloch and C. Gross.
  Science **364**, 6441 (2019).

- ***Floquet prethermalization in a Bose-Hubbard system.***
  A. Rubio-Abadal, M. Ippoliti, S. Hollerith, D. Wei, J. Rui, S. L. Sondhi, V. Khemani, C. Gross and I. Bloch.
  Phys. Rev. X **10**, 021044 (2020).

In addition, the following article has been posted as an electronic preprint:

- *A subradiant optical mirror formed by a single structured atomic layer.*
  J. Rui, D. Wei, A. Rubio-Abadal, S. Hollerith, J. Zeiher, D. M. Stamper-Kurn, C. Gross and I. Bloch.
  arXiv:2001.00795 (2020).

Part I

Bose-Hubbard physics under a microscope

Chapter 2

The Bose-Hubbard model with ultracold atoms

The Hubbard model has become an essential tool in the description and understanding of many systems in the field of condensed matter physics [53]. In the context of ultracold atoms, its precise description of bosons and fermions in optical lattices has made it extremely common in both theoretical and experimental studies. In this chapter we define and describe the main properties of the Bose-Hubbard model, which are particularly relevant for the rest of the thesis. We will first go through the ground-state phases of the model and discuss basic out-of-equilibrium examples. Next, we will derive how ultracold atoms loaded in optical lattices can be described by the Bose-Hubbard model assuming only the lowest band is populated.

2.1 Basics of the Bose-Hubbard model

The Hubbard model was originally conceived as an approximate model for correlated electrons in solids. In essence, it can be seen as an interacting extension of the tight-binding model [54], which considers electrons solely in the surroundings of the ions of a crystal and their hopping through the ionic lattice. Its bosonic counterpart, the Bose-Hubbard (BH) model [55], was at first devised to describe superfluid helium in porous media, but its most common application has become the description of degenerate bosonic atoms in optical lattices [56].

In its simplest version, the BH Hamiltonian can be written in the formalism of second quantization as

$$\hat{H}_{\mathrm{BH}} = -J \sum_{\langle i,j \rangle} \hat{a}_i^\dagger \hat{a}_j + \frac{U}{2} \sum_i \hat{n}_i \left(\hat{n}_i - 1\right) - \mu \sum_i \hat{n}_i, \tag{2.1}$$

where the symbols $\hat{a}_i$, $\hat{a}_i^\dagger$ and $\hat{n}_i$ denote the bosonic annihilation, creation and number operators for a particle in the site at position $\boldsymbol{i}$. The first term describes the hopping between nearest-neighbour sites $\langle \boldsymbol{i}, \boldsymbol{j} \rangle$ with tunneling amplitude J, and the second term

the on-site interactions between two or more particles with interaction strength U. The last term includes the chemical potential μ, which fixes the number of bosons when assuming the grand-canonical ensemble. In most cases we will restrict ourselves to a fixed total boson number such that this term will remain unchanged in homogeneous systems.

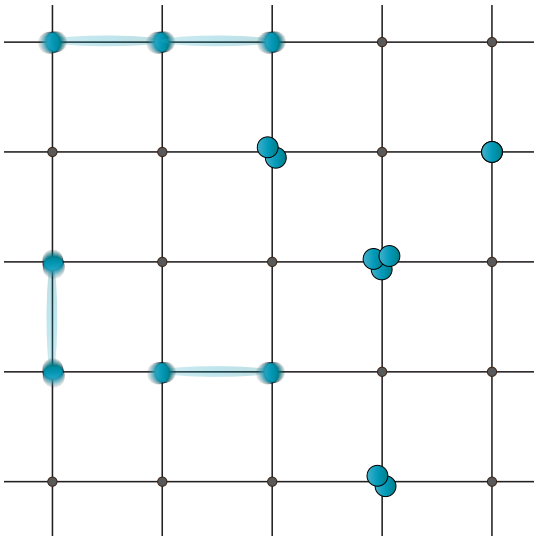

Figure 2.1: Cartoon depiction of the two-dimensional Bose-Hubbard model. Picture of a 5×5 lattice grid with few particles illustrating the tunneling of single particles and doubly and triply occupied sites.

2.1.1 Single-particle eigenstates

Before discussing any eigenstates of the BH model, it will be helpful to consider only the hopping term, i.e. the tight-binding model, $\hat{H}_{\mathrm{TB}} = \hat{H}_{\mathrm{BH}}(U = 0)$. Let us assume a lattice of arbitrary dimension with a total number of lattice sites M, for which we can express the state of a single boson localized in an individual site as

$$|\boldsymbol{j}\rangle = \hat{a}_{\boldsymbol{j}}^{\dagger} |0\rangle, \tag{2.2}$$

where $|0\rangle$ denotes the vacuum state, i.e. an empty lattice. The single-particle eigenstates of $\hat{H}_{\mathrm{TB}}$ can be written in this basis of localized bosons as an equally weighted superposition with a relative phase,

$$|\boldsymbol{q}\rangle = \hat{a}_{\boldsymbol{q}}^{\dagger} |0\rangle = \frac{1}{\sqrt{M}} \sum_{\boldsymbol{j}} e^{i\boldsymbol{q}\cdot\boldsymbol{r}_{\boldsymbol{j}}} |\boldsymbol{j}\rangle, \tag{2.3}$$

where $\boldsymbol{q}$ is the so-called lattice momentum, a vector where each component q_l can be considered a quantum number, and $\boldsymbol{r}_j$ the position vector of each lattice site. The components of the lattice momentum can take values $q_l \in [-\pi/a, +\pi/a]$, where a is the lattice spacing (here we assume it to be the same for all l directions).

These $|\boldsymbol{q}\rangle$ are the lattice periodic Bloch states [54], and to directly see that they are the eigenstates of the system, we can act with the Hamiltonian from the left, obtaining the energy eigenvalues

$$\hat{H}_{\mathrm{TB}} |\boldsymbol{q}\rangle = -2J \sum_l \cos(q_l\, a)\, |\boldsymbol{q}\rangle. \tag{2.4}$$

This expresssion directly indicates that for the non-interacting case, the energy bandwidth for d dimensions will be given by $E_{\mathrm{BW}} = 2zJ$, where $z = 2d$ is the coordination number, i.e. the number of nearest neighbours.

2.1.2 Phases in the ground state

Simple as it is, the BH model displays many interesting physical features. A fundamental one is the appearance of a quantum phase transition (QPT), that is a change in the ground-state phase as one parameter of the Hamiltonian is tuned [57]. By tuning the ratio of the BH parameters J/U, the ground state displays a transition between a superfluid and an insulating phase.

Superfluid phase

Let us start in the regime of extremely weak interactions ($U \ll J$). The ground state is essentially a Bose-Einstein condensate in the lowest energy state, i.e. a product of single-particle Bloch states at $\boldsymbol{q} = 0$,

$$|\Psi_{\mathrm{SF}}\rangle = \frac{1}{\sqrt{N!}} \left(\hat{a}^\dagger_{\boldsymbol{q}=0}\right)^N |0\rangle = \frac{1}{\sqrt{N!}} \left(\frac{1}{\sqrt{M}} \sum_j \hat{a}^\dagger_j\right)^N |0\rangle, \tag{2.5}$$

where N is the total number of bosons. For large M and N, the superfluid state can also be written as a product of single-site coherent states

$$|\Psi_{\mathrm{SF}}\rangle = \prod_j |\alpha\rangle_j = \prod_j \left(e^{-|\alpha|^2/2} \sum_{n=0}^{\infty} \frac{\alpha^n}{\sqrt{n!}} |n\rangle_j\right), \tag{2.6}$$

in which $\alpha = \sqrt{\frac{N}{M}}$, and $|n\rangle$ is a single-site Fock state, i.e. an eigenstate of $\hat{n}_i$, with n bosons. This leads to a Poissonian on-site number distribution $p(n) = \alpha^{2n}\, e^{-\alpha^2}/n!$ with mean occupation $\alpha^2 = N/M$ and equal to its variance $\sigma^2 = N/M$.

Additionally, it can be shown that the state $|\Psi_{\mathrm{SF}}\rangle$ displays off-diagonal long-range order, given by finite first-order correlation $\langle \hat{a}_j^\dagger \hat{a}_k \rangle > 0$ when $|\boldsymbol{r}_j - \boldsymbol{r}_k| \to \infty$. This is precisely the order parameter that identifies the superfluid phase.

Mott insulator

We now turn to the opposite parameter regime, in which the tunneling is negligibly small compared to the single-site interaction ($J \ll U$). In this limit, the ground state for a system with commensurate filling n is

$$|\Psi_{\mathrm{MI}}\rangle = \prod_j |n\rangle_j = \frac{1}{\sqrt{n!}} \prod_j \left(\hat{a}_j^\dagger\right)^n |0\rangle, \tag{2.7}$$

in which each particle is restricted to an individual lattice site, and therefore the variance is $\sigma_i^2 = 0$. This describes an insulating phase and is called the Mott insulator. The expectation value of the field operator is $\langle \hat{a}_j \rangle = 0$ and thereby it has vanishing long-range order.

While the vanishing variance might seem as a suitable order parameter, note that $|\Psi_{\mathrm{MI}}\rangle$ only describes the ground state in the atomic limit. For small but finite values of the tunneling J, the ground state is instead given by

$$|\Psi^{(1)}\rangle \approx |\Psi_{\mathrm{MI}}\rangle + \frac{J}{U} \sum_{\langle i,j \rangle} \hat{a}_i^\dagger \hat{a}_j |\Psi_{\mathrm{MI}}\rangle, \tag{2.8}$$

for which $\sigma_i^2 > 0$. The order parameter for the Mott insulator is therefore instead given by the local compressibility $\kappa_i \propto d\langle \hat{n}_i \rangle / d\mu$, which has a vanishing value $\kappa_i = 0$ in the Mott insulator phase, i.e. it is an incompressible phase. Note also that $|\Psi^{(1)}\rangle$ has a finite short-range coherence, originating from particle-hole pairs, i.e. the additional term in Eq. 2.8 [58, 59].

Another useful way of understanding the properties of these two distinct phases, in the context of quantum optics, is by considering their uncertainty in the phase of each site ϕ_i due to the well-defined atom number n_i. These are expected to fulfill the phase-number uncertainty relation $\Delta n_i \, \Delta \phi_i \geq 1/2$. In the case of the Mott insulator, the fixed boson number per site leads to a high uncertainty in the phase of the single-site matter field. In the superfluid, the phases of each site are well defined, due to the high fluctuations in the particle number, and in addtion, the tunneling between the different sites locks all the phases to each other, leading to the characteristic long-range coherence [60].

2.1.3 Quench dynamics

Let us now go beyond the physics of individual eigenstates and consider few examples of out-of-equilibrium dynamics that can be explored within the BH model. The main process behind non-equilibrium quantum systems is the introduction of a quench in the system, i.e. a sudden change of a Hamiltonian parameter, which projects an initial state into a superposition of eigenstates of the final Hamiltonian. This will typically lead to non-trivial dynamics that can involve many eigenstates from a certain part of the energy spectrum. In the BH case, this will be a quench of the tunneling and/or the interactions.

Coherent collapse and revival

Let us consider the preparation of a coherent state as described in Eq. 2.6, e.g. by preparing a superfluid, and suddenly quench the tunneling strength to zero, such that the time evolution will only be given by the interaction part of the Hamiltonian $\hat{H}_{\mathrm{BH}}(J = 0)$. This will lead to a trivial time-evolution of each one of its single-site eigenstates $|n\rangle$ as

$$|n(t)\rangle = e^{-i\hat{H}t/\hbar}\,|n\rangle = e^{-iUn(n-1)t/2\hbar}\,|n\rangle, \tag{2.9}$$

and therefore to a time evolution of the initial single-site coherent state given by

$$|\alpha(t)\rangle = e^{-i\hat{H}t/\hbar}\,|\alpha\rangle = e^{-|\alpha|^2/2}\sum_{n=0}^{\infty}\frac{\alpha^n}{\sqrt{n!}}\,e^{-iUn(n-1)t/2\hbar}\,|n\rangle. \tag{2.10}$$

The dynamics of this state will first lead to a dephasing of the different $|n\rangle$ states, such that the coherence will quickly collapse. Later on, for multiples of the timescale $t_{\mathrm{rev}} = h/U$, all phase factors will be multiples of 2π, leading to a full revival of the coherence.

An experimental realization of such out-of-equilibrium dynamics has been performed with ultracold atoms in optical lattices [23, 61].

Quantum walk in real space

Let us now consider the opposite scenario of the quench described above. We prepare a single-site Fock state, e.g. beginning from a Mott insulator, and quench the tunneling to a finite value J, while the interaction U is fixed to zero. For simplicity we will assume a one-dimensional system with a single particle at site j, which can be written as $|j\rangle = |n = 1\rangle_j$, consistent with the nomenclature used in Sec. 2.1.1. The time evolution will then be given by the tight-binding Hamiltonian, and since $\hat{H}_{\mathrm{TB}}$ is diagonal in the basis of Bloch states $|q\rangle$, we should reexpress $|j\rangle$ in terms of those as

$|j\rangle = \frac{1}{\sqrt{M}} \sum_q e^{-iqx_j} |q\rangle$ [62]. This leads to the time evolution

$$|\psi(t)\rangle = e^{-i\,\hat{H}_{\mathrm{TB}} t/\hbar}\,|j\rangle = \frac{1}{\sqrt{M}} \sum_q e^{-i\,\cos(qa) 2Jt/\hbar}\, e^{-iqx_j}\,|q\rangle. \tag{2.11}$$

Taking $M \to \infty$ and $a \to 0$, we can consider the continuum limit of the previous expression reaching

$$|\psi(t)\rangle = \frac{1}{2\pi} \int_{-\pi}^{+\pi} dq\, e^{-i\cos(q) 2Jt/\hbar}\, e^{-iqj}\,|q\rangle. \tag{2.12}$$

We now calculate the overlap of $|\psi(t)\rangle$ with a localized state in a single lattice site l,

$$\langle l|\psi(t)\rangle = \frac{1}{2\pi} \int_{-\pi}^{+\pi} dq\, e^{-i\,\cos(q) 2Jt/\hbar}\, e^{-iq(j-l)}, \tag{2.13}$$

which by using the integral representation of the Bessel function $\mathcal{J}_n(x)$,

$$\mathcal{J}_n(x) = \frac{1}{2\pi} \int_{-\pi}^{+\pi} dq\, e^{i(x\sin x - nx)}, \tag{2.14}$$

can be rewritten as

$$\langle l|\psi(t)\rangle = \mathcal{J}_{|j-l|}\left(\frac{2Jt}{\hbar}\right) \tag{2.15}$$

This means that in a lattice site d sites away from the initial one, the probability of finding a particle as a function of time is $p_d = |\mathcal{J}_d(2Jt/\hbar)|^2$.

Such spatial quantum walks have been explored in the BH model for different settings of ultracold atoms in optical lattices [63–65] and recently in superconducting circuits [66].

2.2 Ultracold atoms in optical lattices

The situation of an individual atom moving in an optical lattice has a direct resemblance to electrons moving in a perfect crystal. This has been precisely the motivation to study the BH model using ultracold atoms in optical lattices [56], given that in many regimes this is a very precise description of this system.

In this section we will show how Eq. 2.1 and its terms emerge from considering a quantum particle in the lowest band of a (sinusoidal) periodic potential and link the physical quantities in the atomic physics context to the BH parameters.

2.2.1 Single atom in a periodic potential

We consider the situation of a single neutral atom trapped in a three-dimensional dipole potential made by three perpendicular optical lattices with wavelengths λ_x, λ_y, λ_z and lattice spacing given by $a_{\mathrm{lat},i} = \pi/k_i = \lambda_i/2$ (in the case of retroreflected lattices). Assuming homogeneous, infinite laser beams, the AC-Stark shift experienced by the atoms [67] in such a lattice structure can be simply written as a sum of three potentials,

$$V(x,y,z) = V_x \cos^2(k_x x) + V_y \cos^2(k_y y) + V_z \cos^2(k_z z). \tag{2.16}$$

As it is common in the field of ultracold atoms, we will express the lattice depth V_i in units of the lattice recoil energy $E_{\mathrm{r},i} = h^2/8ma^2_{\mathrm{lat},i}$. The expression of Eq. 2.16 directly implies that the problem is separable, and allows us to focus on solving only the one-dimensional Schrödinger equation

$$-\frac{\hbar^2}{2m}\partial_x^2 + V_x \cos^2(k_x x)\,\psi_x(x) = E\,\psi_x(x). \tag{2.17}$$

This problem is indeed a fundamental one in the field of quantum theory and solid-state physics: a quantum particle in a sinusoidal potential.

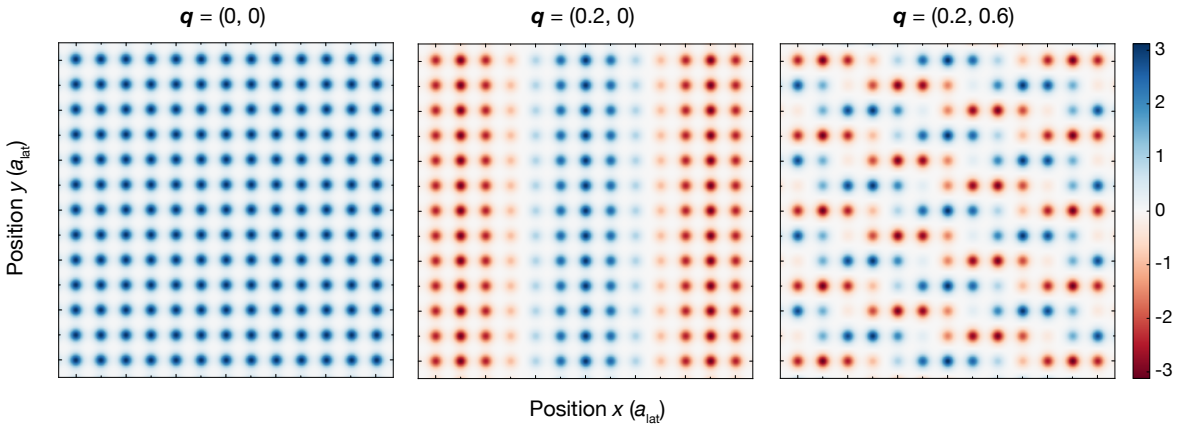

Figure 2.2: Lowest-band Bloch waves in a square lattice at $V = 12\,E_{\mathrm{r}}$. 2D plot of the real part of the two-dimensional Bloch wavefunction $\psi_{0,\boldsymbol{q}}(x,y)$ in a square lattice. Each 2D plot corresponds to a different value of $\boldsymbol{q}$, expressed in units of π/a_{lat}.

Bloch waves

We know from Bloch's theorem [54] that given the periodicity of the lattice potential, i.e. $V(x) = V(x + a_{\text{lat}})$, the eigenstates of the system can be written as Bloch waves

$$\psi_{n,q}(x) = e^{-iqx}\, u_{n,q}(x), \tag{2.18}$$

where $u_{n,q}$ is a function with the same periodicity as the lattice, n the band index, and q is the quasimomentum or lattice momentum, analogous to the one we introduced for the tight-binding solution, and therefore $|q| < \pi/a_{\text{lat}}$.

The solutions of Eq. 2.17 can be obtained numerically (a more detailed derivation can be found in [68, 69]), but one can also directly use the solutions of the Mathieu equation, the so-called Mathieu functions of the first kind [70, 71]. In Fig. 2.2 we plot the real part of the two-dimensional solutions, $\psi_{\boldsymbol{n},\boldsymbol{q}}(x,y) = \psi_{n_x,q_x}(x) \cdot \psi_{n_y,q_y}(y)$, in a square lattice for three different values of $\boldsymbol{q}$ at $n_x = n_y = 0$.

Wannier functions

While the Bloch waves are the direct solutions to Eq. 2.17, the Wannier functions are an extremely useful tool in the context of particles in crystals [72], and will be required to connect to the second quantization formalism later. The expression for a Wannier function in the n-th band and localized around site j is given by

$$w_n(x - x_j) = \frac{1}{\sqrt{\mathcal{N}}} \sum_q e^{-iqx_j}\, \psi_{n,q}(x) \tag{2.19}$$

where the summation runs over all quasimomenta q within the first Brillouin zone, and can be seen as the discrete Fourier transform of the Bloch functions. $\mathcal{N}$ is a normalization constant. These functions fulfill few important conditions:

- They are defined centered around the potential minima at x_j.
- Their set forms an orthonormal basis for the states in the corresponding band.
- They are exponentially localized around their site at x_j.

We can now consider again the three-dimensional case and express the Wannier function as the product of the one-dimensional ones:

$$w_{\boldsymbol{n}}(\boldsymbol{r} - \boldsymbol{R_j}) = w_{n_x}(x - x_j) \cdot w_{n_y}(y - y_j) \cdot w_{n_z}(z - z_j). \tag{2.20}$$

2.2.2 Linking to the Bose-Hubbard

We now consider the three-dimensional problem of a gas of N interacting atoms in an optical lattice. Atom-atom interactions in dilute Bose gases can typically be modelled as an effective contact interaction [3, 73], and the many-body Hamiltonian in second quantization can be expressed as

$$\hat{H}_{\mathrm{OL}} = \int d\boldsymbol{r}\, \hat{\Psi}^{\dagger}(\boldsymbol{r}) \left[-\frac{\hbar^2}{2m}\nabla^2 + V(\boldsymbol{r}) \right] \hat{\Psi}(\boldsymbol{r}) + \frac{4\pi\hbar^2 a_{\mathrm{s}}}{2m} \int d\boldsymbol{r}\, \hat{\Psi}^{\dagger}(\boldsymbol{r})\, \hat{\Psi}^{\dagger}(\boldsymbol{r})\, \hat{\Psi}(\boldsymbol{r})\, \hat{\Psi}(\boldsymbol{r}), \tag{2.21}$$

where a_s is the s-wave scattering length for the corresponding species and $\hat{\Psi}^{(\dagger)}(\boldsymbol{r})$ are the quantum field operators [74].

We now use the three-dimensional Wannier function $w_{\boldsymbol{n}}(\boldsymbol{r}-\boldsymbol{R}_j)$ to express the field operators in their basis as

$$\hat{\Psi}(\boldsymbol{r}) = \sum_{n,j} w_{\boldsymbol{n}}^{*}(\boldsymbol{r}-\boldsymbol{R}_j)\, \hat{a}_{n,j}\,. \tag{2.22}$$

The next step will be to proceed by taking the single-band approximation, which means we will consider the population in any Bloch bands other than the lowest one to be negligible. This allows us to drop the n index of the Wannier functions. We now take a look at the kinetic and the interaction terms separately.

Kinetic energy term

The final expression we reach for the first (kinetic) term of Eq. 2.21 is

$$\begin{aligned} \hat{H}_{\mathrm{kin}} &= \int d\boldsymbol{r} \left(\sum_i w(\boldsymbol{r}-\boldsymbol{R}_i)\, \hat{a}_i^{\dagger} \right) \left[-\frac{\hbar^2}{2m}\nabla^2 + V(\boldsymbol{r}) \right] \left(\sum_j w^{*}(\boldsymbol{r}-\boldsymbol{R}_j)\, \hat{a}_j \right) \\ &= \sum_{i,j} \hat{a}_i^{\dagger}\, \hat{a}_j \underbrace{\int d\boldsymbol{r}\, w(\boldsymbol{r}-\boldsymbol{R}_i) \left[-\frac{\hbar^2}{2m}\nabla^2 + V(\boldsymbol{r}) \right] w^{*}(\boldsymbol{r}-\boldsymbol{R}_j)}_{-J_{ij}}\,. \end{aligned} \tag{2.23}$$

Now, using the fact that Wannier functions fall off exponentially from $\boldsymbol{R}_i$, we can directly see that J_{ij} can be neglected for any two sites beyond nearest-neighbor. In the case of a cubic lattice, it will directly lead to the tight-binding expression we saw in

section 2.1,

$$\hat{H}_{\text{kin}} \approx -J \sum_{\langle i,j \rangle} \hat{a}_i^\dagger \hat{a}_j \,. \tag{2.24}$$

From this, we can also reconnect to Eq. 2.4 in terms of Bloch waves, and alternatively obtain the nearest-neighbour tunneling J directly from the width of the band

$$J \approx \frac{E_{\text{max}} - E_{\text{min}}}{2\,z}\,, \tag{2.25}$$

which for the one-dimensional case is just

$$J \approx \frac{E(q = \pi/a_{\text{lat}}) - E(q = 0)}{4}\,. \tag{2.26}$$

Interaction energy term

We now follow similar steps for the second term of Eq. 2.21, and replace the quantum field operators by their expansion in terms of Wannier functions. From this we obtain

$$\begin{aligned}
\hat{H}_{\text{int}} &= \frac{4\pi\hbar^2 a_{\text{s}}}{2m} \sum_{ijkl} \hat{a}_i^\dagger \hat{a}_j^\dagger \hat{a}_k \hat{a}_l \int d\boldsymbol{r}\, w(\boldsymbol{r} - \boldsymbol{R_i})\, w(\boldsymbol{r} - \boldsymbol{R_j})\, w^*(\boldsymbol{r} - \boldsymbol{R_k})\, w^*(\boldsymbol{r} - \boldsymbol{R_l}) \qquad (2.27)\\
&\approx \frac{4\pi\hbar^2 a_{\text{s}}}{2m} \sum_{i} \hat{a}_i^\dagger \hat{a}_i^\dagger \hat{a}_i \hat{a}_i \int d\boldsymbol{r}\, |w(\boldsymbol{r} - \boldsymbol{R_i})|^4 \\
&= \underbrace{\frac{4\pi\hbar^2 a_{\text{s}}}{m} \int d\boldsymbol{r}\, |w(\boldsymbol{r} - \boldsymbol{R_i})|^4}_{U}\; \frac{1}{2} \sum_i \hat{a}_i^\dagger \hat{a}_i \left(\hat{a}_i^\dagger \hat{a}_i - 1 \right).
\end{aligned}$$

In the second line we have used again the properties of the Wannier functions to keep only the integrals in which $\boldsymbol{i} = \boldsymbol{j} = \boldsymbol{k} = \boldsymbol{l}$, given the small overlap between functions of different sites. In the last line, we have taken the integral out of the sum, which is justified for an homogeneous system, and we have used the bosonic commutation relation $[\hat{a}_i, \hat{a}_j^\dagger] = \delta_{i,j}$ to rewrite the four-operator term.

With this, we have derived the connection between the physical parameters of the atomic system and the BH model, and we can write the kinetic and interacting terms together in the form

$$\hat{H}_{\text{OL}} \approx -J \sum_{\langle i,j \rangle} \hat{a}_i^\dagger \hat{a}_j + \frac{U}{2} \sum_i \hat{n}_i \,(\hat{n}_i - 1). \tag{2.28}$$

This expression directly reflects that a quantum simulation of the BH model can be realized with ultracold bosonic atoms in optical lattices, which is a cornerstone of the experiments in this thesis.

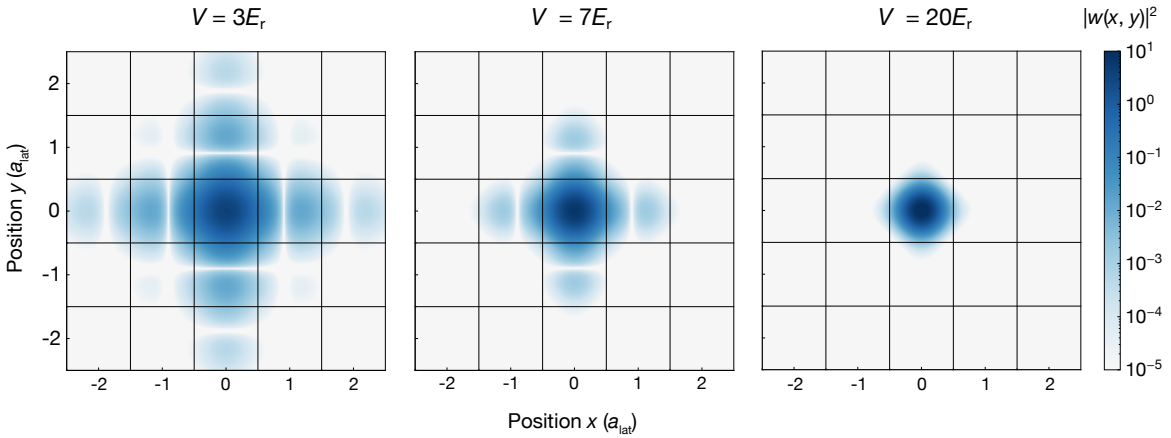

Figure 2.3: Wannier functions in a square lattice at different lattice depths. 2D plots of the probability density for a lowest-band Wannier function, $|w_0(x,y)|^2$, for different lattice depths. The colormap is in a logarithmic scale to better appreciate the parts of the Wannier function in the neighbouring sites. Below $5\,E_\mathrm{r}$, the overlap of the wavefunctions with those for next-nearest neighbours is not negligible in comparison to the nearest neighbours, and cannot thereby be mapped to a model with only nearest neighbour tunneling.

2.2.3 Additional effects

Here we discuss other effects and contributions that have been ignored in the previous section but which are particularly important for real experiments with ultracold atoms in optical lattices.

System inhomogeneity

While in this chapter we have only considered homogeneous systems, i.e. translationally invariant, the laser beams used to generate the trapping potentials are generally Gaussian, and hence the main source of their inhomogeneity is their Gaussian intensity profile. This can be generally taken into account by considering a harmonic potential along each axis l, that is

$$V_\mathrm{ext}(r_{\boldsymbol{i}}) = \sum_l \frac{1}{2} m(\omega_l\, r_{\boldsymbol{i},l})^2\,. \tag{2.29}$$

Where $r_{i,l}$ is the l-th component of the position r_i at site i. This contribution can be absorbed into an effective local chemical potential given by

$$\mu_i = \mu - V_i = \mu - V_{\text{ext}}(r_i)\,. \tag{2.30}$$

This allows one to consider the system locally as an homogeneous system with chemical potential μ_i. In a harmonic trap, this implies that in the center of the trap the system has a chemical potential μ, and as one moves away from the center μ_i will decrease, hence one probes different chemical potentials at the same time in a single system, and a coexistence of superfluid and Mott-insulating phases can take place [75].

Shallow lattices

In Eq. 2.24 we neglected any tunneling terms J_{ij} beyond nearest neighbours. This is a very good approximation close to the atomic limit, but for very shallow lattice depths, next-nearest-neighbour terms can become significant. In the experiments in this thesis, this assumption remains valid, since even for a small depth of $3\,E_\text{r}$, this suppression between nearest-neighbour and next-nearest-neighbour tunneling is of roughly an order of magnitude [76]. Hence a breakdown of the tight-binding approximation, and thereby of the BH model, will only take place at shallower lattices or for very long times. In Fig. 2.3 we can see the probability density of the Wannier functions in two dimensions for different lattice depths. One can see that at $3\,E_\text{r}$ the overlap with beyond nearest-neighbours sites is significantly higher than at 7 and $20\,E_\text{r}$.

Chapter 3

Experimental setup

In this chapter the setup and the main techniques used in the experiments of this thesis are described. We first discuss the main parts of the sequence used to generate a two-dimensional cloud of ultracold atoms in a square optical lattice. Next, we describe the properties of our high-resolution imaging setup and the scheme used for microscopically detecting the atoms. We continue by presenting the tools used for site-resolved addressing, involving a resonant microwave transfer and the use of a spatial light modulator. Finally, we mention few of the most crucial calibrations routinely performed for our experiments.

3.1 The sequence

The preparation of a two-dimensional degenerate quantum gas of ^{87}Rb in a square optical lattice, as desired for the simulation of the Bose-Hubbard model, involves three different vacuum chambers and a series of stages involving cooling, transport and state transfers for a total duration above 20 seconds. In this section we summarize the main parts of this sequence, including few recent changes and upgrades respect to the description in previous PhD theses [59, 77–80].

3.1.1 Laser cooling and transport stage

The sequence starts with a 2D$^+$ magneto-optical trap (MOT) stage in a chamber at 4×10^{-7} mbar, with a high rubidium pressure to ensure an efficient loading. This generates an atomic beam that travels through a differential pumping stage to reach a second chamber (at 1×10^{-11} mbar) where it feeds the 3D MOT, in which atoms are cooled and loaded during 2-3 seconds [81].

After the MOT stage, the atoms in the low-field-seeking $|F = 1, m_F = -1\rangle$ state are loaded into a quadrupole magnetic trap with a field gradient of $\sim 180\,\mathrm{G/cm}$, in which an evaporation stage takes place employing a microwave (MW) knife, which transfers the hottest atoms to the untrapped $|F = 2, m_F = -2\rangle$ state. This is the longest process of the sequence and takes $\sim 6.5\,\mathrm{s}$.

Once the MW evaporation stage is over, the atoms have reached a temperature

around 20 µK and are loaded into the transport dipole trap, with $\lambda = 1070\,\text{nm}$, placed below the magnetic trap. In addition to the original single focused beam configuration, we currently can use a crossed transport trap (CTT) with a small angle (3.5°), generated by splitting and separating the original beam before the first focusing lens of the setup [59]. The laser used is an Ytterbium fiber laser from IPG laser (YLR-50-1070-LP) with a linewidth of $\sim 5\,\text{nm}$, which ensures no strong interference effects in the CTT.

Once the magnetic gradient has been completely ramped down, the position of the transport beam focus is displaced by 13 cm to the science chamber, taking in total $\sim 2.5\,\text{s}$. A piezo mirror tuned during the transport allows to overlap the position of the CTT with the lattice beams in the science chamber.

3.1.2 Preparation of a 2D quantum gas

Once the focus of the transport trap reaches the center of the science chamber, the cloud is transferred into a crossed dipole trap (CDT) made out of two perpendicular in-plane $\lambda = 1064\,\text{nm}$ beams with waists of 70 µm. These are the same beams used to later generate the horizontal optical lattices, though with their retroreflective mirrors blocked by a flipper mount. Next, we force evaporation by decreasing exponentially the depth of the CDT to a value low enough to bring the gas close to degeneracy. Next, the cold three-dimensional cloud is loaded into an optical lattice along the z axis, generated by the reflection of a vertical $\lambda = 1064\,\text{nm}$ beam from a coated viewport (see Fig. 3.1). All the mentioned optical lattices are generated from two Mephisto MOPA lasers with ultra-narrow linewidth (from Innolight/Coherent), which feature a long coherence length and very low noise. After the ramping of this vertical z-lattice, the atoms populate several of its antinodes.

The z-lattice provides the strong vertical confinement required to generate a two-dimensional system. While ideally one would populate only a single lattice antinode, the approach in our setup is instead to optically remove all the initially occupied layers except for one. To do so, a strong magnetic vertical gradient field ($45\,\text{G/cm}$ or $\sim 5\,\text{kHz/µm}$) is used such that one can resolve the individual planes of the lattice by a narrow MW sweep ($\sim 2\,\text{kHz}$) on their hyperfine transitions.

After this "slicing" process (described in more detail in [77]), a single plane is populated with atoms in the $F = 1$ hyperfine states. Next, the last evaporation stage of the sequence takes place, for which a strong horizontal magnetic gradient is introduced by placing the zero of the magnetic field in the plane and shifted from the cloud (using three pairs of "offset" coils along the x,y,z axes). This gradient allows to spill out the atoms horizontally during evaporation in a combined dipole trap of the z-lattice and the tight "dimple" dipole trap. This dimple is based on a laser beam at 850 nm

focused through the objective (10 µm waist [59]). The dimple evaporation takes 1 s, and the temperatures reached after this last stage reach the few nK regime.

3.1.3 Producing a Mott insulator in a square lattice

Having achieved a single 2D degenerate gas, we finally introduce the in-plane optical lattices, allowing us to describe the system with an atomic Bose-Hubbard model as discussed in Ch. 2. Typically, we obtain a superfluid state by slowly ramping the depth of both in-plane lattices below 10 E_r, where E_r is the recoil energy given by a photon of $\lambda = 1064\,\text{nm}$ to a ^{87}Rb atom. By ramping to even deeper lattices, we can prepare the cloud in a Mott-insulator state. To stay close to adiabaticity while crossing the critical point, we usually employ two consecutive s-shaped ramps (using a sigmoid function) [79], the first one until 10 E_r and the following one beyond, often up to 40 E_r (the deep atomic limit). Given that no further cooling takes place beyond this stage, it is very important to avoid heating during the initial turn-on of the lattices, for which we carefully monitor any spikes in the intensity stabilization.

The state most commonly prepared for all our experiments is a Mott insulator at unit filling. To produce it, we tune the dimple evaporation to set the right number of atoms, such that no $n = 2$ shell appears in the center of the cloud. The maximum size of the unit-filling Mott insulator will therefore be restricted by the trapping potentials generated by the three lattices. Notice that by reducing the depth of the vertical lattice during the ramp-up of the horizontal lattices one can achieve slightly bigger sizes than otherwise (roughly 30% more, a total of 250 atoms). Other alternatives involve the use of deconfining optical beams [82] or our magnetic gradient.

3.2 Site-resolved microscopy

The main feature enabling most of the experiments performed in our ultracold-atom setup is quantum-gas microscopy, i.e. the possibility of measuring the atomic occupations in the individual optical lattice sites by using a fluorescence scheme with a high-resolution imaging setup. In the current section we describe the main properties of the imaging setup and the imaging techniques.

3.2.1 The imaging setup

Identifying the occupation in each individual lattice site means distinguishing the positions of the atoms at distances below the lattice spacing a_{lat}. This requires an imaging system with a high optical resolution, which in our setup is based on a objective with a high numerical aperture (NA) placed outside of the science chamber. The main specifications of the objective and the imaging setup are indicated in Tab. 3.1. Since

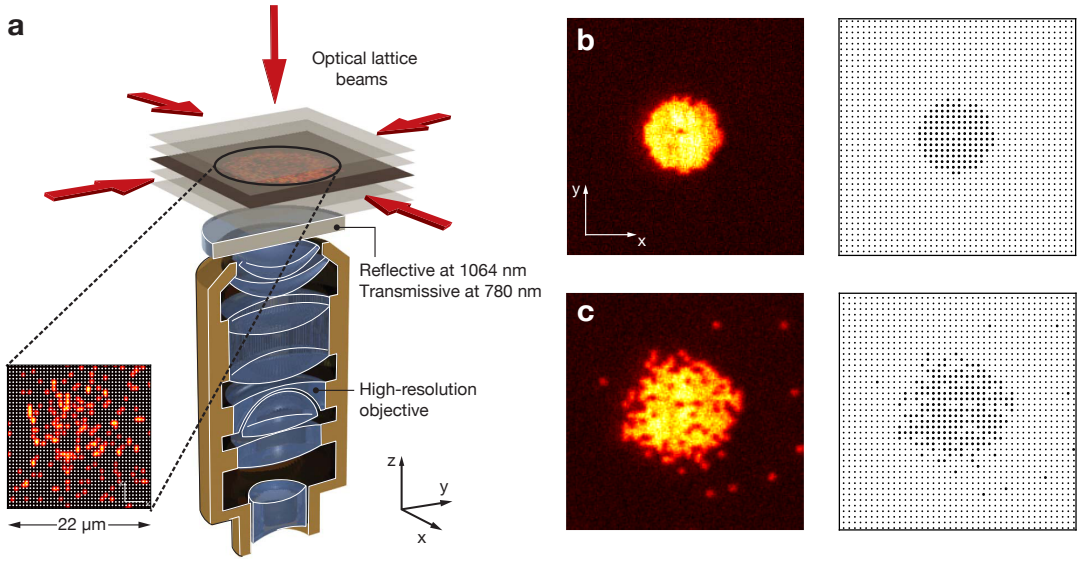

Figure 3.1: Quantum-gas microscopy of a two-dimensional Bose-Hubbard system. **a** Schematic of the optical-lattice structure, high-NA objective and imaging. **b** Example fluorescence snapshot of a unit-filling Mott insulator with only a single defect in the bulk, together with its reconstructed occupation. **c** Example snapshot of a Mott insulator with few excitations on top, together with its reconstructed occupation.

we employ the D_2 line of ^{87}Rb (at $\lambda = 780\,\mathrm{nm}$) to image the atoms, this leads to an expected optical resolution of $R \approx 700\,\mathrm{nm}$, based on the Rayleigh criterion.[1] Notice that while this is higher than the lattice spacing $a_{\mathrm{lat}} = 532\,\mathrm{nm}$, the knowledge that the atoms sit only on the antinodes of the optical lattice enables nonetheless to reconstruct the occupations by using a reconstruction algorithm [78].

Table 3.1: Main parameters of the objective and the imaging setup.

The imaging setup	
NA @ 780 nm	0.68
Magnification	130
Solid angle	$0.13 \cdot 4\pi$
Depth of focus	1.7 µm

[1] The Rayleigh criterion considers two point sources to be resolved when the maximum of the Airy diffraction disk of one falls in the first minimum of the pattern of the other (see [83], for example). This can be expressed as $R = 0.61\,\lambda/\mathrm{NA}$ for a microscope.

3.2.2 Optical-molasses imaging

By combining a high-resolution imaging setup with high-power lasers that strongly pin the position of the atoms into individual lattice sites, it is possible to image their positions by scattering a high amount of photons from each atom. For this, all lattices are taken to a extreme depth of $\sim 3000\, E_\mathrm{r}$. Nonetheless, this photon scattering process will efficiently heat the atoms into higher bands, and eventually lead to the atoms tunneling to neighboring sites or escaping the central region of the trap. Because of this, we use optical-molasses cooling during the imaging stage, which ensures that the atoms remain in low bands and at the same time efficiently scatter many photons.

The optical molasses scheme is performed on the D_2 line, and arranged with two in-plane retroreflected beams (with opposite circular polarizations) and a single vertical beam, each one of those along the lattice axes. To avoid an unwanted intensity modulation due to interference between the beams, two piezo controllers in the retroreflecting mirror are modulated, and the vertical beam position rotates circularly.

A basic drawback of this imaging technique is the fast loss of atomic pairs due to light-assisted collisions. This deprives one from faithfully imaging multiply-occupied sites, such that we resort to a controlled excitation of atomic pairs before imaging, leading to the well-known "parity projection" [9, 10]. More details of the whole process of molasses imaging can be found in [77].

During the imaging duration, of approximately 1 s, each atom can typically scatter tens of thousands of photons, of which we detect roughly 7% of the total, which is $\sim$ 7000 photons per atom. The spatial distribution of the photons after being collected by the objective is measured by an electron-multiplying charge-coupled device (EMCCD), in particular the model iXon$^{\mathrm{EM}}$ + 897 from Andor technology (now part of Oxford instruments), which allows for a good detection in the few-photon regime. From a Gaussian-profile fit of the point spread function of a single atom, based on several snapshots of isolated atoms, one obtains a $\sigma \approx 267\,\mathrm{nm} = 0.5\, a_\mathrm{lat}$ [78]. This corresponds to an imaging resolution[2] of $R \approx 724\,\mathrm{nm}$, consistent with the expectation from the NA of our objective.

Even with molasses cooling, heating to higher bands during the imaging will occur, which can lead to hopping events of the atoms from their lattice sites. This will either change their original position or directly lead to losses due to light-induced collisions with nearby atoms. We usually optimize the lattice and molasses alignment such that we observe less than 1% of hopping events in the cloud. This commonly involves a fine alignment of the retroreflections of the optical-lattice beams and also of the molasses beams, which can be aided by optimizing the far-field coherent scat-

[2] Here we approximated the first lobe of the Airy diffraction pattern with a Gaussian profile, and enforcing them to have the same volume leads to $\sigma = 0.225\,\lambda/\mathrm{NA}$ [84].

tering peaks [85].

Additionally, to ensure that the objective remain in focus with the atoms, we routinely run an "idle sequence" [78], which takes 7 snapshots of a same Mott-insulator cloud at different vertical positions of the objective (shifted by a piezo controller) and feeds back the correct value to the rest of sequences.

3.2.3 Accessible observables

In situ imaging is the main application for quantum-gas microscopy, providing us with the site-resolved occupation of the system. Nonetheless, additional information about the properties of the system can be obtained through different imaging methods. In this subsection we discuss the three main approaches that are relevant for the experiments performed in this thesis.

In situ imaging

In most cases, the described imaging technique is used to directly measure the spatial occupations of a prepared state in the lattice plane. To do this, we first ramp up the depth of all three lattices to the atomic limit ($V = 40\,E_\mathrm{r}$) in less than a millisecond. Next, we ramp all the lattices to the imaging depth, $\sim 3000\,E_\mathrm{r}$ for each axis. During the first ramp, the intensity of the lattices is actively stabilized, while the final ramp is just set to the maximum power available in a free-running mode.

Let us now discuss in more detail which observables we access via quantum-gas microscopy. Ideally one wishes to measure $\hat{n}_{\boldsymbol{i}}$, i.e. the atom number in a single site $\boldsymbol{i}$, by reconstructing it from a fluorescence picture. Due to parity projection, one measures $\hat{n}_{\mathrm{det},\boldsymbol{i}}$ instead, which we will refer to as the "detected occupation". Considering the observable in only a single lattice site, $\hat{n}_\mathrm{det}$, we can define it as

$$\hat{n}_\mathrm{det}\,|m\rangle = (m \bmod 2)|m\rangle\,, \tag{3.1}$$

where $|m\rangle$ is a Fock state with m particles. If we now consider the reduced density matrix $\hat{\rho}$ of a single site, the expectation value of the detected occupation is given by

$$\langle \hat{n}_\mathrm{det}\rangle = \mathrm{Tr}(\hat{\rho}\,\hat{n}_\mathrm{det}) = \sum_m \rho_{mm}\cdot(m \bmod 2)\,, \tag{3.2}$$

and therefore $0 \leq \langle \hat{n}_\mathrm{det}\rangle \leq 1$. Now let us take a look at the variance of the detected occupation, which is given by

$$\sigma^2_\mathrm{det} = \langle \hat{n}^2_\mathrm{det}\rangle - \langle \hat{n}_\mathrm{det}\rangle^2\,. \tag{3.3}$$

Using that the eigenvalues of $\hat{n}_\mathrm{det}$ can only be 0 or 1, we can see that $\langle \hat{n}^2_\mathrm{det}\rangle = \langle \hat{n}_\mathrm{det}\rangle$,

and therefore one can express the previous equation simply as

$$\sigma^2_{\mathrm{det}} = \langle \hat{n}_{\mathrm{det}} \rangle (1 - \langle \hat{n}_{\mathrm{det}} \rangle) \,, \tag{3.4}$$

which makes it easy to see that $0 \leq \sigma^2_{\mathrm{det}} \leq 0.25$.

With this knowledge, we can now analyze what will these observables tell us about the phases of the Bose-Hubbard model. For an atomic-limit Mott insulator with m particles per site, the detected mean atom number is given by $\langle \hat{n}_{\mathrm{det}} \rangle = m \bmod 2$, and the detected variance will vanish, $\sigma^2_{\mathrm{det}} = 0$. In the case of a superfluid, we already discussed in Ch. 2 that for large system sizes we ideally expect a Poissonian distribution of the single-site occupation number. The detected occupation is then given by $\langle \hat{n}_{\mathrm{det}} \rangle = 0.5\,(1 - \exp(-2\alpha^2))$ and the detected variance σ^2_{det} will have a finite value. For single-site densities of few particles this values will already saturate to $\langle \hat{n}_{\mathrm{det}} \rangle = 0.5$ and $\sigma^2_{\mathrm{det}} = 0.25$, which is the maximum detectable variance.

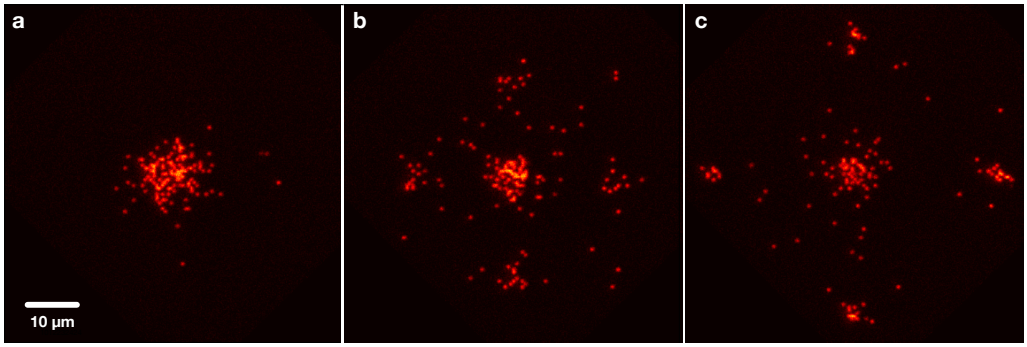

Figure 3.2: Individual snapshots after an in-plane TOF. Single fluorescence images taken of a superfluid state after a TOF of **a** $t = 0$, **b** $t = T/8$, **c** $t = T/4$.

Momentum-space imaging

A common tool in the field of ultracold atoms is the imaging in momentum space after a time of flight (TOF). In the TOF measurement, the atoms are suddenly released from the trapping potentials into free space, and after a long-enough evolution, the momenta of the particles are mapped into their spatial distribution, which is typically measured via absorption imaging of the cloud [7, 58]. This measurement method is used very often in systems with finite- or long-range phase coherence, since from the measured interference pattern, properties of the coherence can be quantified.

In our quantum-gas microscope, imaging in momentum space faces two challenges: First, the small atom number with which we routinely work (few hundreds of atoms) makes it hard to resolve the momentum distribution via an absorption mea-

surement in free space. Second, the size of the region imaged by the microscope is quite limited, which restricts the maximum possible TOF time. These two issues can be addressed by implementing an in-plane TOF followed by a recapture in the in-plane lattices that allows to image in fluorescence. On the one hand, the fluorescence imaging ensures single-particle detection (aside from parity projection), while on the other, the TOF in an harmonic trap allows to image the momentum distribution with a reasonably short time. This can be explained by the fact that after a quarter of a period ($T/4$) of an oscillation in the harmonic trap, the initial momentum distribution will be mapped into the spatial one [86]. While during the TOF interactions are still present, they are weak given the absence of the in-plane lattices. A similar technique was already used in a quantum-gas microscope to identify the transition from superfluid to Mott insulator [10].

In Fig. 3.2 we show examples of the fluorescence pictures taken after different TOFs for a cloud in the superfluid state. For $t = T/4$, one can appreciate the typical interference pattern expected for long-range coherence in a square lattice. While the exact mapping to momentum space is valid at $T/4$, notice that it can be convenient to extract the information on the coherence from shorter times of expansion, such as at $T/8$, to avoid higher occupations leading to parity projection.

To quantify the coherence of an atomic phase in a lattice we can measure the interference visibility V. Its definition is given by

$$V = \frac{N_{\text{max}} - N_{\text{min}}}{N_{\text{max}} + N_{\text{min}}}, \tag{3.5}$$

where $N_{\text{max(min)}}$ denotes the number of detected atoms in the maxima(minima) of the interference pattern (see Fig. 3.3). This quantity should give a value of $V \approx 1$ for a system with long-range coherence, and $V \approx 0$ for a totally incoherent system. A finite value of V is consistent with short-range coherence or a finite superfluid fraction. A description of the properties of the interference visibility can be found in [58].

Measurement of the total atom number

Due to the light-induced collisions that take place during the optical-molasses imaging, the measurement of the total atom number in the 2D system is hindered. This is an important measurement, for example, to quantify the particle losses in the system. An alternative for such cases is to allow for a short in-plane TOF, as described in the previous subsection, to strongly reduce the density, and then recapture the atoms in the in-plane lattices for imaging. To avoid any constructive interference effects, which might enhance light-induced collisions, one can start from very deep in-plane lattices. This allows one to measure the total atom number N. Aside from a study on losses,

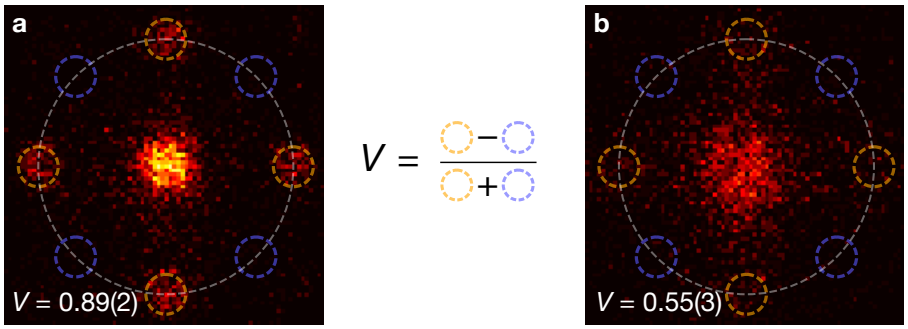

Figure 3.3: Measurement of the interference visibility. Visibility for two examples of mean-atom-number distribution after a $t = T/8$ TOF. The orange circles indicate the position of the four maxima regions (first peaks of the interference pattern) and the blue circles the minima regions (at the same distance from the center but along the diagonal).

this method can be used to estimate the fraction of highly-occupied sites in a prepared state, by comparing the total atom number with the parity-projected one [87]. Notice that while such a measurement will not provide any information on the initial spatial position of the atoms, one can also consider a one-dimensional TOF by switching off only one of the in-plane lattices, leading to a propagation in individual tubes, similar as done in other microscope experiments [39]. A similar approach has also been used in our setup to faithfully distinguish the spin degree of freedom from holes giving the same signal [88, 89].

3.2.4 Mott-insulator thermometry

The site-resolved measurement of the atomic occupations enables a sensitive thermometry technique, based on a fit of the density profile of the cloud in the atomic limit [9]. Let us consider the Bose-Hubbard Hamiltonian for a vanishing tunneling

$$\hat{H}_{\mathrm{BH}}\,(J=0) = \sum_i \left(\frac{U}{2}\hat{n}_i\,(\hat{n}_i - 1) - \mu_i\,\hat{n}_i \right) = \sum_i \hat{h}_i\,, \tag{3.6}$$

where we have assumed the local density approximation for μ_i, as described in Sec. 2.2.3. We see that the dynamics in each lattice site i is given by a single local Hamiltonian $\hat{h}_i$. Hence, the system is now formed of an array of decoupled wells, determined by its interactions and its local chemical potential [90].

We can now obtain the probability for each single-site microstate, which is deter-

mined by the occupation n in that site, from the grand-canonical ensemble as

$$p(n) = \frac{e^{-\beta(E(n)-\mu)}}{\mathcal{Z}(\mu, T)}, \tag{3.7}$$

where $\beta = 1/k_B T$, $E(n) = U n(n-1)/2$ and $\mathcal{Z} = \sum_n e^{-\beta(E(n)-\mu)}$ is the grand-canonical partition function. From this expression, one can extract the mean detected atom number, considering parity projection, at a finite temperature T

$$\langle \hat{n}_{\text{det}} \rangle (\mu, T) = \frac{1}{\mathcal{Z}(\mu, T)} \sum_m e^{-\beta(E(m)-\mu)} \cdot (m \bmod 2) . \tag{3.8}$$

If we now consider our 2D system and assume an isotropic trapping, that is $\omega_x = \omega_y$, this implies that $\mu_i = \mu(r)$, where r is the distance from the center of the trap. One can then fit the experimentally measured $\langle \hat{n}_{\text{det}} \rangle (r)$ to the expression in Eq. 3.8, from which we can extract the temperature T and the chemical potential in the center of the trap $\mu = \mu(r = 0)$. One can even use this thermometry method for a single snapshot, since an azimuthal average at constant r is equivalent to an ensemble averaging [9, 59, 77].

A typical temperature measured in our system is of $T \sim 0.1\, U/k_B$ [9], and the melting temperature of the Mott insulator is roughly at $T = 0.2\, U/k_B$ [90].

3.3 Single-site addressability

Aside from the possibility of resolving the occupation of individual atoms in each lattice site, the high NA of the objective in our setup opens the door to the site-resolved manipulation of the state of the atoms, as well as the projection of potentials featuring short-scale correlations. In this section we describe the approach used in our setup, which combines two main features: the use of a spatial light modulator to engineer arbitrary patterns, and a technique based on selective MW transfer to change the internal state of addressed atoms.

3.3.1 The addressing laser

For the addressing setup we employ laser light at $\lambda \approx 787$ nm provided from a commercial external-cavity diode laser with a tapered amplifier stage (TA pro, from TOPTICA Photonics). The chosen wavelength lies between the D_1 and D_2 lines of ^{87}Rb, which allows us to induce a high differential light shift between the $|1\rangle = |F = 1, m_F = -1\rangle$ and the $|2\rangle = |F = 2, m_F = -2\rangle$ hyperfine states. This will be a requirement for the MW addressing technique that we describe below. Concerning the

generation of potentials, an advantage of this wavelength is that we are not restricted to either attractive or repulsive potentials, given that control on the polarization and the wavelength allows to tune between them. Additionally, for the σ^- polarization the laser can be fine tuned to the "tune-out" (also called "magic-zero") wavelength, which for the $|1\rangle$ state is precisely at 787.55 nm, and can be used to introduce potentials which are insensitive to one specific spin [63, 91], as seen in Fig. 3.4.

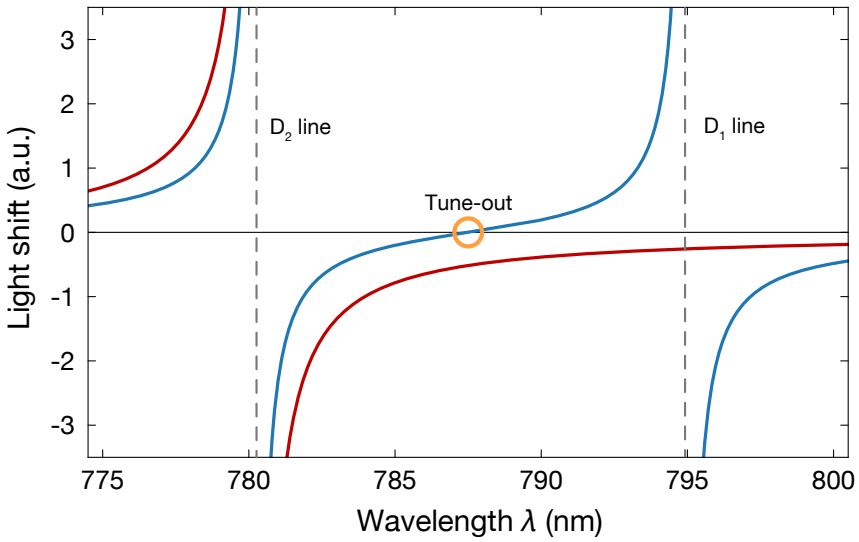

Figure 3.4: Spectrum of the light shift around the tune-out wavelength. Plot of the AC-Stark shift (in arbitrary units) from σ^--polarized light as a function of the optical wavelength for hyperfine states $|1\rangle$ (blue line) and $|2\rangle$ (red line). The tune-out wavelength for $|1\rangle$, at 787.55 nm, is indicated by a yellow circle.

While the use of such a near-detuned laser can be inconvenient, due to enhanced off-resonant scattering, in most of our experiments the atoms will be trapped by the far-detuned optical lattices and only moderate light shifts will be required from the addressing beam.

3.3.2 Digital-micromirror-device projection

To project arbitrary patterns in the atomic plane we use an imaging setup consisting of a digital micromirror device (DMD) at the image plane of the atoms. The DMD model is the DLP Discovery 4100 from Texas Instruments, provided by Vialux. Notice that this approach for addressing differs from the one using Fourier plane filtering [92] or the focusing of a single Gaussian beam with a tunable position, which was originally used in our setup [77].

The imaging system consists mainly of a Gaussian beam (FWHM $\approx$ 5.5 mm) which illuminates the mirror array of the DMD and a path of telescopes through which the image is propagated until the objective setup. An optical layout of the setup can be found in [79]. The total magnification and other technical parameters are specified in Tab. 3.2. Since the laser is closely detuned from the D_2 line, the dichroic shift is minimal, and the same feedback for the objective position obtained from the imaging idle can be used to ensure that the addressed image is properly focused.

The magnification in our setup is chosen so that each individual lattice site is oversampled by an array of $\approx 8 \times 8$ pixels, which allows us to project grayscale intensity distributions using an error diffusion algorithm [93]. Another alternative to generate grayscale potentials would be to used time-averaged potentials, but the flickering frequency in the DMD, set by the motion of their mechanical mirrors, would be detrimental for the temperature of the atoms, which would be resonantly heated. Generally, we only program the DMD in a 400×400 array of the whole size, limited by the intensity profile of the laser beam. This nonetheless allows us to image an area of 50×50 lattice sites, usually well above the size of our unit-filling Mott insulators.

Table 3.2: Main parameters of the DMD and the addressing setup.

The DMD addressing	
DMD resolution	1024×768
DMD pixel pitch	13.68 µm
Refresh rate	32.55 kHz
Total demagnification	195
Pixels per lattice site	7.7×7.7

3.3.3 MW addressing

The possibility of programming the DMD to illuminate only specific lattice sites, together with the differential light shift induced between different hyperfine states, makes it possible to selectively drive MW transitions in the atomic plane. In the most common approach of this technique, we start with a unit-filled Mott insulator in the $|1\rangle$ state and apply a MW Landau-Zener sweep of 20 ms around 6.8 GHz which resonantly transfers only the optically addressed atoms to the $|2\rangle$ state. The prepared spin pattern can be mapped to a density pattern by additionally applying a D_2 push-out pulse to the $|2\rangle$ state. It is remarkable that, by using the MW sweep, the effective resolution of the addressing process is given by a $\sigma \approx 140$ nm, well below the diffraction limit of the addressing-laser wavelength, and the spin-flip fidelity is around 95% [63]. Nonetheless, the simultaneous transfer done with the DMD might make this fidelity

slightly smaller for certain patterns.

3.3.4 Site-resolved potentials

By using the tools described above, we can study quantum systems with arbitrary potentials superimposed with the bare optical lattices. There is, however, a caveat, namely the finite resolution of the imaging setup. We can estimate a Gaussian point spread function of $\sigma_{787} \approx 269\,\mathrm{nm} = 0.506\,a_{\mathrm{lat}}$, which leads to a finite correlation between the potentials in nearby sites. This does not represent a big issue for the creation of, for example, random potentials, but makes it hard to generate potentials with strong anticorrelations between nearest neighbours, such as quasiperiodic models. To obtain an approximation of the potential projected in the atomic plane, necessary for any theoretical model, we introduce a Gaussian blur to the programmed potential, i.e. we convolve it with a Gaussian function. This is shown in Fig. 3.5a, where a convolution with a 2D Gaussian with $\sigma = 0.506\,a_{\mathrm{lat}}$ was used. For our programmed disorder potentials this leads to a correlation length $\xi \approx 0.6\,a_{\mathrm{lat}}$, and changes the overall distribution from a uniform to a rather Gaussian one (see supplementary material in [47]).

To ensure that the programmed potentials are faithfully projected into the 2D atomic system, it is desirable to measure the on-site potential directly in the atomic plane. By making use of the same ideas that enable single-site addressing, we can characterize the potential projected on the atomic plane. We use MW spectroscopy to measure the local light shift experienced by the atoms. We start by preparing a unit-filling Mott insulator in the $|2\rangle$ hyperfine state deep in the atomic limit. We then set the DMD pattern and ramp up the addressing laser to its maximum (stabilized) power. Then we perform a narrow-frequency sweep, transferring few of the atoms into $|1\rangle$, and we then optically push out the atoms in $|2\rangle$ and image the remaining atoms in $|1\rangle$. By repeating this process (with the same disordered pattern) over a range of frequencies, we are able to obtain a site-resolved MW spectrum, and map the local MW resonances (see Fig. 3.5b). The shift of the resonance frequency in each site determines the local differential light shift.

Given that the region addressed by the DMD (around 50×50 lattice sites) is much larger than the typically prepared system sizes of our clouds (below 20×20 sites, and ~ 300 atoms), it is convenient to prepare a Mott insulator as large as possible for the disorder calibration. With our current optical-lattice confinement, this can be around 500 atoms. Even if the increased size might be at the expense of an increased temperature of the Mott insulator, leading to holes and doublons, these will not significantly affect the resonance, since we only image the atoms that are efficiently transferred.

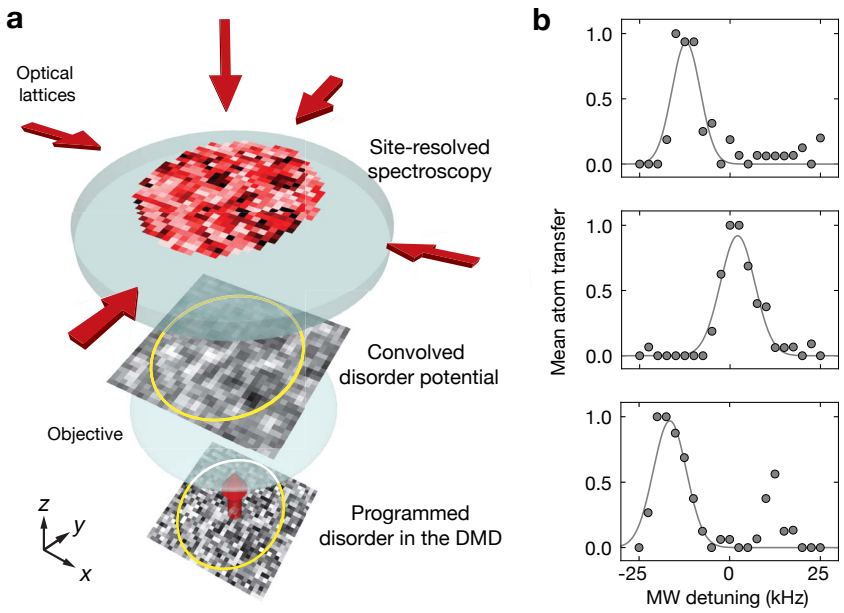

Figure 3.5: Projected potential and site-resolved spectroscopy. a Schematic of the programmable projection setup. A grayscale pattern programmed in the DMD, in this case disordered, is projected into the atomic plane through the objective, that due to its finite resolution leads to a slightly blurred disorder. The projected pattern can be obtained via MW spectroscopy of a Mott insulator. **b** Examples of three different single-site spectra and their Gaussian fits (gray curves).

3.4 System calibration

Four most of our experiments we have to keep a series of parameters properly calibrated and characterized. Here we briefly describe the most relevant calibrations for the experiments in this thesis.

Lattice depth calibration

The tunability to an exact depth of the optical lattices [94] is extremely important for all the experiments performed in our setup. Even for experiments that mostly require the preparation of a Mott insulator as an initial state (such as those exploring frozen Rydberg gases) it is important to know the exact position of the critical point to adiabatically ramp through it.

In our experiment we routinely perform a band spectroscopy, via lattice modulation [95], to calibrate the exact intensity for a lattice depth of 10 E_r. From this value, we linearly extrapolate to all other stabilized lattice depths, based on the measured beam

power. To locate the exact depth for the in-plane lattices, we begin with a condensate loaded into a single plane of the vertical lattice. We then ramp either the x or y lattice to a specific amplitude V and then modulate its depth at the frequency of the resonance between the lowest band and the second excited band at $q = 0$ (obtained from non-interacting numerics or the solutions of the Mathieu equation, as discussed in Sec. 2.2.1). We keep this frequency constant and then search the resonance by sweeping the depth V through each experimental repetition. The resonance is identified as an spatial expansion of the atoms along the modulated lattice. In the case of calibrating the vertical lattice, the procedure is a bit harder, since at low depths a potential gradient is always present (gravitational or magnetic) which will require to identify field-dependent sidebands, due to the Wannier-Stark ladder [62].

An alternative method for the calibration of the lattice in our setup is performing Raman sideband spectroscopy. This method, however, requires to perform the calibration at very deep lattices, which might increase the uncertainty of the depths at low powers.

Removal of magnetic gradients

The presence of residual magnetic gradients in the atomic plane can be a problem for many of our performed experiments. In this thesis this is particularly detrimental in experiments involving resonant tunneling, such as the dynamics in Part II. Our in situ imaging allows for a good characterization of such gradients by performing Ramsey interferometry between the two hyperfine states $|1\rangle$ and $|2\rangle$. This procedure is described in detail in the thesis [79].

Alignment of the addressing pattern

Generating site-resolved potentials and addressing single atoms with high fidelity requires an exquisite alignment between the projected pattern from the DMD and the antinodes of the in-plane optical lattices. In our experiment, the position of the addressing beam is very stable (it is projected through the objective) but thermal fluctuations shift the phase of the lattice sites in the plane [78].

To keep the phase of the lattices and the pattern locked to each other, we make use of a feedback scheme. It is based on using our addressing technique to prepare a well-defined atomic distribution, together with a position calibration based on automatic detection of the position of individual atoms.

Homogeneity of the DMD potential

An exact optical benchmark of the spatially modulated potentials projected in the atomic plane is not possible, and one mainly relies on using beam profilers before sending the beam through the objective. However, the presence of dirt and imperfec-

tions in the imaging system can lead to significant undesired speckle contributions. Because of this it is desirable to directly characterize the projected potential through the atoms. This is done by using the technique described in Sec. 3.3.4 to map out the site-resolved potential in the atomic plane. This then allows one to feedback to the programmed pattern in the DMD to correct global unwanted gradients [79].

A future solution that could strongly reduce any speckle inhomogeneity in our setup is the use of an incoherent laser source, as demonstrated in [96].

Heating and losses

Since the remaining openness in the system is a fundamental limitation in all experiments exploring quantum out-of-equilibrium dynamics, it is important to quantify all uncontrolled processes leading to heating or atom losses. In our experiment, particle losses can either be caused by background-gas collisions [97], parametric excitation or photon scattering. Background-gas collisions are limited by the quality of the vacuum in the science chamber, and in our setup are taken as intrinsic. Parametric excitation processes will most likely stem from fluctuations in the dipole traps, which can either be caused by intensity, frequency or mechanical noise. Finally, photon scattering is likely to come either from leakage of resonant light (limited by shutters or acousto-optic modulators) or from off-resonant scattering of high-intensity dipole traps. Aside from processes that take the atoms out of the system, we are also extremely sensitive to heating processes within the lowest band. These are believed to come purely from parametric excitations.

In the conditions in which the experiments described in Part II were realized, we observed atomic losses of 20% of the system after $\sim 6\,\mathrm{s}$ (see Supplementary Materials in [87]), which were believed to be caused mainly by intensity noise in the optical lattices. In addition, in clean systems we observed a heating onset on a timescale of $\sim 300\,\tau$ (around $\sim 2\,\mathrm{s}$, see Supplementary Information in [47]).

Before the beginning of the experiments in Part III, an optimization of the intensity stabilization of the optical lattices was carried out. This led to a considerable improvement in the isolation of our system, which would have otherwise made it impossible to observe the results described in Ch. 9. In particular, atomic losses are now negligible, with measurements of the single-atom lifetime showing a decay timescale of $\sim 600\,\mathrm{s}$. These lifetimes exceeding several minutes are expected to be limited by background-gas collisions and off-resonant scattering of light at $\lambda = 1064\,\mathrm{nm}$. Concerning intraband heating, we observed a depth-dependent heating on timescales always above $4000\,\tau$ (which can be more than $10\,\mathrm{s}$), and hence enhanced for higher tunneling J. The origin of this residual heating still remains to be identified, but we suspect it to arise from acoustic mechanical noise.

Part II

Disordered bosons: phases and dynamics

Chapter 4

Microscopy of dirty bosons

Quenched disorder is a fundamental ingredient in many real condensed matter systems, as generated by dislocations and impurities in crystals, but commonly absent in many simplified effective models. This can make a big difference in many systems, since a plethora of physical phenomena, such as the quantum Hall effect or Anderson localization, are a direct consequence of potentials with a disordered landscape.

In this chapter we will introduce the disordered Bose-Hubbard model and describe the main properties of its phases. We will then compare our experimental implementation, based on the engineering of site-resolved disordered potentials, with those in previous experiments with ultracold gases. Next, we will experimentally explore the effects of disorder close to equilibrium in our two-dimensional system. We will present and discuss experimental results obtained by using in situ and TOF imaging to identify some of the key features present in these disordered phases. Last, we summarize the conclusions from these experiments and mention possible extensions of this work.

4.1 The disordered Bose-Hubbard model

In the seminal paper in which the Bose-Hubbard model and its phases were introduced [55], the authors do not only discuss the clean case and the superfluid-to-insulator transition, but also consider a scenario in which quenched disorder, i.e. a frozen random potential, is present in the system. This is described by

$$\hat{H}_{\mathrm{dBH}} = -J \sum_{\langle i,j \rangle} \hat{a}_i^\dagger \hat{a}_j + \frac{U}{2} \sum_i \hat{n}_i \left(\hat{n}_i - 1\right) + \sum_i (-\mu_i + \delta_i)\, \hat{n}_i \,, \tag{4.1}$$

which is essentially the same Hamiltonian as in Eq. 2.1, but now δ_i is a local potential given by a certain random probability distribution (e.g. uniform, Gaussian, etc.). This is commonly referred to as the disordered Bose-Hubbard (dBH) model.

The original motivation to consider such disordered bosonic systems came in part from the experimental context of superfluid Helium-4 in porous media [98]. Those experiments studied thin films of Helium-4 in materials like Vycor glass, which have

a sponge-like structure with interconnected pores that can be randomly distributed in three dimensions. However, the importance of studying disordered interacting bosons goes way beyond this particular case. The competition between superfluidity, localization and interactions [99] leads to a rich diagram of insulating and conducting phases, the so-called "dirty-boson problem" [100].

4.1.1 Phases in equilibrium

In Ch. 2 we discussed that the (clean) BH model displays a quantum phase transition between two distinct phases: a *superfluid* (SF) phase, which displays long-range coherence and finite compressibility; and a *Mott-insulating* phase (MI), that is incompressible, with gapped spectrum and no superfluid order parameter. As we introduce finite disorder into the system, a new phase emerges: the *Bose glass*.

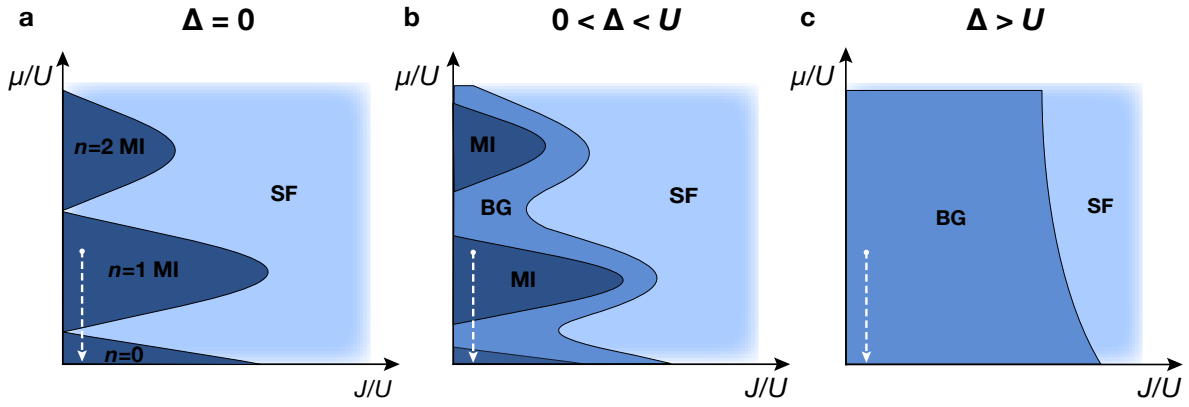

Figure 4.1: Phase diagrams of the dBH for fixed disorder strengths. a In the absence of disorder, the diagram shows only the clean SF and MI phases. **b** For a finite disorder, the BG intervenes between the MI and the SF as a Griffiths phase. **c** For sufficiently strong disorders, the MI phase is completely absent. The white dashed vertical arrow indicates the range of local chemical potentials μ_i that are probed in the experiments of Sec. 4.3 due to the inhomogeneity of the trap confinement.

Properties of the disordered phases

The Bose glass (BG) is an insulating phase with finite compressibility, vanishing SF order parameter and no gap [55]. One can think of it as a bunch of disconnected SF puddles. In the absence of coupling between these different SF pools, their phases will be uncorrelated, hence no long-range SF order. The vanishing gap allows for local excitations of these puddles, which locally display short-range coherence, but globally the system remains an insulator.

Concerning the SF phase in the dBH model, it is important to notice that, while it is still defined by the same superfluid order parameter, its features are a bit less robust than in the bare clean case. In general, one will deal with an inhomogeneous SF, which aside from a spatially dependent density distribution, will display a smaller, though finite, SF fraction [101, 102]. This means that the thermal SF-to-normal transition will happen at much lower temperatures, making it challenging for experiments to reach this regime.

In contrast, the MI phase remains robust for small disorders, and only eventually does the formation of SF puddles lead to a BG for strong interactions.

Table 4.1: Main properties of the three phases in the dBH model.

	Compressible	Superfluid Fraction	Spectrum
Superfluid	Yes	Finite	Gapless
Bose glass	Yes	Zero	Gapless
Mott insulator	No	Zero	Gapped

Shape of the phase diagram

A long-standing theoretical debate concerned the exact shape and topology of the dBH phase diagram. In particular, the question of whether there is a direct MI-SF quantum phase transition in the presence of disorder. While already early on this was argued to not be the case [55], it was only recently formally proven. The solution came from the so-called "theorem of inclusions" [103] and by the calculation of the 3D phase diagram via quantum Monte Carlo [101]. The theorem implies that any phase transition in a disordered system will display on each side of the transition rare regions of the competing phase. This means that the transition from a gapped phase to a gapless phases has to involve an intervening Griffiths phase [104], which in the dBH is the BG.

4.1.2 Experiments so far

While the original motivation for the dirty-boson problem stemmed from the study of superfluid helium films in porous glasses [98], ultracold bosonic gases have emerged as systems that can be almost ideally described by such bosonic models, though dirty phases have also been explored in solid-state disordered quantum antiferromagnets [105].

In an early experiment, a system of one-dimensional Bose gases was studied in the presence of a quasiperiodic potential, and the observation of a state with vanish-

ing long-range coherence and a flat excitation spectrum was taken as evidence of a Bose glass [106]. Later on, additional measurements showed signatures of an insulator phase surviving both at weak and strong interactions [43].

Other experiments explored both transport properties and coherence in three dimensions, observing a transition from a superfluid to a disordered insulator state [107]. In a second experiment, the SF-to-BG phase transition was explored by measuring excitations after performing a quench [108].

Certain aspects like the measurement of the density distribution or the realization of two-dimensional systems have been less explored so far. Our setup, which combines the ability to engineer site-resolved potentials and that of measuring the atomic occupations, is a great candidate for studying such kinds of disordered systems. In the remainder of this chapter, we will first introduce our implementation of quenched disorder, and then show and discuss experimental results obtained close to equilibrium.

4.2 Implementing quenched disorder

Quenched disorder has already been introduced in a vast variety of experiments with ultracold atoms, in particular to study Anderson localization of Bose-Einstein condensates in free space [109, 110] and disordered Hubbard models with bosons and fermions [46, 106]. A very common way to implement disorder in such systems involves random potentials using speckle-patterned light [111, 112], obtained by sending a laser beam through a diffuser plate.

In systems of atoms loaded in an optical lattice, a second approach consists in introducing an additional lattice with an incommensurate spacing [44, 106], which generates a quasiperiodic potential (sometimes misleadingly called quasirandom). An advantage of incommensurate lattices is that they generate a potential with subwavelength resolution, in contrast to the high autocorrelation lengths typically displayed by speckle potentials, set by the size of the speckle grains. At the same time they allow for a well-defined analytic formulation of the problem, as studied by Aubry and André [113]. Nonetheless, these potentials are strictly speaking not random, and display very special correlations.

In the experiments described in this thesis, we do not follow any of these two approaches. We instead make use of the high resolution of our imaging system, together with a DMD setup, to generate programmable site-resolved potentials. This means that we can effectively tune the values δ_i in Eq. 4.1, and thereby directly realize the dBH model. The details and limitations of this technique have already been described in Ch. 3, here we will just focus on the specific implementation of disorder and its

calibration.

In our experiments with two-dimensional disorder, we generate a 2D array of random numbers given by a uniform box distribution (based on a pseudorandom number algorithm) which sets the site-resolved grayscale distribution that will be programmed into the DMD. By using the MW spectroscopy technique described in Sec. 3.3.4, we can obtain the map of all the site-resolved resonances (see Fig. 4.2a) and use it calibrate the strength of the projected disorder. To do so, we first compute the distribution of the site-resolved resonances, and perform a fit with a skewed Gaussian function (see Fig. 4.2b), due to an asymmetry caused by the finite resolution. From the fit we can extract the variance of the distribution, and define the disorder strength Δ as the full width at half maximum (FWHM) of the distribution. Based on this calibration, we can tune the disorder strength in the experiment by modifying the intensity of the addressing laser, which should depend linearly on each other.

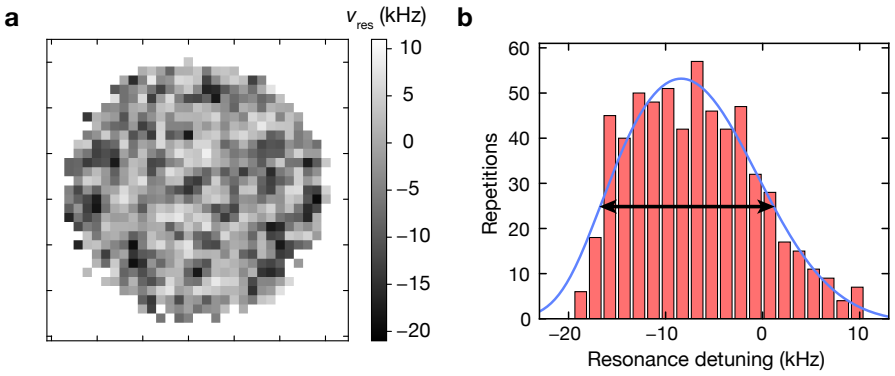

Figure 4.2: Calibration of the disorder strength. a Map of the fitted resonance frequencies in the system. **b** Histogram of the resonance frequencies (red bars) together with a fit of a skewed Gaussian (blue curve). The black arrows indicate the FWHM of the distribution, used to define the disorder strength Δ.

4.3 Measurements at strong interactions

In this section we microscopically observe the changes induced by the disorder in the strongly interacting regime. In particular, we will remain at $J/U = 0.01$, with an in-plane lattice depth of $V = 18\,E_r$, which corresponds to a deep MI phase in the clean case. As the disorder strength is increased, one expects that once Δ gets on the order of the Mott gap ($E_g \approx U$), the MI phase will become unstable, and a transition towards a BG phase will take place. This transition, driven by the competition between disorder and interactions, should be identifiable as the emergence of a compressible phase.

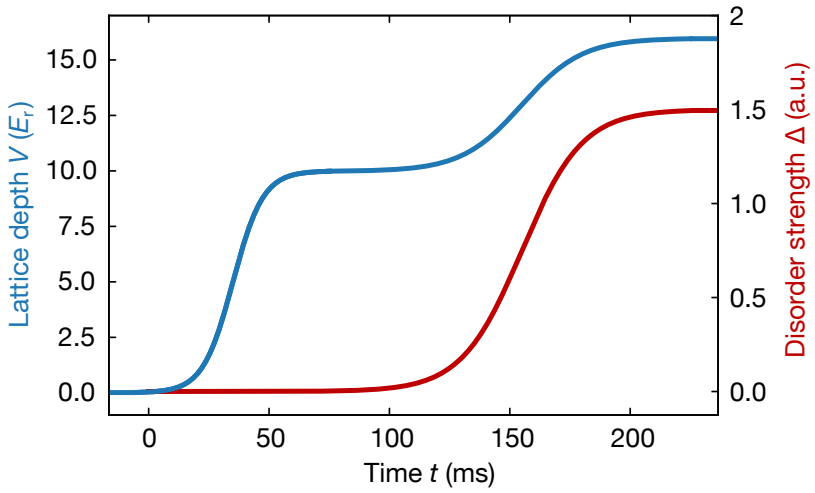

Figure 4.3: Ramp of the lattice depth and the disorder in the strongly interacting regime. Example of a sequence for preparing a disordered state with high interactions. The lattice depth (blue curve) is first ramped to $V = 10\,E_r$ in an s-shaped ramp of 75 ms and subsequently ramped to a deeper value in 150 ms simultaneously as the disorder strength ramp (red curve).

To experimentally prepare such a disordered state in a deep lattice, we ramp up both the in-plane lattices and the intensity of the disorder laser over a duration of 150 ms (see Fig. 4.3). By doing so, we avoid fast ramps in the regimes of slow dynamics. After the preparation, we proceed directly to take in situ imaging and obtain the site-resolved occupations. Concerning the disorder pattern in the DMD, it can be programmed to be either the same or different in each sequence. By repeating several snapshots with the same pattern α, we can obtain the mean occupation $\langle \hat{n} \rangle_\alpha$ and from several of those we can obtain the disorder-averaged

$$\overline{\langle \hat{n} \rangle_\alpha} = \frac{1}{N_p} \sum_\alpha \langle \hat{n} \rangle_\alpha , \tag{4.2}$$

where the overline indicates the average over several disorder patterns, with the total number of patterns being N_p. From now on we will refer to it using $n = \overline{\langle \hat{n} \rangle_\alpha}$ for simplicity.

In Fig. 4.4 we plot the 2D mean occupation for a single disorder pattern $\langle \hat{n} \rangle_\alpha$ (upper images), and for the pattern-averaged n (lower images), obtained from $N_p = 8$ different disorder patterns. As the disorder strength Δ is increased, we observe how the homogeneous density distribution in the center, typical of a unit-filling MI [9], gives

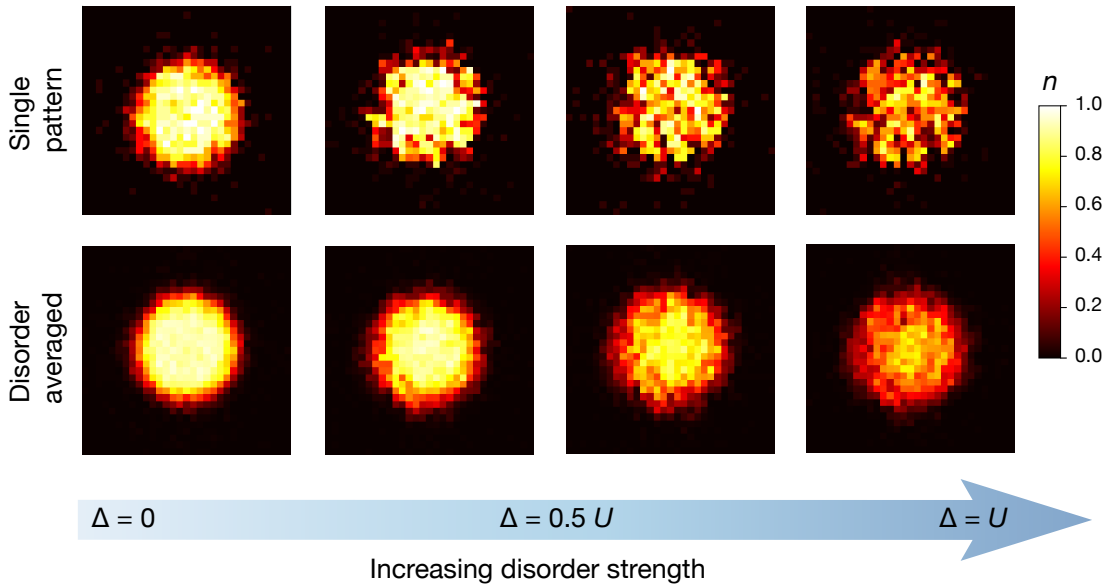

Figure 4.4: Transition from a MI into a disordered compressible state. Mean detected density at $J/U = 0.01$ for increasing disorder strength Δ. From left to right, $\Delta = 0.11\,U$, $0.45\,U$, $0.67\,U$, $0.9\,U$. The upper row shows the mean detected occupation obtained for the same disorder pattern $\langle \hat{n} \rangle_\alpha$. The bottom row shows the pattern-average of the mean occupation, n, obtained from averaging over 8 different disorder patterns. Any remaining inhomogeneities are associated to the finite number of patterns or to intrinsic features of the addressing beam.

birth to a seemingly random pattern of single-site densities, associated to the projected disorder potential. This tendency creeps in from the edges of the cloud, which correspond to the smallest local chemical potential μ_i (discussed in Sec. 2.2.3), as indicated by the white arrows in the phase diagram in Fig. 4.1. Only for $\Delta \sim U$ does the melting of the Mott insulator take place over the whole cloud. Looking at n, one can more clearly see the reduction in the mean detected atom number, beginning from the outer part of the cloud.

To obtain more insight into this transition, in Fig. 4.5 we plot the azimuthal average of the disorder-averaged density n and its variance σ^2 as a function of the radial distance from the center of the cloud. This allows one to observe how the initial squeezing in the central atom number, characteristic of the MI phase with $n \approx 1$ and $\sigma^2 \approx 0$, gets eventually destroyed by the influence of the disorder, leading to higher local fluctuations and hence an indication of a finite compressibility. In fact the profile obtained for the highest disorder strength, with $\Delta = 1.12\,U$, is reminiscent of the one

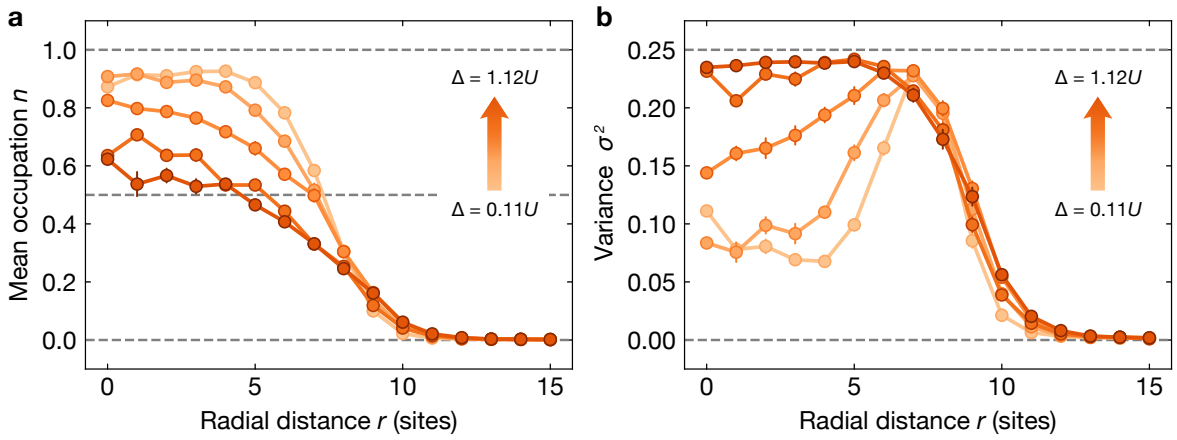

Figure 4.5: Density profiles for increasing disorder strength at strong interactions. **a** Density profile of the disorder-averaged mean detected occupation n and **b** its variance σ^2. The measurements were taken for $J/U = 0.01$, and the disorder strength values go through $\Delta = 0.11\,U$, $0.45\,U$, $0.67\,U$, $0.9\,U$, $1.12\,U$ (darker markers correspond to stronger disorder).

for a SF in the clean case [9].

4.3.1 Measuring the Edwards-Anderson parameter

Given that the BG phase shares properties with both the SF and the MI case, it can be challenging to unambiguously identify it. One cannot use a single order parameter to distinguish the three existing phases. Recently, it has been suggested that an analog of the so-called "Edwards-Anderson" (EA) parameter could be used as an order parameter for the BG [114, 115]. Originally defined in the context of spin glasses [116], the definition we use here in the BH model is

$$q_{\mathrm{EA}} = \overline{(\langle\hat{n}\rangle_\alpha - n)^2} = \overline{\langle\hat{n}\rangle_\alpha^2} - \overline{\langle\hat{n}\rangle_\alpha}^2, \tag{4.3}$$

where again $n = \overline{\langle\hat{n}\rangle_\alpha}$, and the overline always indicates an average over different disorder patterns. The EA parameter can be thought of as the fluctuation of the density distribution over different disorder distributions. In Fig. 4.6 we show the mean density distributions $\langle\hat{n}\rangle_\alpha$ for three different disorder patterns, which gives an intuition on the fluctuations that q_{EA} quantifies. The possible values of q_{EA} are bound by the detected variance σ^2, and therefore $0 \leq q_{\mathrm{EA}} \leq 0.25$.

In a non-disordered system, q_{EA} will, by definition, always be zero. This is no longer true in the presence of weak disorder, and the BG phase will always display a

finite value of q_{EA}. In the MI phase, however, the value of q_{EA} should vanish even for finite disorder strengths. This means that a rise of the EA parameter can be attributed to the transition from a MI to a BG phase. However, q_{EA} will in general also be finite for an inhomogeneous SF [115], and hence it cannot be established as an order parameter for the BG. Nonetheless, it remains a physically interesting parameter in disordered systems.

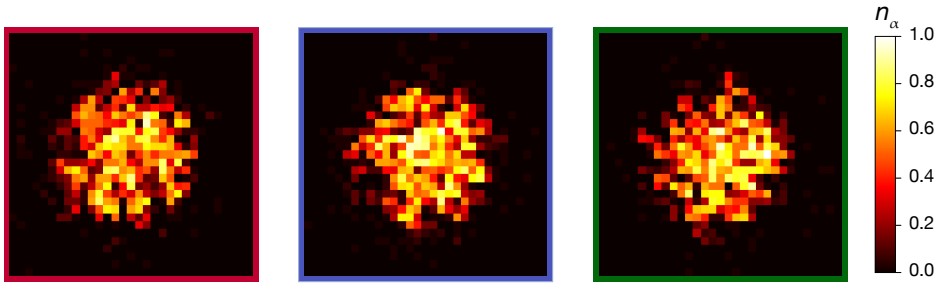

Figure 4.6: Mean detected densities for three different disorder patterns. 2D plots of the mean detected occupation $\langle \hat{n} \rangle_\alpha$ obtained for three different disorder patterns. The data was taken for a value $J/U = 0.01$ and with a disorder strength $\Delta = 0.9\,U$. The results reflect how, for sufficiently strong disorder, the distribution of the density can strongly differ for different programmed disorder patterns.

Our setup makes it possible to directly measure q_{EA} in the dBH. Here we present the first measurements in an experiment of the EA parameter and use it to qualitatively characterize the emergence of a BG phase as disorder is increased. In Fig. 4.7, we plot the site-resolved q_{EA} for three disorder strengths. One can see that at $\Delta = 0.11\,U$ (a) the measured parameter is essentially vanishing, at $\Delta = 0.45\,U$ (b) a strong increase emerges from the edges of the cloud and finally, at $\Delta = 1.12\,U$ (c) a finite value of q_{EA} penetrates also through the bulk.

In Fig. 4.7d we get a better quantitative insight of the values of q_{EA} by plotting their profile (similar to Fig. 4.5). We note that the highest measured value, $q_{\mathrm{EA}} \approx 0.06$, is below the theoretical maximum value of $q_{\mathrm{EA}} = 0.25$. This is a direct consequence of the finite temperature of our system. The dependence of q_{EA} on the temperature was numerically studied in [115], predicting an effect on the q_{EA} consistent with our observations at a temperature of $T \approx 0.15\,U$, measured from in situ thermometry in the clean case (see Sec. 3.2.4). As we mentioned earlier, a finite q_{EA} cannot be used to unequivocally distinguish a BG and an inhomogeneous SF. Nonetheless, at the strong interactions present in the system, in which no superfluid phase is expected, the observed signal suggests a state with the properties of a BG.

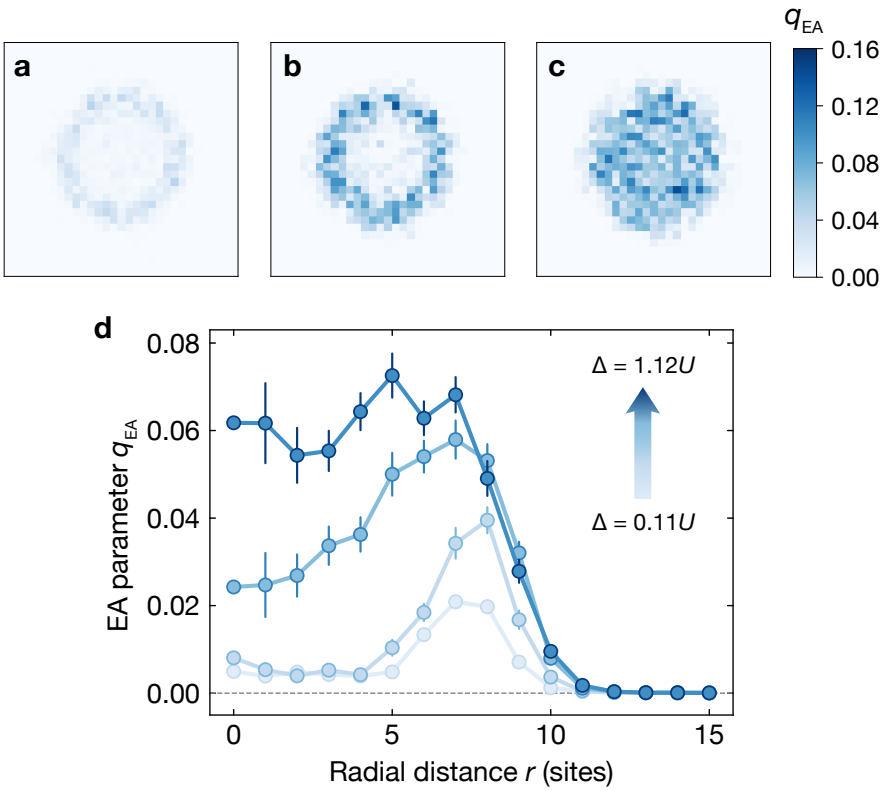

Figure 4.7: Measurement of the Edwards-Anderson parameter. 2D plots of q_{EA} at $J/U = 0.01$ for disorder strengths of **a** $\Delta = 0.11\,U$, **b** $\Delta = 0.45\,U$ and **c** $\Delta = 1.12\,U$. **d** Profile of the EA parameter obtained from an azimuthal average for disorder strengths $\Delta = 0.11\,U$, $0.22\,U$, $0.45\,U$, $0.67\,U$, $1.12\,U$ (darker markers correspond to stronger disorder).

4.4 Measurements at large tunneling

We now take a look at the effects of disorder in the regime of weak interactions and large tunneling. In the clean case, this implies starting from a homogeneous SF phase. We prepare the lattice depth at $V = 7\,E_{\mathrm{r}}$, for which $J/U \approx 0.22$. As one introduces disorder in the system, the density distribution of the SF should be strongly modified, giving rise to an inhomogeneous SF with a reduced SF fraction. Eventually, for even stronger disorders, one would completely suppress any long-range coherence and reach a BG phase [101, 102].

In Fig 4.8, we show the mean detected density for a fixed disorder pattern both for in situ and TOF imaging. The in situ pictures show how, as the disorder strength is increased (from left to right), the density shifts from an homogeneous distribution (in

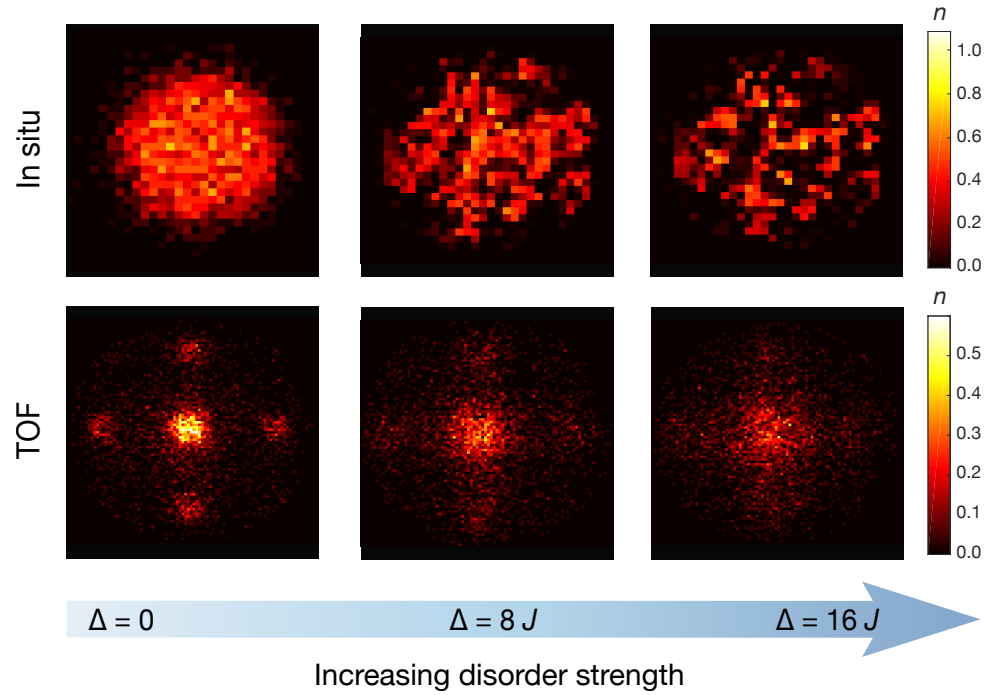

Figure 4.8: Decrease of the SF phase coherence and fragmentation of the density for increasing disorder. Measurements at $J/U = 0.22$ of the single-pattern mean occupation $\langle \hat{n} \rangle_\alpha$ for in situ imaging (top pictures) and TOF imaging (bottom pictures). The corresponding disorder strengths are $\Delta = 0\,J$, $5.5\,J$, $15\,J$ (from left to right). One can see that as the disorder strength Δ is increased, the homogeneity of the in situ cloud is lost, and the visibility of the coherence peaks is suppressed.

the clean case) to a more fragmented one, with many sites displaying a vanishing density. In TOF, one appreciates how the initial long-range coherence of the superfluid, characterized by the interference peaks, is strongly suppressed for higher disorder. Nonetheless, a visible cross-like pattern remains in the density.

From these two different observables, one can infer that the increase in the disorder induces a redistribution of the atomic density, due to a specific landscape of valleys and peaks, which leads to a shrinking in the SF fraction, related to a reduction in the global transport of the system. One can understand this in terms of a number-phase uncertainty relation, as already discussed in Sec. 2.1.1. The global phase of the system will only be well defined when the different clusters of fluctuating sites are coupled to each other via tunneling. That is to say a percolation between all the disconnected SF puddles [117]. The process of disconnection between the SF regions is precisely the

mechanism that eventually drives the transition from a SF to a BG phase.

To better characterize this effect, we calculate two suitable quantities, based on the data from a single disorder pattern, and study their dependence on the disorder. The first quantity is the interference visibility (defined in Ch. 3), which quantifies the phase coherence in the system. The second one is the local variance per site, σ^2, which we average in a region of interest in the center of the cloud. In Fig. 4.9 we show the dependence of these two quantities on the disorder strength. Both show qualitatively the same dependence, monotonically decreasing, indicating their relation and compatible with the view that sites with a well-defined phase will have high fluctuations. These quantities do not sharply identify any phase transition, and in fact the SF phase is expected to remain stable even for such high disorder strengths. However it is important to underline that a finite visibility does not necessarily imply long-range phase coherence, but is also an indicator of short-ranged coherence. Therefore the remaining signal, even for strong disorders, does not imply a survival of superfluidity, which could be hindered by our finite size and temperature.

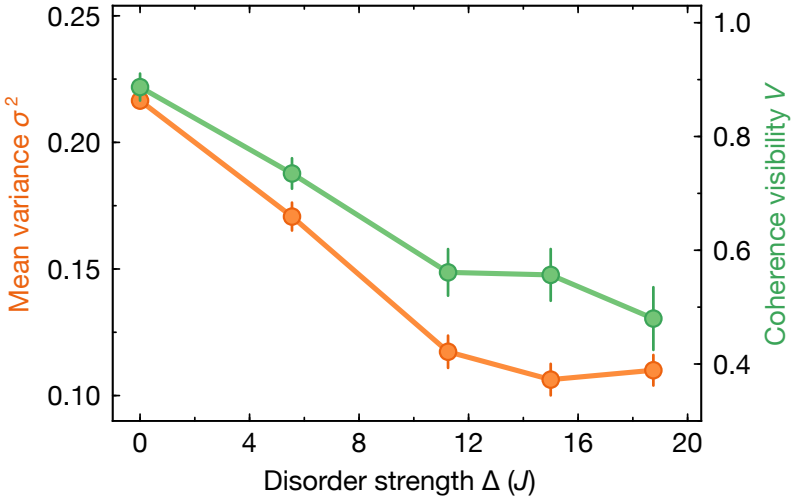

Figure 4.9: Decay of the interference pattern and the occupation variance for increasing disorder. Plot of the local variance, averaged over sites in the center of the cloud, (orange markers) and the interference visibility (green markers) as a function of the disorder strength Δ. The system is at $J/U = 0.22$, and the data was obtained from measurements with a single disorder pattern. One can see that both quantities show a similar dependence on the disorder strength, indicating the relation between the decrease of the long-range coherence and the fragmentation of the system.

4.5 Summary and outlook

To summarize, in this chapter we have studied the close-to-equilibrium properties of the dBH for the first time in a two-dimensional experiment. To do so we have implemented a novel approach to introduce disorder in experiments of ultracold atoms in optical lattices, based on a high-resolution objective and the use of a DMD to program arbitrary disorder patterns. With the available tools, we have explored different regimes of interactions, tunneling and disorder, and used our microscopy technique to get new insight into the local density of disordered bosonic systems, in contrast to previous measurements based on global observables [43, 106–108].

In the strongly interacting limit, this has allowed us to identify the appearance of a state with an enhanced occupation variance as one increases the disorder strength starting from a unit-filling MI. The observed behavior is consistent with the emergence of a BG phase as a result of the competition between disorder and interactions. In addition, we have performed the first measurement of the EA parameter, relevant for probing spin glasses [116], in a Hubbard system. We have identified that the emergent compressible phase displays a nonzero EA parameter, whose value increases as the disorder gets stronger.

Finally, we have also explored the regime of weak interactions. By combining our local probes with in-plane TOF measurements, we have been able to correlate a loss in the phase coherence of a SF with the fragmentation of its density distribution, induced by the presence of disorder. This observation is consistent with the transition from a SF to a BG phase, or with the formation of an inhomogeneous SF, which is also characteristic of the dBH model.

Among the possible future directions, the study of much larger disordered systems and with weaker harmonic confinement would be highly desirable. This would allow for a more precise measurement of the phase-coherence properties, better statistics due to single-shot disorder averaging, and particularly reduced finite-size effects in the vicinity of phase transitions. Another direction is the study of dynamics at low temperatures, which for example could directly probe transport properties of the different phases [118].

Chapter 5

Thermalization, ergodicity and MBL

The development of statistical mechanics has been extremely successful at linking concepts of microscopic physics with laws involving macroscopic observables. It has essentially made it possible to derive the laws of thermodynamics based on those of classical and quantum mechanics [31–33]. Nonetheless, many questions remain open in the field of non-equilibrium statistical mechanics, with much interest for many-body quantum systems. In this chapter we will introduce theoretical ideas from non-equilibrium physics of classical and quantum systems. Then we will look specifically at the problem of quantum thermalization in isolated quantum systems and how it leads to the eigenstate thermalization hypothesis. Last, we will discuss cases where quantum thermalization can fail, and focus on the phenomenon of many-body localization, which will be experimentally studied in the last two chapters of this part.

5.1 Basics of non-equilibrium physics

In many problems in thermodynamics and statistical mechanics we take for granted that we work with states in thermal equilibrium. However, the power of statistical mechanics can also be extended into the field of non-equilibrium physics, though a general framework to describe relaxation processes is still missing [33]. The typical scenario considered in this field is the preparation of a system in an out-of-equilibrium state, followed by its own dynamics which lead to its relaxation into thermal equilibrium. Some of the fundamental questions addressed are: *Which processes make a specific system undergo irreversible dynamics towards equilibrium? Are there systems which fail to equilibrate and, if so, why?* These two examples alone face several apparent paradoxes, such as the fact that irreversibility can emerge from (quantum) mechanical time-reversible processes (commonly referred to as *the arrow of time*), or that isolated systems can relax into a thermal state in the absence of an external bath.

5.1.1 Approach to equilibrium

Let us consider an isolated classical system. Typically, the microcanonical ensemble is used to derive its properties in equilibrium where we assume all microstates in

the same energy window are equally probable. This description of equilibrium states works very well, but provides no intuition into how classical dynamics takes a system from an initial arbitrary configuration through all the microstates of the ensemble. To gain some insight, let us consider a common textbook example: A gas of particles (maybe atoms or molecules) in a box where, after forcing them to a corner, they are released and evolve until they homogeneously occupy the whole box. Explaining the origin of this every-day intuitive behavior with a certain rigorousness can be very challenging. In Fig. 5.1 we consider a toy model of the gas in a box: the Hardy-Pomeau-De Pazzis (HPP) lattice gas automaton.[1] We prepare an initial state with a clear periodic density pattern and with random velocities, and plot the dynamics of the imbalance $\mathcal{I}$, which, in short, quantifies the visibility of the initial pattern, as a function of the number of steps. We see how the system evolves until it settles to a roughly constant value of $\mathcal{I} = 0$. Other initial distributions will also converge to this long-time state.

This simple deterministic model of many interacting particles already illustrates the approach to equilibrium of an out-of-equilibrium state. While the simulation does not explain why this process takes place, we can get an answer in terms of *typicality*. That is the fact that almost all the available microstates look macroscopically identical (homogeneous density), and if we start in a configuration with an *atypical* macroscopic observable (e.g. a density imbalance) it will naturally evolve into a *typical* configuration [33].

5.1.2 Ergodicity and integrability

"Ergodicity" is another important concept to understand relaxation processes. A system is said to be ergodic whenever the time-average of a macroscopic observable O is equal to the ensemble average. That is

$$\overline{O(t)} = \frac{1}{N}\sum_i O_i, \tag{5.1}$$

where the overline indicates here a long-time average, i labels each independent configuration of the ensemble, and N is the total number of configurations. In this sense, thermalization happens as the system dynamically explores all possible configurations. In the above example of a gas in a box, ergodicity is fulfilled, since the long-time average of the imbalance is equal to the average over all possible density configurations.

[1] The HPP lattice gas automaton is a dynamics model for fluids in 2D, which considers particles in a square lattice with four possible velocities [119]. The model is deterministic and made out of propagation and collision steps.

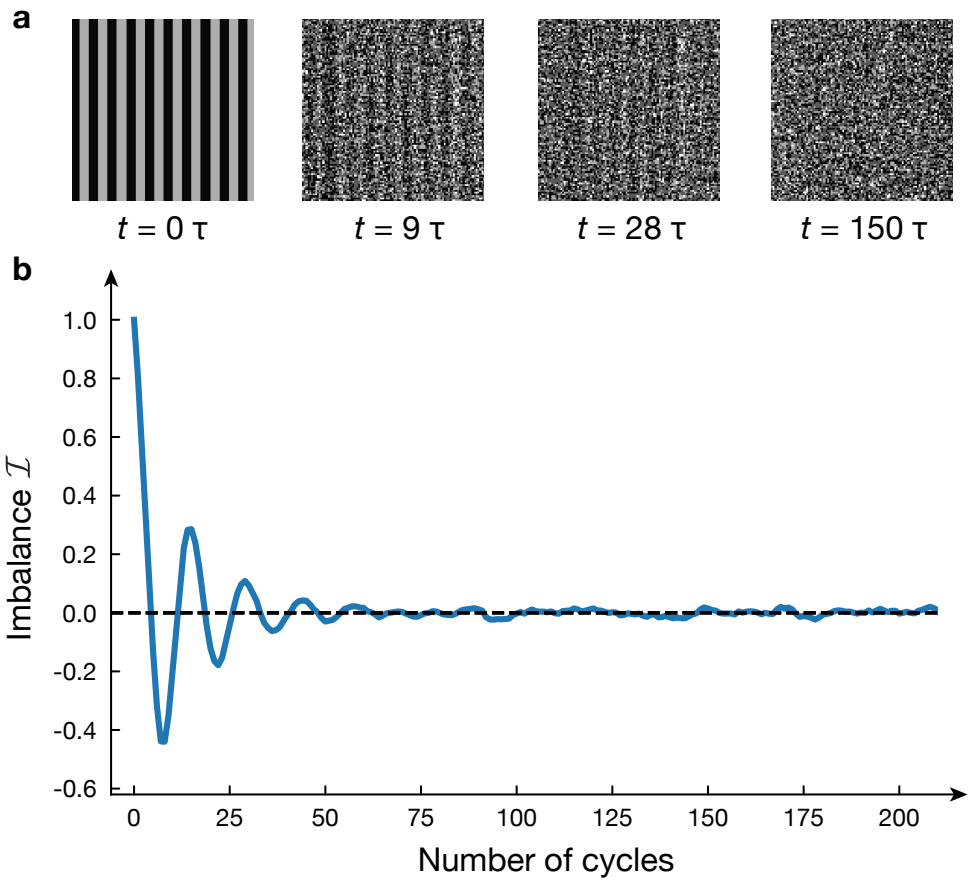

Figure 5.1: Classical relaxation dynamics based on an HPP model. a Individual snapshots of the density for four different evolution times. **b** Plot of the density imbalance $\mathcal{I}$, which quantifies the visibility of the initial density pattern, as a function of the number of evolution cycles. The simulation was done in a square lattice with 100×100 sites and a total of 10^4 particles organized in stripes of 5 sites of length.

Should we expect all systems to display ergodicity and hence to thermalize? In ergodic classical systems, a common property is chaotic dynamics. In the lattice gas example, a change in the initial velocity of a single particle will lead to a significantly different long-time evolution. One can also see this with a single billiard ball bouncing against the walls of a stadium-shaped container, which will end up exploring the whole phase space [33]. Such chaotic dynamics vanish in systems with an extensive number of independently conserved quantities, i.e. integrals of motion. Integrable systems show a breakdown of ergodicity due to restrictions on the available trajectories. A billiard ball bouncing in a circular container will show non-chaotic dynamics,

and will not explore the whole phase space. This non-ergodicity can also happen in more complex interacting systems, as for example in the Fermi-Pasta-Ulam-Tsingou problem. In their numerical experiment, considered the first computer-based simulation ever, they found an absence of thermalization in the modes of a nonlinear string [120].

5.2 Quantum thermalization

Let us now consider the approach to equilibrium in many-body quantum systems. At first, it seems like the conflict between the microscopic and macroscopic dynamics will only be amplified in the quantum case. After all, the evolution by the Schrödinger equation is linear, and if we consider a single eigenstate, this evolution is in fact a trivial one. In this section we will see that, in a way, recent developments have left a clearer picture for quantum thermalization than for its classical counterpart [31–33].

In quantum statistical mechanics it is common to consider a system of interest coupled to an external heat reservoir (see Fig. 5.2a), allowing for an exchange of energy and particles. This configuration naturally brings our system into thermal equilibrium, as described by a thermal density matrix $\hat{\rho}_{\text{th}}$ in the canonical (Gibbs) ensemble. But how is thermal equilibrium reached if we consider an isolated quantum many-body system? One might consider full isolation to be unrealistic, but the same problem can be reached when absorbing the external heat reservoir into the system.

Starting the system in a pure state, described by a density matrix $\hat{\rho}(0)$, it seems clear that unitary dynamics will not modify the global purity of the system and that it cannot reach a thermal state $\hat{\rho}_{\text{th}}$. To solve this apparent paradox, one should consider the thermalization of a *local* physical observable instead [30]. In fact, when we consider a thermodynamic system, it should be clear that measuring global operators does not make physically sense. The relevant object to keep track of, given an operator that acts on a finite region of the Hilbert space A (see Fig. 5.2b), will be the density matrix $\hat{\rho}_{\text{A}}(t) = \text{Tr}_{\text{B}}(\hat{\rho}(t))$ (where B is the remainder of the system).

Quantum thermalization takes place then when $\hat{\rho}_{\text{A}}(t) \approx \hat{\rho}_{\text{A,th}}$. A globally pure system can look thermal locally (in A), whenever the remainder of the system (B) can efficiently act as a thermal bath for it. Assuming we start with a system that looks initially pure in A, e.g. a product state, the generation of entanglement between A and B will be the process driving its thermalization, and leads to a spread of initially local information and dephasing [34, 121].

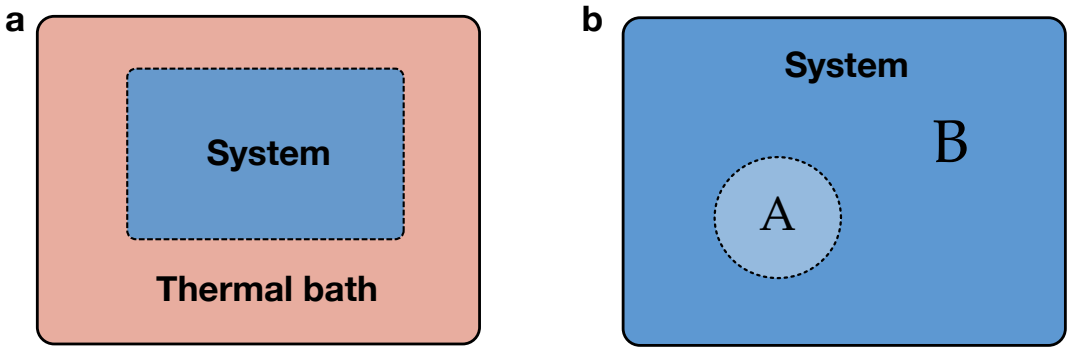

Figure 5.2: Two different approaches to quantum statistical mechanics a The scenario most commonly considered is a system coupled to a reservoir with which energy and particles can be exchanged. **b** The scenario of a single isolated quantum system, where the observables of a region A can thermalize if the remainder B acts as an effective bath.

5.2.1 The eigenstate thermalization hypothesis

Let us consider the out-of-equilibrium dynamics of a pure system. We start with an eigenstate $|\psi_0\rangle$ of the initial Hamiltonian $\hat{H}_0$. We then quickly change to a new Hamiltonian $\hat{H}$, and we can reexpress $|\psi_0\rangle$ as a superposition of the eigenstates of the new Hamiltonian:

$$|\psi_0\rangle = \sum_\alpha c_\alpha |\phi_\alpha\rangle, \tag{5.2}$$

which leads to the time evolution of the state

$$|\psi(t)\rangle = e^{-i\hat{H}t/\hbar}\,|\psi_0\rangle = \sum_\alpha c_\alpha\, e^{-i\epsilon_\alpha t/\hbar}\,|\phi_\alpha\rangle. \tag{5.3}$$

The time evolution of some observable $\hat{A}$ will be given by

$$\langle \hat{A}(t)\rangle = \langle\psi(t)|\,\hat{A}\,|\psi(t)\rangle = \sum_{\alpha,\beta} c^*_\alpha c_\beta\, e^{i(\epsilon_\alpha-\epsilon_\beta)t/\hbar}\,A_{\alpha\beta}, \tag{5.4}$$

where $A_{\alpha\beta} = \langle\phi_\alpha|\,\hat{A}\,|\phi_\beta\rangle$. Note that if we look at the average of $\langle\hat{A}(t)\rangle$ over long times, the exponential term will average to zero for any oscillating phase, i.e. $E_\alpha \neq E_\beta$, and hence one obtains

$$\overline{\langle \hat{A}(t)\rangle} = \sum_\alpha |c_\alpha|^2\, A_{\alpha\alpha}. \tag{5.5}$$

Quantum thermalization emerges from this last step. From Eq. 5.5 it is clear that the long-time average of the observable will only depend on the weights of each eigenstate $|\phi_\alpha\rangle$. This is commonly referred to as the "diagonal ensemble". If the system thermalizes at long times we expect the average obtained from this diagonal ensemble to coincide with the one from a microcanonical ensemble with energy E_0, defined as

$$\langle A\rangle_{\mu c} := \frac{1}{N}\sum_{\alpha'} A_{\alpha'\alpha'}, \tag{5.6}$$

where the sum is taken only over the N eigenstates that fulfill $|E_0 - \epsilon'_\alpha| < \delta E$. Therefore the condition for the thermalization of the system can be written as

$$\overline{\langle \hat{A}(t)\rangle} = \langle A\rangle_{\mu c}. \tag{5.7}$$

Given that the left hand side of Eq. 5.7 explicitly depends on the initial conditions (via the coefficients c_α), while the right hand side is only fixed by the energy of the state E_0, one needs to find a mechanism that makes this equality fulfilled. One possible way is for the diagonal elements $A_{\alpha\alpha}$ close in energy to only weakly fluctuate. In that case, $A_{\alpha\alpha}$ can be taken out of the sum in Eq. 5.5, and the dependence on the coefficients c_α is effectively gone, since the sum of probabilities must add up to 1. This is in fact the main idea behind the so-called "Eigenstate Thermalization Hypothesis" (ETH) [35–38], which can be stated as:

The expectation value of the (local) observable $\hat{A}$ for a single eigenstate with energy E_α is the same as the predicted by a microcanical ensemble around that same energy:

$$A_{\alpha\alpha} = \langle A\rangle_{\mu c}. \tag{5.8}$$

A consequence of ETH is that local observables of individual eigenstates will smoothly depend on their eigenenergies. And its name can be better understood by considering each one of the individual eigenstates already to be a "thermal" state. Even though an initial pure state can look far from equilibrium (due to the coherence between eigenstates set by its coefficients c_α), the long-time dephasing will reveal the previously hidden thermal properties of the involved eigenstates.

While ETH is only a hypothesis, there is wide numerical evidence in many models and also analytic results [33, 38]. Additionally, many experiments, in particular with ultracold atoms [22], have considered the study of thermalization and relaxation dynamics in isolated quantum systems [26, 39, 122], providing evidence of quantum thermalization in different ways. In the next subsection we will, however, discuss specific cases in which ETH does not hold at all.

5.2.2 Breakdown of ETH

Similar as in our discussion of classical ergodicity, we will see that there are few models that violate ETH. These systems fail to serve as a bath for their subsystems, and because of this they are of fundamental interest. Let us go through some known examples of models and also mention few experiments in which quantum thermalization seems to fail.

Integrable systems

Similarly as in the classical case, the existence of integrals of motion in a quantum system lead to restrictions of its otherwise ergodic behavior. This usually takes place in low-dimensional systems such as models of hard-core bosons in 1D [123]. This kind of breakdown of ergodicity is, however, fine-tuned, in the sense that as a single parameter shifts the system away from integrability, thermalization might end up taking place, though potentially over arbitrary long timescales [124].

Few experiments with 1D Bose gases have addressed these kinds of systems. The early article *A quantum Newton's craddle* [24] triggered many theoretical discussions, and over the last few years other similar experiments have observed prethermalizing dynamics [27] or the emergence of thermalization due to integrability-breaking interactions [125].

Anderson-localized systems

In single-particle systems, the influence of quenched disorder can lead to a breakdown of its transport properties. This can be directly seen in a tight-binding model with diagonal disorder, as originally considered by P. W. Anderson [40], for which both the eigenstates and the dynamics can display full localization. In such disordered systems there is a strong suppression of the transport and therefore a breakdown of quantum thermalization.

Anderson localization has been experimentally observed with matter waves, i.e. Bose-Einstein condensates, in disordered optical potentials [109, 126]. But as a wave phenomenon, it has also been explored in many other experiments involving the localization of light [127], microwaves [128] or sound waves [129].

Many-body-localized systems

Extending Anderson localization beyond the non-interacting limit has been the focus of a lot of recent research, though Anderson already speculated on this possibility in his original work on single-particle localization [40]. Localization has been shown to survive for high-enough disorder strengths and moderate interactions [41, 42]. This is a very significant result, since it implies that there is a generic type of quantum

many-body systems that exhibit a failure of thermalization even at finite energy densities [34]. This contrasts with the two examples above, which were either fine tuned to integrability, or to a non-interacting scenario. Additionally, it promotes many-body-localized states to a new phase of matter. The properties and phenomenology of many-body localized systems will be discussed in detail in Sec. 5.3.

Quantum many-body scars

A new kind of non-thermalizing possibility has recently emerged, though currently still at the center of much debate, the so-called "quantum many-body scars" [130]. The motivation emerged from the results of a recent experiment with Rydberg-atom arrays [131]. The main observation was a lack of thermalization for certain high-energy states (leading to an almost undamped periodic oscillation) in contrast to an efficient thermalization for other states at similar energies. The situation might emerge from a small set of eigenstates that violate ETH, even though most of the other eigenstates of the spectrum do follow ETH. Given the recent emergence of this phenomenon, a full understanding of its mechanism is not yet present, though some connection to integrability is likely to be behind it.

5.3 The many-body-localized phase

Let us begin by reemphasizing some of the features of many-body localization (MBL) that make it so unique. Systems exhibiting MBL display a nonergodic behavior far from equilibrium, and because of their violation of the ETH, they resist to be described by the formalism of quantum statistical mechanics. This places the phenomenon in a very singular context, and it signifies the emergence of a new phase of matter and of a new kind of quantum phase transition: an *eigenstate phase transition*. This means a phase transition that instead of corresponding to a change of its properties in thermal equilibrium, it corresponds to a change in all of the eigenstates of a many-body Hamiltonian.

By modifying one parameter of the Hamiltonian, e.g. the disorder strength or the interactions, it is possible to cross from an ergodic phase that satisfies ETH to a localized one where ETH fails. While localization-delocalization transitions are common in many disordered models in the low-temperature limit, MBL can also exist at finite energy densities above the ground state. This means that in contrast to a conventional quantum phase transition, which strictly takes place at $T = 0$, the MBL-ergodic phase transition can happen even at infinite temperatures [132]. A common approach to study the properties of the MBL phase transition is the exact diagonalization of small systems, successfully implemented to a range of different models, such as spinless fermions [132] or Heisenberg [133, 134] and Ising spin models [135].

While the phenomenology of MBL is fundamentally interesting on its own right, another dramatic consequence of these properties is that MBL may enable quantum order that is protected by localization even at finite energy densities [135–137]. This goes beyond the thermal-MBL phase diagram, and it can display more than a single localized phase, each one of them identified by a different order parameter. This also connects to the possibility of stabilizing phases of matter in periodically driven systems [49], which we discuss in more detail in Ch. 8.

5.3.1 Properties of the ergodic and localized phases

In this subsection we review few phenomenological properties of the MBL phase and contrast them with the characteristics of the ergodic phase. The discussion will focus either on out-of-equilibrium states or individual eigenstates with finite energy densities, to avoid any ground-state effects.

Eigenstate properties

On the ergodic side, the eigenstates are thermal and obey the ETH. This implies that as the system size diverges, the reduced density matrix of finite subsystems will be thermal. Another consequence is that the entropy of entanglement will scale proportional to the size of these subsystems, i.e. it follows a "volume law".

On the localized phase, the eigenstates are not thermal and therefore ETH does not apply. As those states cannot serve as a heat bath for their subsystems, their entanglement is only short-ranged and their entropy of entanglement obeys an "area law". Note that even in non-disordered local Hamiltonians, area laws are a generic property found in ground states [138]. In some sense, MBL extends ground-state physics to all temperatures.

Eigenstate structure

While the difference between the dependence of the entropy of entanglement in the two phases can be used to identify them, this is in practice hard, since it requires to study different sizes of the same system. A very common approach used instead is to study the spectral statistics of adjacent energy levels. In the ergodic phase, the eigenstates obey the Wigner-Dyson statistics of random matrix theory (given by the Gaussian orthogonal ensemble). This is due to the level repulsion, a property associated to systems with quantum chaos [33]. On the other hand, in the strongly localized limit, eigenstates with nearby energies will in general have almost no overlap in Fock space with each other, such that they will not interact and hence level repulsion is absent [132]. The distribution of eigenenergies is instead given by a Poissonian distribution.

Another property that one can directly observe in the eigenstate structure, and which is a direct implication of ETH (as discussed in Sec. 5.2), is the dependence of a local observable as a function of the energy. In an ergodic system, we expect these observables to change smoothly through the spectrum, as required by ETH. However, in the MBL phase local observables might strongly fluctuate for eigenstates arbitrarily close in energy [49].

Memory of the initial conditions

Aside from the direct eigenstate properties, let us now discuss the phenomenology in the dynamics of far-from-equilibrium states. First note that a direct consequence of thermalization is the erasure of the system memory concerning certain initial conditions. In quantum thermalization, this means that local information of an initial state will spread through the whole system and thereby remain hidden (since unitary evolution cannot erase that information) [34]. Because of this, any initial distribution in which we prepare an out-of-equilibrium state will fade once the system thermalizes.

In contrast, in MBL systems a partial memory of the initial conditions can survive locally for arbitrary long times. Because of this, the study of long-time dynamics can be used to distinguish a thermal from a localized non-equilibrium state. This property is particularly used in experiments exploring MBL, as we will discuss in the following chapter.

Spread of entanglement

Finally, let us take a look at the dynamics of the bipartite entropy of entanglement after a quench to an out-of-equilibrium product state. If the system is ergodic, the entropy of entanglement will quickly increase, in a ballistic fashion [139], until it saturates to an entropy that will be proportional to the number of degrees of its subsystems (again a volume law).

In the MBL phase, the entropy monotonically increases after long times only in a logarithmic fashion [140]. The entanglement entropy to which it eventually saturates will actually obey a volume law, but have a smaller value than in the ergodic case. This is a key property that distinguishes the physics of MBL from that of Anderson localization. In the latter, there is no such monotonic increase of the entanglement entropy for long times, indicating the role of interactions in the phenomenon of MBL.

Chapter 6

Probing ergodicity and localization in the 2D BH model

In this chapter we show how our quantum-gas microscope can be used to explore thermalization and MBL in the two-dimensional BH model, and present experimental results showing signatures of these phenomena. We start by motivating some of the strengths of our system and comparing it to previous and current experiments concerning MBL. Then we proceed to describe how the available tools in our setup are used to prepare an out-of-equilibrium initial state and for its local measurement. In the following section, we show data of measured dynamics in a system with a domain-wall initial state, showing signatures of a long-lived memory of the initial conditions, and also observe its dependence on the density of the system. We continue the experimental results by studying the dependence of the observed features in systems with a different initial density modulation. This allows to get more insight into the relation between the localization length in the system and the measured observable, the "imbalance". Finally, we discuss possible future experiments and additional models that can be directly studied in our setup.

6.1 Experimental motivation

Because of the fundamental implications that MBL has in the field of quantum statistical mechanics, the possibility of experimentally realizing such MBL phases is very exciting. The fact that MBL appears in quite generic models, i.e. locally interacting systems with quenched disorder, and that it can be observed at finite temperatures, means that the phenomenon can be realized in many diverse experimental platforms. Aside from systems of ultracold atoms in optical lattices [44–47], experiments with chains of trapped ions [141, 142], superconducting circuits [143–145] or solid-state spin systems [146] have also observed signatures of MBL in very different regimes.

While the high level of controllability in some of these platforms (with the goal of quantum computation) makes them great for arbitrary preparations and measurements, there are two main reasons that put ultracold atoms at the forefront of exper-

imentally exploring MBL. The first one is their great level of isolation, allowing one to explore thousands of tunneling times [87, 147]. The second one is a higher degree of scalability, which makes it possible to work with system sizes on the order of hundreds [47] or even thousands [48] of lattice sites. Both long evolution times and big system sizes are features that make classical computer simulations of these systems extremely hard, especially in the far-from-equilibrium regime. These reasons make it strongly desirable to use ultracold atoms as analog quantum simulators of MBL models and their phase transitions.

The experiments performed in this and the following chapter describe out-of-equilibrium experiments in a two-dimensional disordered Bose-Hubbard model with hundreds of lattice sites and particles. In addition to the dimensionality and the size of the system, the bosonic nature also adds a level of complexity. While in general it is true that in these high-temperature states quantum statistics play a negligible role, in practice higher occupations (e.g. $n = 2,3...$) can be achieved, and it also leads to an enhancement of interaction effects.

6.2 Description of our approach

In this section we explain the main ideas behind our approach to study thermalization and MBL, including the experimental techniques and its theoretical interpretation. In a nutshell, we will be combining our ability to realize the disordered BH model, which we already described in Ch. 4, with a fast quench of the lattice depth. The preparation of a well-defined initial state with a specific density modulation, typically stripes of occupied and unoccupied lattice sites, will be used as a initial-condition reference, whose visibility can be microscopically tracked after a certain evolution.

We will first formally discuss the prepared quantum states and their dynamics, and then provide a summary of the main procedures carried out in our setup concerning the preparation, evolution and imaging of out-of-equilibrium states.

6.2.1 Formal description

We begin by introducing the starting point of the experiment, a unit-filling MI in the atomic limit, whose quantum state is

$$|\Psi_{\mathrm{MI}}\rangle = \prod_j \hat{a}_j^\dagger |0\rangle, \tag{6.1}$$

and which can be reached by preparing the ground state of $\hat{H}_{\mathrm{BH}}(J = 0)$. In the next step, we proceed by selectively removing the bosons sitting in a subset of all lattice

sites B,

$$|\Psi_{\mathrm{DP}}\rangle = \hat{\mathrm{D}}_B\,|\Psi_{\mathrm{MI}}\rangle = \left(\prod_{l\in B}\hat{a}_l\right)|\Psi_{\mathrm{MI}}\rangle = \prod_{j\in A}\hat{a}_j^\dagger\,|0\rangle, \tag{6.2}$$

thereby preparing a density-patterned (DP) product state $|\Psi_{\mathrm{DP}}\rangle$, with particles only occupying the sites in A (the remainder of B). This state with all particles well localized in individual sites, will be the initial state of our dynamics, $|\Psi(t=0)\rangle = |\Psi_{\mathrm{DP}}\rangle$.

Now we continue by performing a quench of the Hamiltonian to that of Eq. 4.1. This means that we suddenly tune to a finite value of J and introduce a disorder pattern α with strength Δ. This directly leads to the time evolution

$$|\Psi_\alpha(t)\rangle = e^{-i\hat{H}_{\mathrm{dBH}}t/\hbar}\,|\Psi_{\mathrm{DP}}\rangle. \tag{6.3}$$

which will depend on t, the Hamiltonian parameters and the initial density pattern, characterized by the subset of occupied sites A.

After a certain evolution time t, we can proceed to measure the state of the system. While there are several interesting observables, here we will focus on the imbalance operator $\hat{\mathcal{I}}$, which we define as

$$\hat{\mathcal{I}} = \frac{\hat{N}_A - \hat{N}_B}{\hat{N}_A + \hat{N}_B}, \tag{6.4}$$

where $\hat{N}_{A(B)}$ is the operator for the total atom number in region $A(B)$, defined as $\hat{N}_{A(B)} = \sum_{j\in A(B)}\hat{n}_j$. Now we can compute the disorder average of the expectation value as

$$\mathcal{I}(t) = \overline{\langle\mathcal{I}(t)\rangle_\alpha} = \overline{\langle\Psi_\alpha(t)|\,\hat{\mathcal{I}}\,|\Psi_\alpha(t)\rangle}. \tag{6.5}$$

Note that, by definition, $\mathcal{I}(t=0)=1$. In the clean system, we expect the evolution of the system to eventually lead to a quantum thermalization of the state, and hence to $\mathcal{I}(t\to\infty)=0$. This is taken as evidence of the system being in the ergodic phase, and particles fully delocalizing over the entire system. However, in the presence of strong quenched disorder, MBL can emerge, which we can identify by $\mathcal{I}(t\to\infty)>0$, which implies a remaining memory of the initial density pattern.

This measured observable, the imbalance, is model-free and is equivalent to the correlation with the initial state at $t=0$, $\hat{C}_i(t) = \hat{n}_i(t)\cdot\hat{n}_i(0)$, which is commonly used in theoretical simulations with arbitrary initial product states [148].

6.2.2 Experimental implementation

Now let us summarize how the procedure introduced in the previous subsection is routinely implemented in our experimental setup.

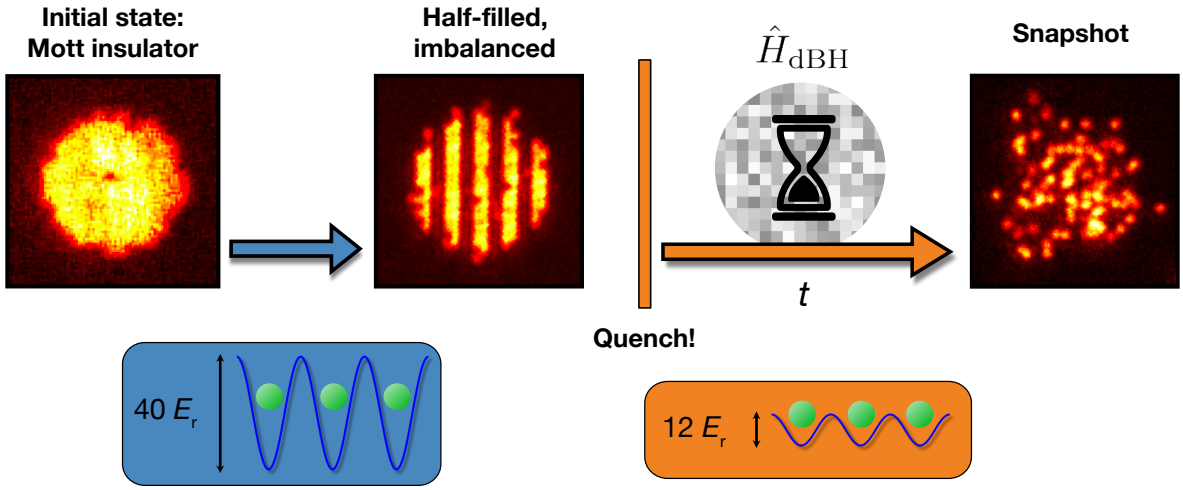

Figure 6.1: Schematic overview of the experimental sequence. An initial unit-filling MI, deep in the atomic limit (red box), is prepared into a certain density pattern by removing the atoms in some regions. Subsequently we proceed with the quench by turning on the disorder and suddenly ramping down the in-plane lattices (yellow box). After a certain time t of dynamics under the dBH Hamiltonian, we ramp up the lattices again and proceed to image the occupations in the system.

Initial state preparation and quench

The first step in the experiment involves the preparation of a two-dimensional unit-filling MI, with typically an atom number of $N \approx 240$. The lattices are then ramped to a depth of 40 E_r, in the deep atomic limit, to ensure that no particles tunnel during the preparation of the density-patterned state. For this, we program the DMD with a specific pattern, such that only half of the lattice sites (region B) will be illuminated. Next, we use our single-site MW addressing techniques (described in Ch. 3), to selectively transfer the illuminated atoms into a different state, and afterwards optically remove them. This process takes the system into a half-filling configuration, and already far from its original state close to "zero temperature".

In the next step, we use a MW π pulse to transfer all the remaining particles from the hyperfine state $|F = 1, m_F = -1\rangle$ to the $|F = 2, m_F = -2\rangle$, which is repulsively affected by the light shift of the addressing laser. Then, we first reprogram the DMD to a grayscale disorder pattern (see Ch. 4) and then we slowly ramp the intensity of the laser sent through the DMD to the atoms (in approximately 150 ms) until it reaches a specific disorder strength Δ. Note that since we are still in a quite deep lattice, the introduction of the disorder potential will generally not induce any tunneling dynamics.

In the last part of the preparation, we perform a quench in the system by ramping down the in-plane lattices from 40 to 12 E_r in less than a millisecond. While this is a fast quench respect to the Bose-Hubbard dynamics, it is essentially adiabatic with respect to the band degree of freedom, and hence no transfers into higher bands take place.

Evolution and subsequent imaging

After performing the quench, the system is allowed to evolve for a certain time t under the dBH Hamiltonian of Eq. 4.1. At 12 E_r the tunneling strength is set to a value of $J/\hbar = 2\pi \times 24.8\,\mathrm{Hz}$ and the interactions to $U = 24.4\,J$ (see App. A). To ensure the coherence of the dynamics, it is particularly important to ensure a good isolation during this stage. The typical measured timescales go beyond few $100\,\tau$ ($\sim 600\,\mathrm{ms}$), where $\tau = \hbar/J$ is one tunneling time.

After a certain evolution time t, we proceed to image the occupation in the lattice sites of the system, following the description in Sec. 3.2.3. From the reconstructed lattice-site occupations one effectively measures the observable $\hat{\mathcal{I}}$, and by repeating the experiment several times and with different disorder patterns we can obtain the quantity $\mathcal{I}$, and hence estimate the visibility of the initial pattern.

In most experiments, we directly take the disorder averaging by preparing a different disorder pattern in each individual measurement. This ensures that our observations are not limited by a finite amount of disorder patterns. To compute the imbalance, we typically consider a region of interest (ROI) of 100 lattice sites in the center of the cloud. This has the advantage that one can focus on the most homogeneous region of the system, since the harmonic trap might induce additional localization effects in the edges of the cloud. This contrasts with other experiments without in-situ resolution of the imbalance, where one effectively averages different regions of the trap. Concerning the light-induced losses in our imaging, leading to parity-projection (see Ch. 3), they will cause the measured imbalance to be strongly affected in the presence of higher occupations. Because of this, it is desirable to work in strongly interacting regimes, – in this experiment $J/U \approx 0.04$ parameters– where only a small number of doubly occupied sites are present.

Estimation of the energy density

A requirement for the study of far-from-equilibrium phenomena, such as MBL, is for the prepared states to be at finite energy densities. In real experiments, it is generally not straightforward to characterize the effective temperature after a quench, since it requires knowledge of the entire spectrum. We nonetheless bring up few arguments to bring confidence on the high energy density in the system, and its position in the many-body spectrum.

Let us consider first the single-particle case in an homogeneous lattice. We note that preparing a single particle localized in a single lattice site (a Wannier-like state) corresponds to populating all kinetic energy states of that particle (all Bloch waves). Now we consider a system of hard-core bosons at half filling, which in fact is a good approximation of our system for $\Delta = 0$, since $U > 16J = 2 \times E_{\mathrm{BW}}$. Assuming all bosons are initially prepared in a state localized to a single site, the energy of the prepared state will be exactly in the middle of the many-body spectrum, thereby corresponding to the energy at infinite temperature. Additionally introducing a disordered landscape in the system will (on average) not modify the previous conclusion, since the localized particles will randomly sample the disordered potential.

Following similar arguments, one can extrapolate this result to a system also displaying few doubly occupied sites. In this sense one can always define an effective maximum local Hilbert space dimension, which suffices to describe the system, and consider the energy density with respect to the spectrum of that model. In addition to these theoretical arguments, quantitative estimations of the energy density and effective temperature were provided in the supplementary material of [87] for our experimental parameters.

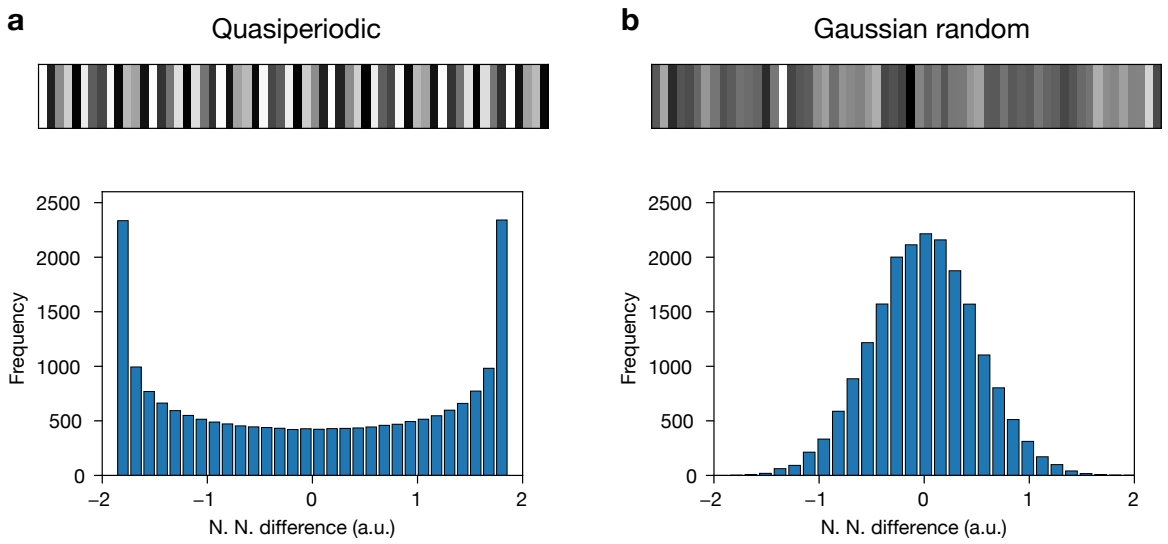

Figure 6.2: Comparison of 1D nearest-neighbour detunings for a quasiperiodic potential and a normal distribution. a Quasiperiodic potential given by the incommensurate periodic potential $V(i) = \cos(2\pi\beta i)$ where $\beta = (\sqrt{5}-1)/2 \approx 0.618$ is the inverse golden ratio and i are integer values. **b** Random values given by a normal (Gaussian) distribution with $\mu = 0$ and $\sigma = 0.35$. Both histograms have been obtained by sampling 20000 points.

True random disorder

A specific feature that is characteristic of our experimental implementation is that the projected disorder potentials are "true random". This means that, in contrast to quasiperiodic models, the potential in each site δ_i is almost independent (uncorrelated) of the values in other lattice sites (only limited by the finite resolution in our imaging system). We would like to emphasize that the experimental results obtained with these different distributions can be significantly different. Aside from differences related only to the histogram distribution of the single-site potentials, a main difference can be found in the nearest-neighbour detuning. In Fig. 6.2 we compare the nearest-neighbour potential differences for a 1D quasiperiodic and 1D Gaussian random distribution. We observe that, while in the quasiperiodic case the distribution is peaked at the maximum possible detunings, in the Gaussian case the distribution is centered around the vanishing difference.

In practice, this means that in general one cannot directly compare the dependence on their disorder strengths, since Δ_{qp} typically denotes the amplitude of the modulating sinusoid, while Δ_{Gau} the width of the Gaussian distribution. In fact, the emerging physical phenomenology can be fundamentally different [149], and a study of these two kinds of disorder, in the same experimental setup, would be particularly interesting.

As a last remark, note that similar results are also reached when considering uniform (instead of Gaussian) distributions, and that similar comparisons, with modified conclusion, can be obtained when considering quasiperiodic models in higher dimensions [48].

6.3 A first glimpse at MBL: domain-wall dynamics

A first experiment concerning MBL realized in our setup was done by preparing an initial state with all particles prepared on one side of our trap, i.e. a density domain wall. The imbalance $\mathcal{I}$ was computed by taking

$$\mathcal{I} = \frac{N_L - N_R}{N_L + N_R}, \tag{6.6}$$

where $N_{L(R)}$ is the number of particles in the left(right) side of the harmonic trap for the selected region of interest. In this section we will discuss some of the main results of the publication *Exploring the many-body localization transition in two dimensions* [47].

6.3.1 Imbalance dynamics

Following the experimental implementation described in the previous section, the system was allowed to evolve for few hundreds of tunneling times and its imbalance measured. In Fig. 6.3a one can already qualitatively appreciate the behavior expected for a thermalizing and a localized state. In the absence of disorder, the density gets homogeneously distributed in the harmonic trap after more than a 100 τ, while for a disorder strength of $\Delta = 13\,J$, clearly most of the particles remain in the left side of the trap even after 249 τ.

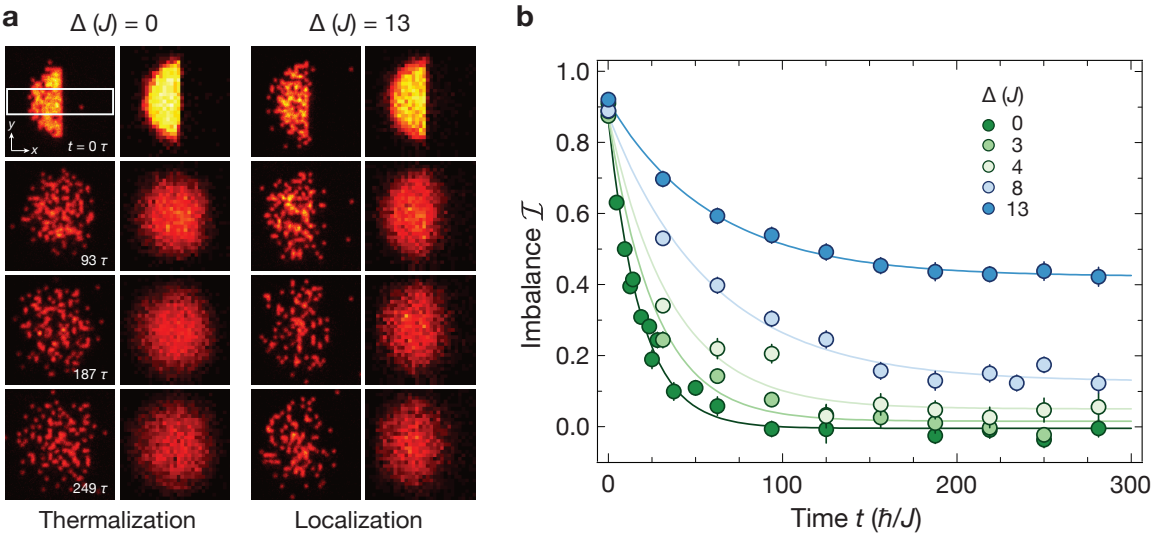

Figure 6.3: Dynamics of a domain wall for different disorder strengths. a Evolution of the density in the system, illustrating thermalization and localization. The left two columns show the evolution in the absence of disorder, with individual snapshots in the left and the mean occupations in the right (black-red-yellow colormap). For the right two columns, the disorder strength is $\Delta = 13\,J$ and most particles remain on the left side of the trap even after long times. **b** Plot of the imbalance $\mathcal{I}$ as a function of time for five different disorder strengths. The solid lines are fits of an exponential with an offset.

The imbalance dynamics are plotted in Fig. 6.3b for five different disorder strengths. For $\Delta < 4\,J$, the imbalance ends up vanishing for long times, an indication of the delocalization of the particles over the trap. For the datasets at $\Delta = 8\,J$ and $13\,J$, we see a remaining imbalance (as high as $\mathcal{I} \approx 0.5$) even after the longest measured times, which evidences a localization of the particles, and hence a breakdown of ergodicity. The dynamics of the imbalance is compatible with an exponential decay with a long-time offset , that is $\mathcal{I}(t) = (\mathcal{I}_0 - \mathcal{I}_\infty)\, e^{-t/t_1} + \mathcal{I}_\infty$.

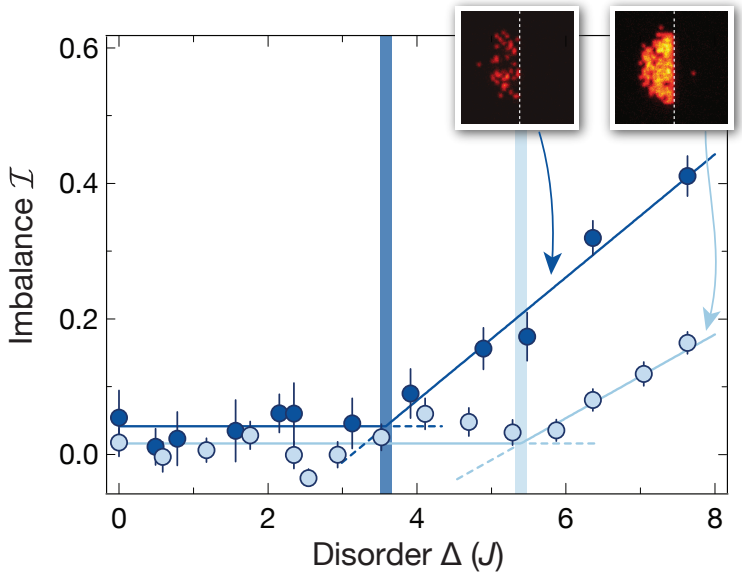

Figure 6.4: Long-time imbalance vs disorder strength for two different densities. We plot the imbalance $\mathcal{I}$ at $t = 187\tau$ as a function of the disorder strength Δ for initial states close to unit filling (light blue) and states with one quarter of that density (dark blue). The two solid lines indicate a double linear fit, and the vertical faded lines indicate the fitted location of the transition.

6.3.2 Density dependence

A natural question to ask is what is the effect of interactions in the dynamics of the system, to therefore distinguish this phenomenon from Anderson localization. While in our system it is not possible to tune the interaction strength U via a Feshbach resonance, a direct way of exploring this direction is to reduce the density in the system. This can be done by pushing out a selective fraction of the particles after the preparation of the MI in the atomic limit, which can be done by a MW pulse followed by an optical push.

In Fig. 6.4 we show the imbalance after a long time of $t = 187\tau$ as a function of the disorder strength for two different densities. One is essentially at unit-filling, that is at the same conditions as in the dynamics, and the other one with $\sim 25\%$ of the initial density. One can appreciate that, while in the unit-filling case the imbalance remains close to 0 until $\Delta \approx 6J$, in the low-density dataset the imbalance goes above zero already for $\Delta \approx 3J$. We can perform a piecewise double-linear fit with the function $\mathcal{I}(\Delta) = \mathcal{I}_1 + \mathcal{C}_2 \cdot \max(0, \Delta - \Delta_c)$, which allows us to extract the critical disorder strengths $\Delta_c = 5.5(4)\, J$ and $\Delta_c = 3.6(2)\, J$. This shows that the localization

transition is shifted to stronger disorder strengths Δ as one increases the effect of interactions. This is consistent with interactions reducing localization, and indicates the many-body character of our system.

6.4 Probing localization at different lengthscales

An interesting direction to explore concerns the effects on localization by preparing diverse initial states. For example, one can prepare states with different energy densities, which can be used to study the existence of many-body mobility edges [150, 151]. On the other hand, the transport properties and the relaxation timescales can highly depend on the specific density configuration that one explores [148, 152]. In particular, in our domain-wall experiment we effectively probe the transport over a lengthscale on the order of the size of the system ($\sim$ 12 sites). This is quite different from experiments probing charge density waves, which effectively probe localization on the order of one lattice site. In this section, we make use of our capabilities to prepare initial density patterns with density modulations on very different lengthscales.

6.4.1 Experimental results

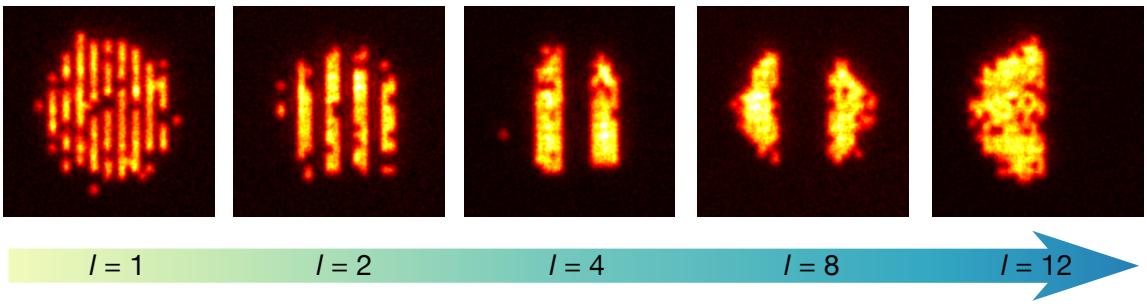

Figure 6.5: Snapshots of different stripe patterns. Individual fluorescence pictures of the initial state for the five different stripe patterns. The stripe widths go through $l = 1, 2, 4, 8, 12$ (from left to right).

Initial stripe patterns

The prepared initial density patterns are made of occupied stripes (with one atom per site) of tunable width l (see Fig. 6.5). One can also consider them square charge density waves with different periods. The $l = 1$ case (a Néel-like state) is precisely the initial state prepared in superlattice MBL experiments [44, 48], which refer to as "charge density wave". The largest width, of $l = 12$, is roughly half of the system size,

and hence is equivalent to the domain-wall state.

To avoid significant contributions from the harmonic trap confinement, we prepare the stripes symmetrically with respect to the center of the trap. This means that the total atom number and the energy density is the same for all states with different density modulation. In principle, this implies that in the different experiments one deals with the same MBL relaxation physics but probes different lengthscales.

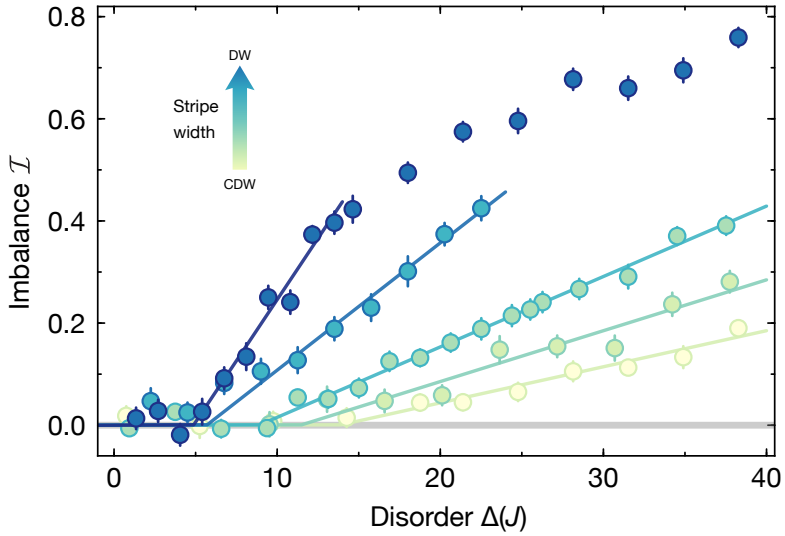

Figure 6.6: Long-time imbalance as a function of the disorder strength for different density stripes. Plot of the generalized imbalance measured after $t = 625\,\tau$ as a function of disorder strength. The stripe widths correspond to l =1, 2, 4, 8 and 12 sites (yellow-green-blue colormap). The solid curves are the fit of the piecewise bilinear function $\mathcal{I}(\Delta) = \mathcal{C}_2 \cdot \max(0, \Delta - \Delta_c)$. We can see how the dependence of the imbalance is steeper for the longer lengthscales.

Localization and disorder dependence

The quench and the dynamics follow the same conditions as described in Sec. 6.2.2. To study the degree of localization in these states, we will use the generalized version of imbalance defined in Eq. 6.4. In the absence of disorder, the imbalance $\mathcal{I}_l$ of all these different states will relax to a vanishing value. This nicely reflects the process of quantum thermalization, in the sense that, regardless of the initial density distribution, the system relaxes to the "same" state.

Now we focus on the localization in the presence of disorder. To do so, we measure the imbalance for different disorder strengths after an evolution of $t = 625\,\tau$, to en-

sure that the we are beyond the initial relaxation dynamics. The results are shown in Fig. 6.6 for stripe widths of $l = 1, 2, 4, 8$ and 12 sites. Qualitatively, all datasets behave similarly to the ones in Fig. 6.4. They show a vanishing imbalance for small disorder strengths Δ which becomes finite above a certain threshold of disorder. Above that threshold, the imbalance monotonically grows (roughly linearly) as the disorder is increased. The slope of the dependence, however, is dramatically different for the different stripe widths. While the $l = 12$ case (domain wall) shows a steep growth (similar as in Fig. 6.4) and reaches values of the imbalance close to $\mathcal{I} = 0.8$, for the $l = 1$ case the dependence is weaker, and even for the strongest disorders one observes $\mathcal{I} < 0.2$.

To better characterize the dependence, we also perform a double linear fit $\mathcal{I}(\Delta) = \mathcal{C}_2 \cdot \max(0, \Delta - \Delta_c)$ for each dataset. From the solid lines in Fig. 6.6 one can directly see how the slope increases for wider stripes. This dependence can be intuitively understood in terms of the localization length of the particles. The width-dependent imbalance $\mathcal{I}_l$ can be seen as a probe of localization on a lengthscale l, and therefore $\mathcal{I}_{l=1}$, for example, will only grow to a significant value once the localization length is below few lattice sites.

From these results, one can quantify the localization length as a function of the disorder strength. To do so, we define an arbitrary finite threshold value of the imbalance, here $\mathcal{I}_l = 0.2$, for all stripe widths. If the imbalance goes above this threshold, we consider the atoms to be localized on a lengthscale l. This allows us to extract a threshold disorder strength $\Delta_t(l)$ for each stripe width l. In Fig. 6.7 we show this dependence by plotting the stripe width l as a function of the threshold disorder strength. This plot is similar to that in other works in 1D, where the dependence of the localization length on the disorder was characterized for Anderson localization [109] and MBL [45].

In the same figure, we also show the relation between the stripe width l and the "critical" value Δ_c. The dependence looks very similar as Δ_t, which seems to suggest that the phase transition gets shifted to higher disorder strengths for shorter stripe widths. However, this effect could be just explained by the weaker sensitivity of $\mathcal{I}_l$ for localization lengths way above l. In this sense, experimentally measured values of Δ_c are likely to be an underestimated in finite-sized systems.

6.4.2 Non-interacting simulation

Last, to provide some more intuition into the dependence on the stripe width, we perform simulations for a non-interacting disordered tight-binding model. We simulate single-particle dynamics in a disordered lattice of a particle initially prepared in one lattice site. We then compute the imbalance from the single-particle wavefunction, and do the same for different initial positions in the lattice. The total imbalance, for a

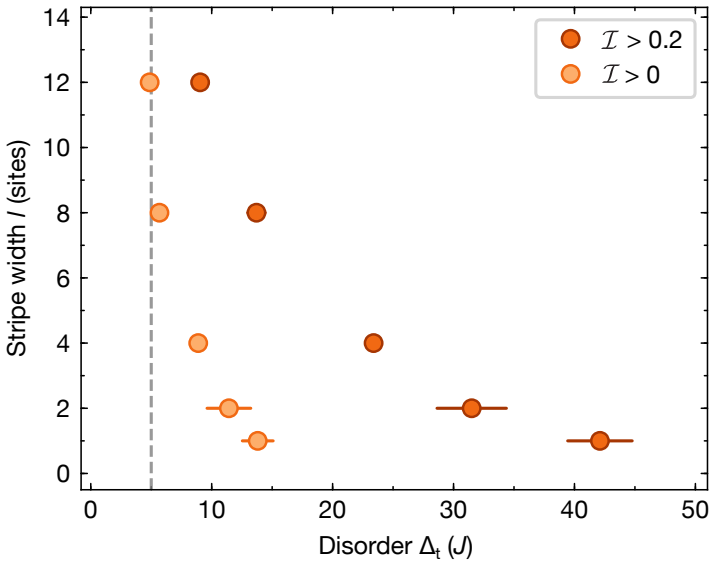

Figure 6.7: Stripe width vs localization threshold. We plot the width of the density-striped state vs its corresponding threshold Δ_t for a localization with $\mathcal{I} = 0.2$ (dark orange). We also do the same plot for the critical value Δ_c, which can be seen as a threshold for $\mathcal{I} > 0$. The dashed vertical gray line indicates the position of $\Delta_c(l = 12)$, which is the longest measured width.

specific density pattern, can then be calculated by averaging only the imbalance of the particles in a subset A. Finally, we also average over the total imbalance several disorder patterns. This approach has the advantage to be only limited by the dimension of the single-particle Hilbert space, allowing to simulate large 2D systems easily.

The results are shown in Fig. 6.8, where we have also considered the harmonic confinement. For Anderson localization in 2D one expects, in contrast to MBL, localization to start for an arbitrarily small disorder strength. While the imbalance for $l = 12$ shows a quite sharp increase (though partially affected by finite-size effects), $\mathcal{I}_{l=1}$ only shows a clear onset as the disorder goes way beyond $\Delta = 5\,J$. This is consistent with the previous line of argument concerning the sensitivity of $\mathcal{I}_l$ for small values of l.

6.5 Summary and outlook

To summarize, in this chapter we introduced our scheme to study out-of-equilibrium dynamics in a disordered two-dimensional BH system. A spatially modulated product state is initially prepared and, by means of a quench of the lattice depth and of a

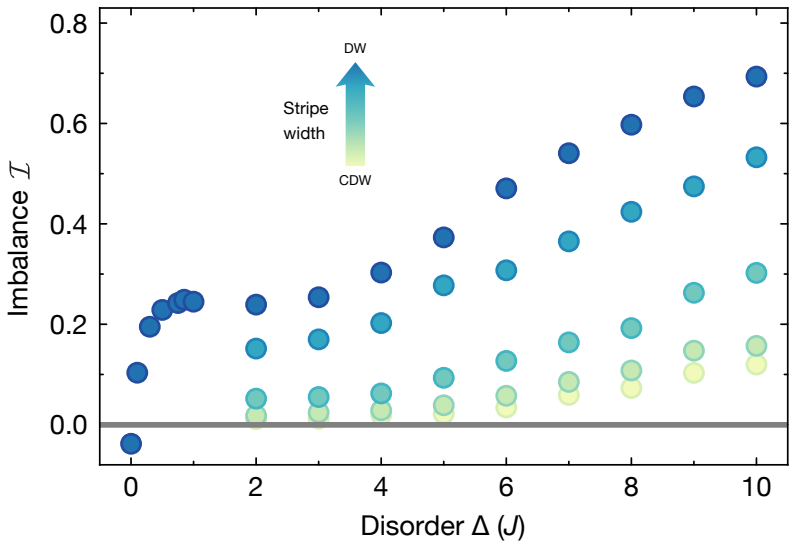

Figure 6.8: Steady-state imbalance vs disorder strength for a non-interacting simulation. Plot of the imbalance for the five stripe patterns as a function of the disorder strength. The stripe widths correspond to l =1, 2, 4, 8 and 12 sites (yellow-green-blue colormap). The results have been obtained from a single-particle simulation in a lattice with the same parameters as in the experiment. The results show few features qualitatively similar to those in the experimental results for an interacting system, as the distinct dependence for increasing stripe width. For low disorder strengths, finite-size effects arise related to the harmonic confinement, especially for the $l = 12$ case.

disordered potential, is brought far from equilibrium. By measuring the density imbalance and tuning the disorder strength, we have observed an onset of localization, which is a key signature of the ergodic-to-MBL phase transition. By preparing different initial states with tunable density modulation, we have gained insight into the length over which the particles are localized in our system. These results are among the very few experimental studies of MBL in higher dimensions, and only recently have some numerical results shown evidence of 2D localization [153–155].

In the future, there are several exciting directions to be explored. A major one is to study larger system sizes, which would also make it possible to prepare large homogeneous one-dimensional systems, which have not been explored in this thesis. Another one is to explore more exotic observables, such as density correlators [45] or probes of entanglement [88]. Last, it would be interesting to explore additional models displaying MBL, such as with hard-core bosons or the Heisenberg model, which can be studied in our setup with minor changes in our implementation.

Chapter 7

Coupling a quantum bath to a MBL system

A major open question in the field of MBL concerns the robustness of localization when coupled to finite thermal regions. In this chapter we consider the situation of coupling a disorder-free system to a localized one to observe how it affects its out-of-equilibrium dynamics. We will first motivate simple models that provide insight into these delocalization questions and comment on some theoretical results. We will then describe the two-species system studied in the experiments of this chapter, consisting of a *clean* and a *dirty* component. Next we will track the imbalance dynamics of the dirty component under a tunable presence of the clean one, and discuss its interpretation. We will continue by tracking the dynamics of the clean component too. Finally we will discuss possible extensions of this work and similar experiments. The contents of this chapter are based on the article *Many-body delocalization in the presence of a quantum bath* [87].

7.1 Motivation

When discussing the phenomenon of MBL and its properties, we commonly consider it as a discrete opposition to ergodicity. Nonetheless, in many relevant situations one finds states with partially thermalizing features, even in the MBL side. For example, as one approaches the MBL phase transition rare locally thermal regions proliferate through the system [156]. The processes through which these locally thermalized regions couple to the rest of the system are at the heart of recent discussions concerning the stability of MBL in higher dimensions [157]. These scenarios are also related to the existence of many-body mobility edges, where the ETH might be obeyed in some parts of the spectrum but be violated in others [158–161].

Some of these fundamental questions could be addressed by considering the coupling between two different systems, one in an ergodic state and the other one fully localized. While this is the kind of problem already treated when coupling a macroscopic external heat bath to a MBL system [147, 162–165], it would be particularly

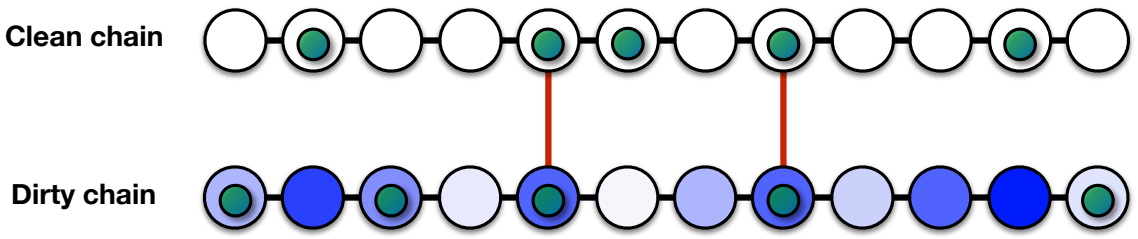

Figure 7.1: Schematic illustration of a hybrid clean-dirty system. The system is made out of two coupled chains, each one of them with interacting and tunneling particles. The upper chain is purely periodic, while the lower one displays quenched disorder.

interesting to consider cases where the thermal bath is only made up of few degrees of freedom. This would allow to answer questions such as *How small can a bath be to delocalize MBL?*, or *Can the MBL system affect the dynamics in thermal one?*

To study such phenomena in a well-controlled setting, one can consider a ladder model consisting of a *dirty* chain (with a quenched-disorder potential) coupled to a *clean* chain [166–168]. In this model, particles could hop and interact within each respective chain, and an interchain coupling would emerge for particles in the same rung (see Fig. 7.1). In the uncoupled case, the particles in the clean chain will quantum thermalize, while on the dirty chain localization might take place for strong enough disorders. By introducing interactions between the chains, the clean particles can now be regarded as a quantum bath for the dirty chain.

In this chapter, we will describe an experiment that makes such a realization of a MBL system coupled to a quantum bath. By employing a state-dependent disorder, we study the dynamics of a two-dimensional mixture of atoms in a dirty and a clean state. While the atoms of the dirty component show strong signatures of localization in the absence of a bath, by introducing a large enough number of atoms in the clean component, the signs of localization eventually vanish. For intermediate sizes of the bath, the situation is less clear and a finite imbalance remains even beyond 1000 tunneling times.

7.2 Experimental details

The details of the experimental system and the initial preparation of the out-of-equilibrium state are very similar to those described in Ch. 6. Starting with a unit-filling MI, we first prepare a charge-density-wave pattern (stripe width $l = 1$) by se-

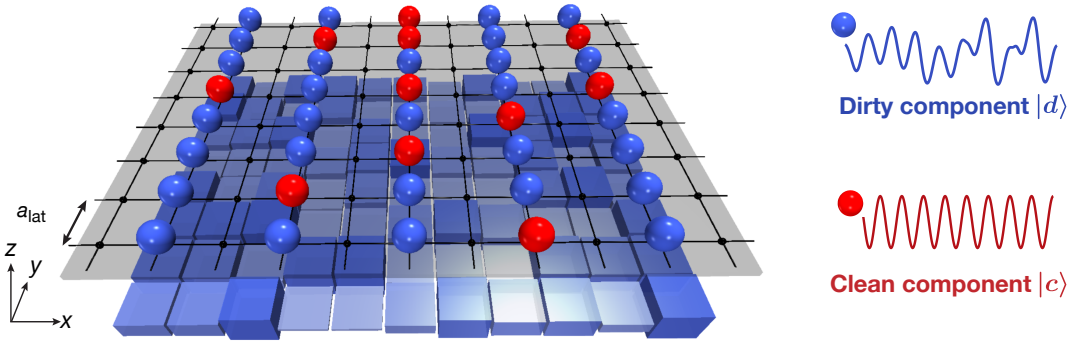

Figure 7.2: Schematic illustration of the experiment. A charge-density-wave pattern of atoms is prepared in a 2D square lattice. The atoms populate two different states (blue atoms in $|d\rangle$, red atoms in $|c\rangle$), and the disorder potential (blue boxes) is only experienced by the atoms in the dirty $|d\rangle$ state.

lectively removing all atoms in the odd columns (see Fig. 7.2). The total atom number after this procedure is of $N = 124(12)$. Next, we use a resonant MW pulse to prepare the atoms in a mixture of the hyperfine $|F = 2, m_F = -2\rangle$ and $|F = 1, m_F = -1\rangle$ states. By modifying the length of the pulse we can tune the population in each one of those states (see Fig. 7.3a). After preparing this initial state in deep lattices, we then quench the system by ramping up a disordered potential and ramping down the in-plane lattices.

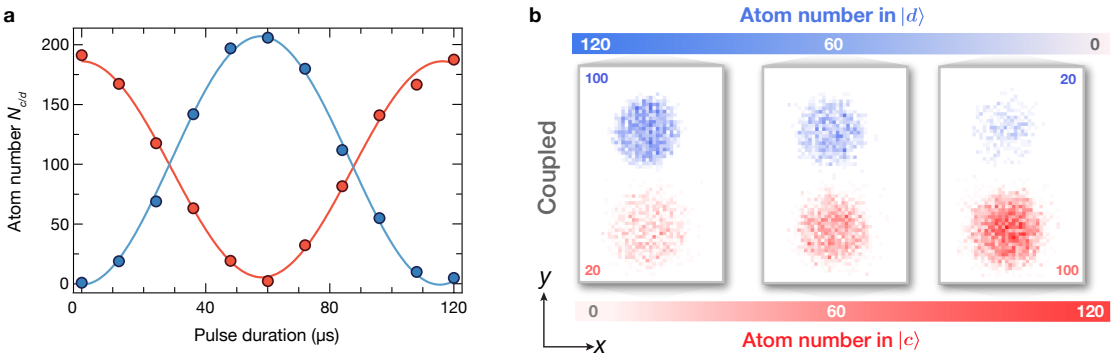

Figure 7.3: Preparation of the state mixture. a Plot of the number of atoms in the $|c\rangle$ and $|d\rangle$ states as a function of the duration of the resonant MW pulse. **b** Pictures of the averaged occupations in states $|c\rangle$ and $|d\rangle$ after an evolution time of 281 τ for three different population ratios.

The important point to note is that by tuning the disorder beam to be in the tune-out wavelength of the $|F = 1, m_F = -1\rangle$ state ($\lambda = 787.55\,\mathrm{nm}$, as discussed in Ch. 3), we have effectively generated a lattice with a state-dependent disorder. This means that while the *dirty* species $|d\rangle = |F = 2, m_F = -2\rangle$ experiences the disorder potential, the *clean* $|c\rangle = |F = 1, m_F = -1\rangle$ is only affected by the purely periodic optical-lattice potential. The scattering lengths are essentially the same both for intra- and inter-species interactions, and thereby the onsite interactions fulfill $U_{dc} \simeq U_{cc} \simeq U_{dd} \equiv U$. Because of this, the system can be well described by the two-species BH Hamiltonian

$$\begin{aligned}\hat{H} = &- J \sum_{\langle i,j\rangle,\sigma} \hat{a}^\dagger_{i,\sigma}\,\hat{a}_{j,\sigma} + \frac{U}{2}\sum_{i,\sigma}\hat{n}_{i,\sigma}(\hat{n}_{i,\sigma}-1) \\ &+ U\sum_{i}\hat{n}_{i,d}\,\hat{n}_{i,c} + \sum_{i,\sigma} V_i\,\hat{n}_{i,\sigma} + \sum_i \delta_i\,\hat{n}_{i,d},\end{aligned} \tag{7.1}$$

with $\hat{a}_{i,\sigma}$, $\hat{a}^\dagger_{i,\sigma}$ and $\hat{n}_{i,\sigma}$ denoting the annihilation, creation and number operators for a particle in state $\sigma \in \{c, d\}$ at a site $\boldsymbol{i}$ of the 2D lattice [$\boldsymbol{i} = (i_x, i_y)$]. The first term indicates the tunneling between nearest-neighbour sites $\langle \boldsymbol{i}, \boldsymbol{j}\rangle$ with a state-independent amplitude J, followed by the intra- and inter-species interaction terms. Next, the harmonic trap potential is given by V_i, and the last term is the state-dependent on-site disorder, affecting only the $|d\rangle$ state. The single-site potential δ_i is Gaussian distributed with a full-width-at-half-maximum Δ. For all experiments in this chapter, the Bose-Hubbard parameters are fixed to $J/\hbar = 2\pi \times 24.8\,\mathrm{Hz}$, $U = 24.4\,J$ and the disorder distribution to a strength $\Delta = 28\,J$.

Let us begin by considering the outcome of preparing the system purely in one of the two hyperfine states. At these parameters of tunneling and interactions, a system in the $|d\rangle$ state will display a very slow decrease in the visibility of the initial pattern (see Fig. 7.4a) until it reaches a long-lived steady state of finite imbalance, as we saw in the dynamics of Ch. 6, which is a signature of many-body localization. On the other hand, a purely clean system will fade into a state with homogeneous density after very few tunneling times (see Fig. 7.4b). This qualitatively shows that we indeed have realized a setup where we can prepare a hybrid system with localizing or thermalizing particles.

7.3 Dynamics of the dirty component

In this section we will focus on the effects induced by the coupling of a quantum bath into a MBL system and its dynamics. Working always with the same total number of atoms, we transfer a preset number N_c of atoms into the clean state, which constitute the thermalizing bath with few degrees of freedom. After the dynamics, we remove all

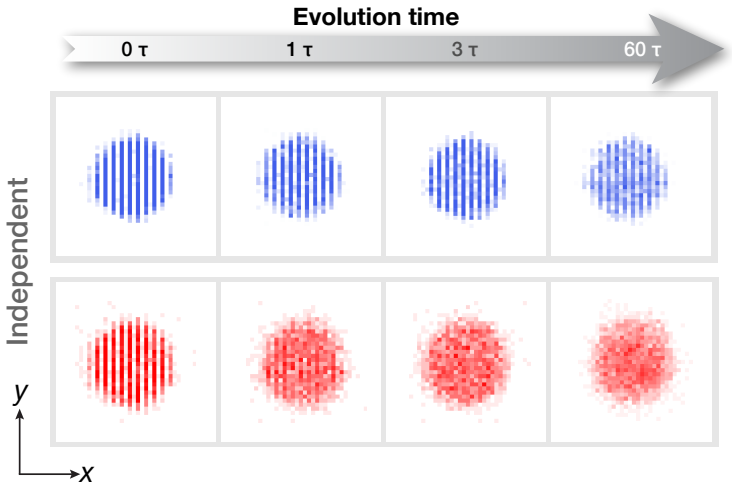

Figure 7.4: Evolution of the site-resolved density for a purely clean or dirty system. Plot of the mean measured densities in the lattice for the independent dirty (blue) and clean (red) systems. The dirty atoms show a pattern remaining even after several tens of tunneling times, while the density pattern in the clean atoms disappears in few tunneling times.

$|c\rangle$ atoms by performing a MW transfer followed by a resonant D_2 light pulse before imaging the occupation of the remaining $|d\rangle$ atoms.

7.3.1 Dynamics in the absence of a bath

We begin by preparing a state with no particles in the clean component, i.e. in the absence of coupling to a quantum bath. In Fig. 7.5 we plot the dynamics of the imbalance of the dirty component $\mathcal{I}_d$. Overall, we observe a decrease of the initial imbalance from $\mathcal{I}_d = 0.91(1)$ to a long-time steady value of $\mathcal{I}_d \approx 0.13$. This resilience of a finite imbalance after long times is a signature of MBL.

The observed relaxation of the imbalance takes place on two different timescales, and one phenomenologically describe the data by a sum of two exponentials plus a stationary offset, $\mathcal{I}_d(t) = \mathcal{I}_1\, e^{-t/t_1} + \mathcal{I}_2\, e^{-t/t_2} + \mathcal{I}_\infty$. A first timescale is identified with a decay time of $t_1 = 0.6(1)\,\tau$, during which the atoms mainly expand freely into the empty sites. Next, a much smaller dynamics takes place, with a decay time of $t_2 = 103(6)\,\tau$, in which interactions are actually relevant. The changes in this last decay once the clean particles are introduced will be the focus of following analysis in this experiment. Note that the separation of these two timescales was not identified in the domain-wall dynamics shown in the previous chapter (see Fig. 6.3). This is caused by the much faster initial decay in the CDW case, due to its short spatial modulation.

Additionally to the imbalance, we also resolve the generation of doubly occupied sites (which we refer to as doublons) during the relaxation dynamics (see inset of Fig. 7.5). We do so by comparing the total measured atom number (see Sec. 3.2.3) with the parity-projected one (more details can be found in the Supplementary Information of [87]). Beginning from a doublon-free initial state, we observe a very rapid formation after the quench, followed by a saturation of the doublon fraction. Bear in mind that this effect requires both the presence of disorder and interactions, given that for the parameters of the experiment (strong interactions), a disorder-free lattice would not display such a dynamical formation of doublons. The behavior of both the imbalance and the doublon dynamics is qualitatively reproduced by exact-diagonalization simulations shown in App. B.

Beyond the characterized timescales, we expect the finite isolation of the experiment, which is unavoidable in any experiment, to become significant for longer times. In this experiment, it led to an atom loss of 15% of the total atom number after $600\,\tau$. We expect these losses to be mainly due to excitation to higher bands during the dynamics. While it is unclear what is the effect of this coupling on localization, our experiments do not seem to show a strong delocalization for long times. Any subsequent relaxation of the imbalance must be well separated from the initial decays, and based on a bootstrap analysis of an exponential fit for the data beyond $500\,\tau$, we were able to bound any further relaxation to be $t_3 > 2300\,\tau$ with 92% confidence.

7.3.2 Dynamics in the presence of a bath

In Fig. 7.6 we plot the imbalance of the dirty component $\mathcal{I}_d$ for three different bath sizes ($N_c = 20, 40, 90$), together with the purely dirty case ($N_c = 0$) as reference. This last dataset is the same one as in Fig. 7.5. Qualitatively, we see that as the size of the bath is increased the overall imbalance gets reduced. While the imbalance does end up vanishing for the two biggest bath sizes ($N_c = 40$ and $N_c = 90$), a very small finite imbalance remains for the smallest bath size ($N_c = 20$). We should stress that, while preparing a fraction of clean atoms implies reducing the density of the dirty component, this alone would actually lead to a higher long-time imbalance, as we discussed in Ch. 6 and in [47].

To get a better insight, especially into the delocalizing dynamics, we plot those same datasets in a log-lin scale in Fig. 7.7, which makes it easier to identify solely exponential behavior. For the biggest bath size, the $N_c = 90$ case, the imbalance relaxes to zero in less than $300\,\tau$, implying that the atoms have been delocalized over few lattice sites. From fitting a single exponential, that is $\mathcal{I}(t) = \mathcal{I}_1\, e^{-t/t_1}$, we obtain a time constant of $140(30)\,\tau$ (red dashed line). For the $N_c = 40$ case we observe a similar delocalization, whose exponential fit gives a slower time constant of $200(20)\,\tau$. These results evidence that the atoms in the clean component act as an effective bath, desta-

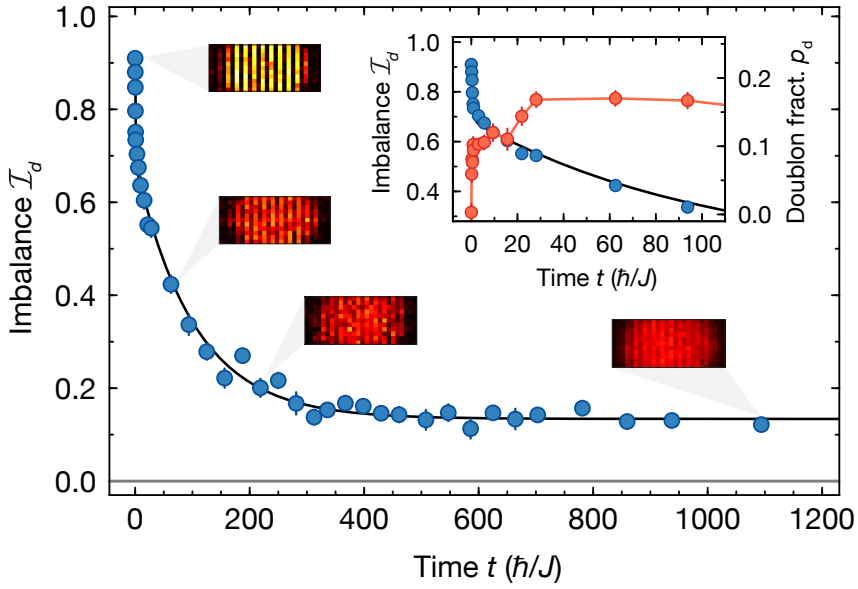

Figure 7.5: Dynamics of solely the dirty component. We plot the measured long-time evolution of the dirty-component imbalance $\mathcal{I}_d$. We observe a monotonic decrease of the imbalance in two distinct timescales. An initial quick decay, in which interactions play not much of a role, is followed by a much slower one related to relaxation of doubly occupied sites. After roughly $300\,\tau$ the system reaches a steady state with $\mathcal{I}_d \approx 0.13$. Inset rectangles show the mean density in the center of the trap (black-red-yellow colormap) for four different times, $t = 0\,\tau$, $63\,\tau$, $219\,\tau$ and $1094\,\tau$ which illustrate the reduction in imbalance. In the inset plot (top-right corner) we plot the dynamics of $\mathcal{I}_d$ (blue markers) and the fraction of doubly occupied sites p_d (red markers) for very short times. Notably, the rate of doublon generation sharply changes between the two regimes of the imbalance decay. The error bars represent one standard error of the mean (s.e.m).

bilizing the localized dirty component and bringing it towards thermalization. Note that this effect is only caused by intercomponent collisions, with same strength as the intracomponent interactions in the system. This means that no additional energy scale has been introduced by adding the clean component, underlining the non-triviality of the observed localization.

For even smaller sizes of the bath ($N_c = 20$), the overall imbalance reduction can be appreciated, but there is a qualitative difference in its dynamics. There still remains a finite value of the imbalance for the longest measured times (above $1000\,\tau$), and the data is no longer well described with a simple exponential fit. Instead, we introduce

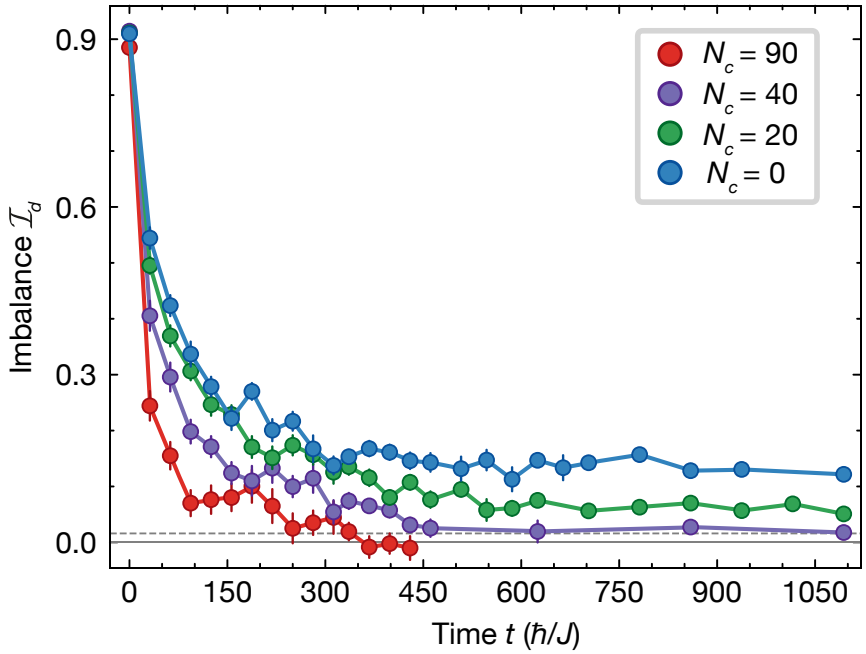

Figure 7.6: Full-range dirty-component dynamics. Dynamics of the imbalance $\mathcal{I}_d$ of the atoms in the dirty state for four different sizes of the bath ($N_c = 0$ in dark blue, $N_c = 20$ in green, $N_c = 40$ in purple and $N_c = 90$ in red). Increasing the population of the clean component leads to delocalization, as indicated by a reduction in the imbalance $\mathcal{I}_d$. The imbalance relaxes completely for the two largest bath sizes, while for the smallest size of the bath ($N_c = 20$), a finite imbalance still remains after long times. The horizontal dashed gray line indicates the typical statistical threshold at which the imbalance is compatible with zero. The error bars indicate one standard error of the mean (s.e.m.).

a steady-state offset, as we did in the fit of the bath-free case, which matches the data much better (solid curves). Additional fits of the other datasets reveal this as the simplest model that can give a good description of all data. Concerning any potential subsequent relaxation, a bootstrap analysis revealed that to be bound by $t_3 > 1100\,\tau$ with a confidence of 92%.

To give a clearer picture of the delocalization in the long-time limit, in Fig. 7.8 we plot the imbalance $\mathcal{I}_d$ as a function of bath size for two different evolution times ($t = 859\,\tau$ and $t = 1094\,\tau$). The imbalance values for both cases are quite similar, and they are also compatible with the offsets obtained from the exponential-plus-constant fits of the data in Fig. 7.7. We observe that a finite imbalance is still present for datasets

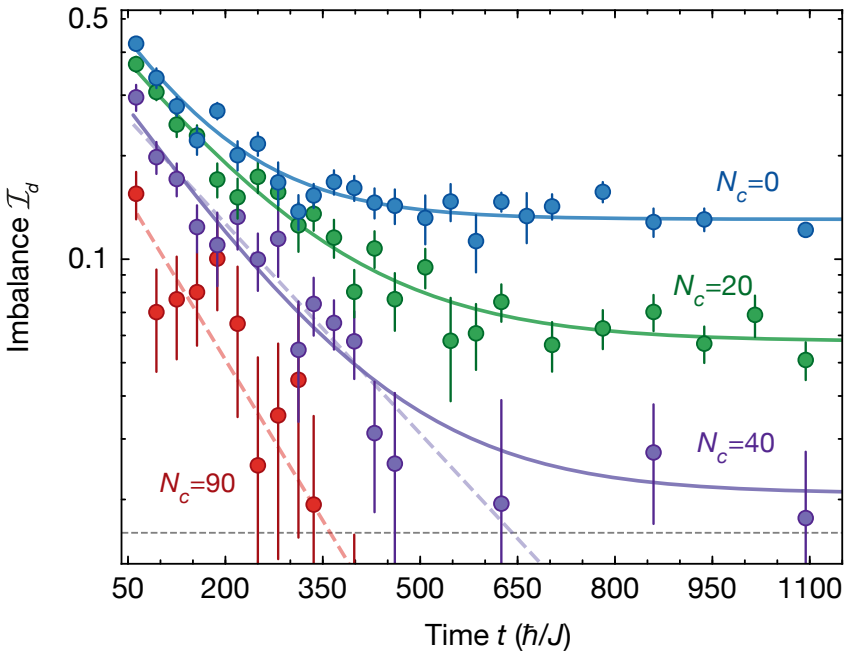

Figure 7.7: Zoomed dirty-component dynamics in log-lin plot. Dynamics of the imbalance $\mathcal{I}_d$ of the atoms in the dirty state for four different sizes of the bath ($N_c = 0$ in dark blue, $N_c = 20$ in green, $N_c = 40$ in purple and $N_c = 90$ in red) in a log-lin plot. The solid curves are fits of an exponential with an offset, while the dashed curves are fits of a single exponential decay. The horizontal dashed gray line indicates the typical statistical threshold at which the imbalance is compatible with zero. The error bars indicate one s.e.m.

with bath sizes $N_c \lesssim 40$.

The phenomenology of the dynamics for small baths could be a consequence of a very slow delocalization of the dirty component, leading to a decay well below all other timescales of the system. Nonetheless, it could also be explained by a complete failure of thermalization. In one dimension, theoretical studies considering systems of interacting clean-dirty components have found persisting localization in some regimes where the clean component has a reduced tunneling [166, 167]. A similar process could be happening in our experiment, explained by a reduction in the coupling of spatially separated points, due to the reduction in the size of the bath component.

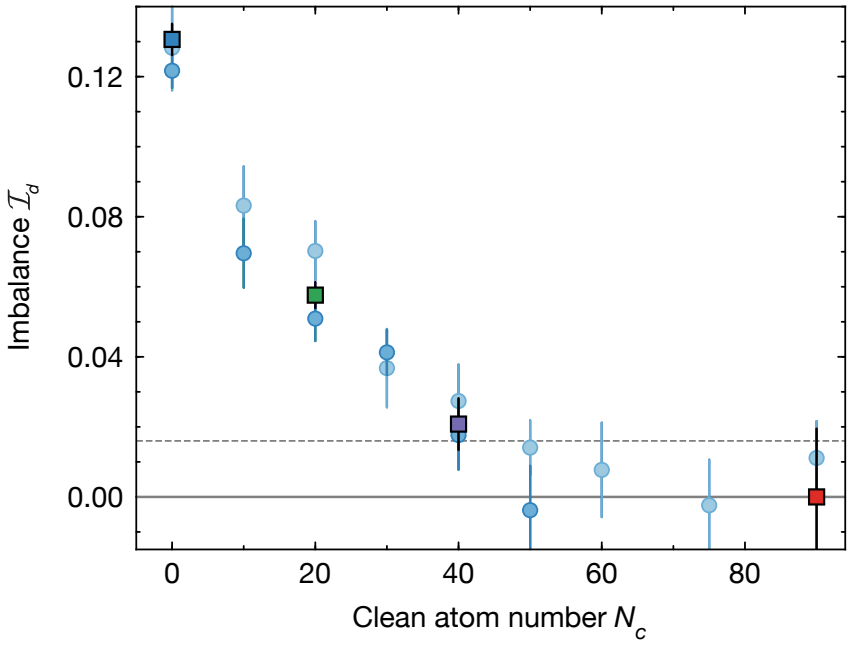

Figure 7.8: Experimental steady-state imbalance as a function of the bath size. Plot of the long-time imbalance $\mathcal{I}_d$ vs the number of atoms in the clean state N_c. The data was measured at $t = 859\,\tau$ (round points in blue) and at $t = 1094\,\tau$ (round points in light blue). The square points correspond to the asymptotic offsets obtained from the four solid line fits in Fig. 7.7. The horizontal dashed gray line indicates the typical statistical threshold at which the imbalance is compatible with zero. The error bars indicate one s.e.m.

7.4 Dynamics of the clean component

After focusing on tracking the dynamics of the dirty component, in this section we look at the dynamics of the imbalance of the clean-component atoms $\mathcal{I}_c$. By doing so, we probe the back-action of the dirty component on the quantum bath and its dynamics. We proceed by removing all the atoms in state $|d\rangle$ before imaging. We do so by first applying a microwave π-pulse that swaps the populations of the two hyperfine states and then applying a resonant light pulse in the D_2 line. The results show that, independently of how small the size of the bath is, $\mathcal{I}_c$ quickly relaxes to a vanishing value, on a timescale of few tunneling times. This means that any potential interaction-induced localization of the atoms in the bath by the dirty component has to be given by a localization length spanning at least few lattice sites, and therefore beyond what our short-distance imbalance probe can detect. Since for the smallest bath

($N_c = 20$) the remaining imbalance of the dirty component, $\mathcal{I}_d = 0.07(2)$, is already very small, it should only act as a pretty weak source of disorder.

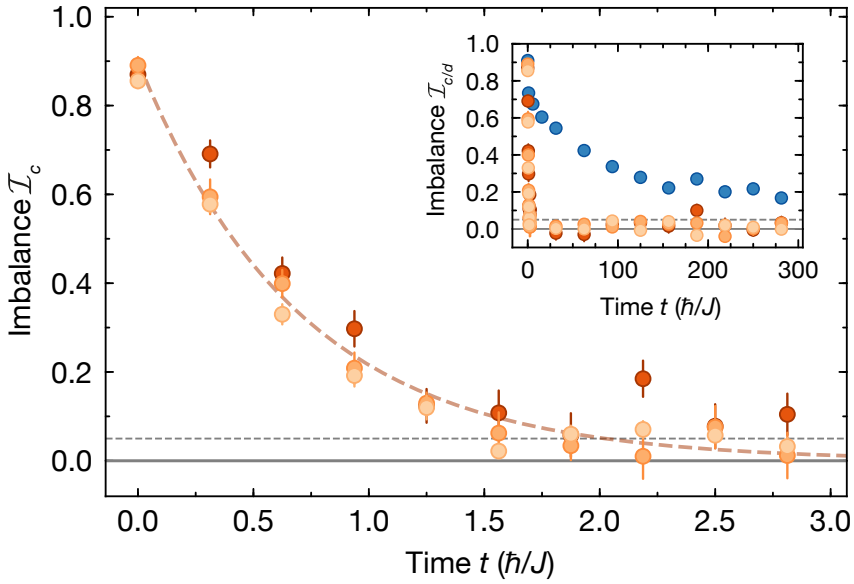

Figure 7.9: Clean-component dynamics. Evolution of the imbalance of the clean component $\mathcal{I}_c$ for three different number of atoms in the clean component ($N_c = 120$ in light orange, $N_c = 60$ in orange and $N_c = 20$ in dark orange). The dashed-lined curve is an exponential fit of the decay, with a time constant of $t_1 \approx 0.7\,\tau$. The outcome is essentially the same for all bath sizes, i.e. the imbalance vanishing in few tunneling times. In the inset we plot the long-time imbalance for the clean component $\mathcal{I}_c$ together with the dirty-component imbalance $\mathcal{I}_d$ for the purely disordered case ($N_c = 0$). This underlines the dramatic difference in the relaxation time scales. The horizontal dashed gray line indicates the typical statistical threshold at which the imbalance is compatible with zero. The error bars indicate one s.e.m.

7.5 Summary and outlook

The experiments described in this chapter have realized for the first time the coupling between a MBL system and a quantum bath of controllable size. Overall, the introduction of the small bath drives the system towards delocalization, which for a sufficiently large sizes of the bath seems to totally thermalize. In the less trivial regime of a very small bath, memory of the initial state of the system remains even after long times.

In the future, it would be interesting to explore different regimes of interaction and disorder. In particular to explore the question of proximity-induced localization [166, 167], which can be realized based on the disorder originating from interatomic interactions [169, 170]. Additionally, the preparation of systems with local absence of disorder could be used to directly address the question on the stability of MBL when coupled to thermal inclusions, given its relevance for systems in higher dimensions [156, 157]. Initial experiments in this direction have already been explored in our experiment, though seem to indicate that the delocalization processes could be beyond the extent of our experimental

Part III

Floquet prethermalization

Chapter 8

Dynamics of Floquet quantum systems

The study of periodically driven (*Floquet*) systems [171] has had a remarkable boost over the last few years, both theoretically and experimentally. This development has greatly benefited the field of ultracold atoms, where closed driven systems can be naturally implemented. In this chapter we start by motivating and giving some examples of applications of periodic driving in different platforms. We then introduce the main properties of Floquet quantum systems and describe their stroboscopic evolution in terms of the Floquet Hamiltonian. We also show how the Magnus expansion provides an expression for the effective Hamiltonian of the system. Next, we consider the heating dynamics in interacting Floquet systems, a major bottleneck for Floquet engineering, and present ways to avoid it. Last, we discuss which specific aspects must be taken into account when considering a system of ultracold atoms in a driven optical lattice.

8.1 Motivation

The scenario of a physical system under periodic modulation is a common one in physics. A broad range of theoretical and experimental studies have considered systems under electromagnetic modulation or mechanical kicks. An example in classical physics is the paradigmatic Kapitza pendulum [172], which shows how an unexpected configuration of the system can be stabilized through a periodic drive. Similarly, in the quantum side we obtain the phenomenon of dynamical localization [173], where a particle in a lattice can get spatially localized by simply introducing an AC field. These two examples reveal the kind of new opportunities that can be enabled by the periodic driving of a system. Recently, a revival of the field of Floquet systems has emerged from the study of out-of-equilibrium dynamics in quantum systems [49, 174–177].

In the field of ultracold atoms, the periodic driving of certain experimental parameters, such as the depth of the dipole trap or the strength of a magnetic field,

has become a common tool. This has led to many examples of Floquet implementations [174], such as the experimental demonstration of dynamical localization [178–180]. A very successful application has been the creation of artificial magnetic fields [181] , which has led to the implementation of the Hofstadter [182] and the Haldane model [183]. Another quite different example is the study of (classical) frustrated spin models [184].

In other systems aside from quantum gases, Floquet engineering has also become a common part of their toolbox. For example topological Floquet insulators, where systems with static topologically trivial phases are electromagnetically driven to engineer new exotic band structures [185]. This method has been implemented in semiconductor quantum wells as well as in graphene [186, 187].

Most of these implementations of periodic drives allow to engineer models or phases of matter that, while possible, can be hard to realize in static systems. However, a completely new direction is the study of quantum Floquet matter with no analog in static phases of matter. A clear example of such a phase of matter is the discrete time crystal [188–197], which extends spontaneous symmetry breaking to the time domain. Another recently discovered example is the anomalous Floquet insulator [198–200].

It is important to note that in these new exotic phases of matter, the high number of involved degrees of freedom requires to consider the onset of heating in driven systems [49], as we will discuss later in this chapter.

8.2 Floquet quantum systems

8.2.1 Time evolution

The time evolution of a quantum state under an arbitrary time-dependent Hamiltonian $\hat{H}(t)$ is given by the Schrödinger equation

$$i\hbar\frac{d}{dt}|\psi(t)\rangle = \hat{H}(t)|\psi(t)\rangle. \tag{8.1}$$

Assuming the case of a static Hamiltonian $\hat{H}_0$, this directly leads to the well-known expression for the unitary evolution

$$|\psi(t)\rangle = \hat{U}(t,t_0)|\psi(t_0)\rangle = \exp\left(-\frac{i}{\hbar}(t-t_0)\hat{H}_0\right)|\psi(t_0)\rangle. \tag{8.2}$$

We now consider instead the Hamiltonian of a periodically driven system, i.e. $\hat{H}(t) = \hat{H}(t+T)$, where T is the period of one Floquet cycle. The time evolution over one

single period is given by the unitary evolution operator

$$\hat{U}(t_0+T,t_0) = \mathcal{T}\exp\left(-\frac{i}{\hbar}\int_{t_0}^{t_0+T} dt\,\hat{H}(t)\right), \tag{8.3}$$

where $\mathcal{T}$ denotes the time ordering of the operators. Due to the periodicity of the Hamiltonian, we can obtain the time evolution over a certain number of Floquet cycles N_{cyc} by just applying the operator $\hat{U}(t_0+T,t_0)$ a number N_{cyc} of times. Based on this, we can always express the time evolution operator as

$$\hat{U}(t+N_{\text{cyc}}T,t_0) = \hat{U}(t,t_0)\left[\hat{U}(t_0+T,t_0)\right]^{N_{\text{cyc}}}, \tag{8.4}$$

where $t \in [t_0, t_0+T]$. This indicates that the additional knowledge of the evolution operator within a cycle, $\hat{U}(t,t_0)$, suffices to calculate the evolution to an arbitrary time of the system. This evolution within a Floquet cycle is referred to as "micromotion", which is in contrast to the "stroboscopic" evolution, described by Eq. 8.3. In the rest of this chapter, we will leave the discussion of any micromotion aside and restrict ourselves to the stroboscopic evolution of the system.

8.2.2 The Floquet operator

We now proceed by discussing the properties of the solutions to the Floquet problem. We begin by considering the one-cycle time evolution, commonly known as the "Floquet operator", which from now on we will simply write as $\hat{U}(T) = \hat{U}(T,0)$. Let us now consider the eigenstates of $\hat{U}(T)$, defined by

$$\hat{U}(T)\,|\phi_\alpha\rangle = e^{-i\epsilon_\alpha T/\hbar}\,|\phi_\alpha\rangle. \tag{8.5}$$

These $|\phi_\alpha\rangle$ are the so-called Floquet modes, and the ϵ_α the corresponding quasienergies. This is the perfect point to discuss the analogy existing between the problem of a potential periodic in time and a potential periodic in space, and thereby between Floquet's theorem and Bloch's theorem. In a spatially periodic potential, a continuous space-translation symmetry is broken into a discrete one, which is reflected by the invariance under a spatial translation operator $\hat{T}(a_{\text{lat}})$. This requires that the solutions of the problem will be given by eigenstates of the translation operator, and also that momentum is no longer a conserved quantity, but rather quasimomentum. In the Floquet case, $\hat{U}(T)$ plays the role of the translation operator, manifesting the discrete time translation symmetry, and leading to the conservation of the quasienergy instead of the energy. Making use of this analogy, one can apply Floquet's theorem, which says

that the family of solutions to the Schrödinger equation is of the form

$$|\psi_\alpha(t)\rangle = e^{-i\epsilon_\alpha t/\hbar}|\phi_\alpha(t)\rangle, \tag{8.6}$$

where $|\phi_\alpha(t)\rangle = |\phi_\alpha(t+T)\rangle$. These solutions $|\psi_\alpha(t)\rangle$ also obey

$$|\psi_\alpha(t+T)\rangle = e^{-i\epsilon_\alpha T/\hbar}|\psi_\alpha(t)\rangle. \tag{8.7}$$

Last, let us realize that the fact that $\hat{U}(T)$ describes a unitary evolution means that it can be expressed as the exponential of a time-independent Hermitian operator, as in Eq. 8.2, hence

$$\hat{U}(T) = \exp\left(-\frac{i}{\hbar}T\hat{H}_F\right). \tag{8.8}$$

$\hat{H}_F$ is the so-called "Floquet Hamiltonian", and describes the stroboscopic dynamics of the system. Note that the Floquet modes $|\phi_\alpha\rangle$ are eigenstates of $\hat{H}_F$ with eigenvalues ϵ_α, which are only defined modulo $2\pi/T$.

The relevance and beauty of the Floquet Hamiltonian resides on the fact that by periodically driving a system, one can effectively generate exotic dynamics which can be very different from the ones emerging from the original physical Hamiltonian. The calculation and study of this Hamiltonian is the main goal in Floquet engineering, which we will further discuss in the next section.

8.2.3 The Magnus expansion

Now that we have introduced the Floquet Hamiltonian, we ask the question of how can one obtain an accurate expression of $\hat{H}_F$ for some given drive parameters. This is desirable, for example, to tune the parameters to achieve some exotic target Hamiltonian. The answer is that one has to resort to expansion methods, since in general it is not possible to obtain an exact expression for $\hat{H}_F$. These expansions apply in particular to the high-frequency case, with the driving frequency $\omega = 2\pi/T$ well above the physical energy scales of the effective Hamiltonian. A common approach to this problem is the Magnus expansion [177, 201, 202], which gives a formal expression for $\hat{H}_F$ as

$$\hat{H}_F = \sum_{n=0}^{\infty} \hat{H}_F^{(n)}, \tag{8.9}$$

where each one of the $\hat{H}_F^{(n)}$ terms is given by a series of higher-order commutators. Note that this expansion can be seen as a continuous analog of the Baker-Campbell-

[1] The Baker-Campbell-Hausdorff formula is an expression to solve for Z in $e^X e^Y = e^Z$, where X, Y, Z are operators.

Hausdorff formula[1]. The first two terms of the Magnus expansion are

$$\hat{H}_F^{(0)} = \frac{1}{T}\int_0^T dt\, \hat{H}(t)\,, \tag{8.10}$$
$$\hat{H}_F^{(1)} = -\frac{i}{2T}\int_0^T dt_1 \int_0^T dt_2\, [\hat{H}(t_1), \hat{H}(t_2)]\,.$$

Higher order terms scale as $1/\omega^n$ for an order n, and because of this it is common to express Eq. 8.9 as an explicit high-frequency expansion $\hat{H}_F = \sum_{n=0}^{\infty} T^n \hat{\Omega}_n$. In general, this formal series will not converge. Among the few exceptions where it does, there is the case of single-particle system with a drive frequency ω above its energy bandwidth. But in the case of many-body systems a divergence of the series is the expected outcome. However, while the divergence arises from the contribution of higher-order terms which are relevant as $t \to \infty$, the transient dynamics for "short-enough" times can still be described by a truncated expansion

$$\hat{H}_{\text{eff}} = \sum_{n=0}^{m} \hat{H}_F^{(n)}\,, \tag{8.11}$$

defined up to some optimal order m, typically given by $m \sim \mathcal{O}(\omega)$. Note that, due to the definition of the individual terms, the unitarity of the time evolution operator is preserved even for a truncated expression.

8.3 Floquet thermalization

Until now we have, at least partially, neglected the elephant in the room: a periodically driven system does not fulfill energy conservation. The lack of a continuous time-translation symmetry implies that any initially prepared state will eventually heat to infinite temperature under a periodic drive. Such an infinite-temperature state will have trivial properties and will not display anymore any order shown in the transient regime. The heating process, commonly dubbed "Floquet thermalization", is a major bottleneck for any application of Floquet engineering. Nonetheless, it is at the same time a fundamentally interesting physical problem on its own.

8.3.1 ETH in Floquet systems

In Ch. 5 we already introduced the ETH and discussed its implications in the context of non-driven systems. We saw that in systems obeying ETH, the local observables of the individual eigenstates will have a smooth dependence on their energy density. When extending ETH to the periodically driven scenario, it leads to the driven eigen-

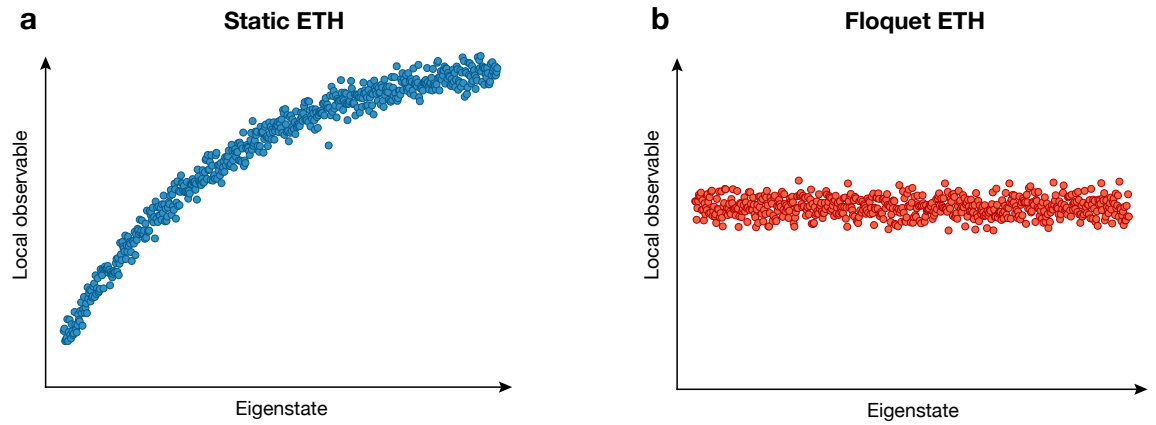

Figure 8.1: Eigenstate distributions for static and Floquet ETH systems. a Typical distribution of a local observable for each eigenstate in a static Hamiltonian, ordered according to their eigenenergy. **b** Equivalent distribution but in the case of a periodic Hamiltonian, ordered according to the quasienergy of each eigenstate. In contrast to the static case, where the observables changes smoothly, in the Floquet case it is essentially constant and the same for all eigenstates.

states, i.e. the Floquet modes $|\phi_\alpha\rangle$, involving a superposition of many eigenstates of the static Hamiltonian. These static eigenstates may correspond to very different energy sectors, and as a consequence, the local observables of the Floquet modes will be an average of those over the entire static spectrum, hence corresponding to states at $T = \infty$ (see Fig. 8.1). Additionally, the entropy of entanglement of all driven eigenstates will fulfill a volume law, with an entropy saturated to its maximum value [49].

Considering an arbitrary initial pure state $|\psi(0)\rangle$, which can be expressed as a superposition of Floquet modes, it will evolve in time as

$$|\psi(t)\rangle = \sum_\alpha c_\alpha \, e^{-i\epsilon_\alpha t/\hbar} \, |\phi_\alpha(t)\rangle. \tag{8.12}$$

Due to Floquet ETH, for $t \to \infty$ the system will ultimately thermalize to an infinite-temperature-like state.

This Floquet-ergodic phase is expected to generally show up in clean, interacting, driven systems. Given that these are properties that we would find in almost all physically relevant implementations of Floquet engineering, one could wonder what is the hope to realize exotic phases of matter, such as topologically non-trivial ones, which are long lived in driven systems. The answer is that we will require systems displaying a high number of conserved quantities, such that even after long times, the system

will not be able to efficiently thermalize.

8.3.2 Exceptions to Floquet ETH

Similar as our discussion in Sec. 5.2.2, we here consider which kinds of systems will lead to a breakdown of the process of Floquet thermalization. We will see that this will generally take place in quantum systems displaying an extensive number of integrals of motion.

Integrable Floquet systems

A first way to escape heating in periodically driven systems is integrability (briefly introduced in Sec. 5.2.2). Systems such as periodically driven free fermions or hard-core bosons in one dimension are some of the possible models [49, 203–205]. The out-of-equilibrium dynamics in such integrable Floquet systems end up relaxing into a periodic steady state, described by the so-called periodic Gibbs ensemble [203].

Again as in the static case, it is important to stress that such systems will only remain non-ergodic in fine-tuned regimes without the presence of integrability-breaking terms.

Floquet MBL

The only known way to generically hold Floquet thermalization indefinitely is via MBL [206–209]. Starting from a static MBL system, introducing a periodic drive at high enough frequencies will not lead to thermalization. In this regime, the system will just resemble a set of (quasi-)decoupled "spins" which are Rabi-driven [49]. This will, however, not be the case for low frequencies of the drive, since local resonances can be resonanly excited and trigger a heating avalanche of the whole system. Recently, the range of stability of a periodically driven MBL system was also experimentally studied [210].

The most important consequence of the breakdown of Floquet thermalization due to MBL is that it enables the existence of non-equilibrium phases of matter in periodically driven systems [188]. The paradigmatic example of such Floquet quantum matter is the recently discovered discrete time crystal (also referred to as the $\pi-$spin glass) [188–191, 196]. A time crystal is a phase of matter which, in a way, extends spontaneous symmetry breaking to the time domain (in analogy to a regular crystal, which does it in space). Such a phase is believed to not exist in systems with continuous time symmetry, but can be realized in periodically driven ones. The phase should display so-called discrete time-crystalline order, and recently such signatures were observed in systems of nitrogen-vacancy centers [192] as well as trapped ions [193]. In the former, the disorder emerged in the interactions due to the random positions

of the individual dipolar spins [211], while in the latter it was programmed as an effective onsite magnetic field [141].

8.3.3 Floquet prethermalization

From the discussion in the previous section, one concludes that MBL is the only generic solution to create driven phases of matter. However one might wonder if, instead of finding an absolute violation of ETH, one may find a "temporary" one. That means shifting the question of *whether* thermalization will happen to the question of *how quickly* will it happen. For this we leave aside these disordered or integrable non-ergodic Floquet phases, and focus again on the dynamics of interacting, clean, driven systems.

Even if the fate of such generic clean systems is to heat up to infinite temperature in the long-time limit, they might still display interesting dynamics in some transient timescales. Such a dichotomy in the dynamics of a system, is directly connected with the broader phenomenon of "prethermalization" [27, 212–214]. The dynamics of systems displaying prethermalization involve the relaxation of a non-equilibrium state through two well-separated timescales. In the first timescale, the system reaches a, potentially long-lived, "thermal-like" state. A second and slower timescale brings the system to its true thermal equilibrium. In static systems, these prethermal dynamics typically take place in scenarios close to integrability. In this section, however, we will be considering generic systems driven at high frequencies, which as we will see, display a similar prethermalizing behavior.

Thermal and prethermal Floquet dynamics

The dynamics of Floquet quantum systems, as we discussed in Sec. 8.2, can be described through a time-independent effective Hamiltonian $\hat{H}_{\text{eff}}$, which is made up of local terms and can be computed from a truncated Magnus expansion, as given in Eq. 8.11. This description is, however, only valid for short-enough times during which the energy is quasiconserved, but will eventually break down as higher orders of the expansion become significant. In many-body systems, these higher-order contributions introduce non-local couplings and will ultimately lead to the emergence of Floquet thermalization, i.e. heating. The timescale in which this heating process takes place, t_{th}, sets the range of validity of the quasi-conserved effective Hamiltonian $\hat{H}_{\text{eff}}$, which one can refer to as the "prethermal" Hamiltonian [215].

From a practical point of view, what is meaningful when considering the dynamics of driven systems is to compare the timescale t_{eff}, set by the prethermal effective Hamiltonian, with the thermalization timescale t_{th}. The goal in such systems is to remain in regimes with $t_{\text{eff}} \ll t_{\text{th}}$, and hence one desires t_{th} to be as high as possible. Note that in a real experiment, one could already compromise to work with a t_{th} well

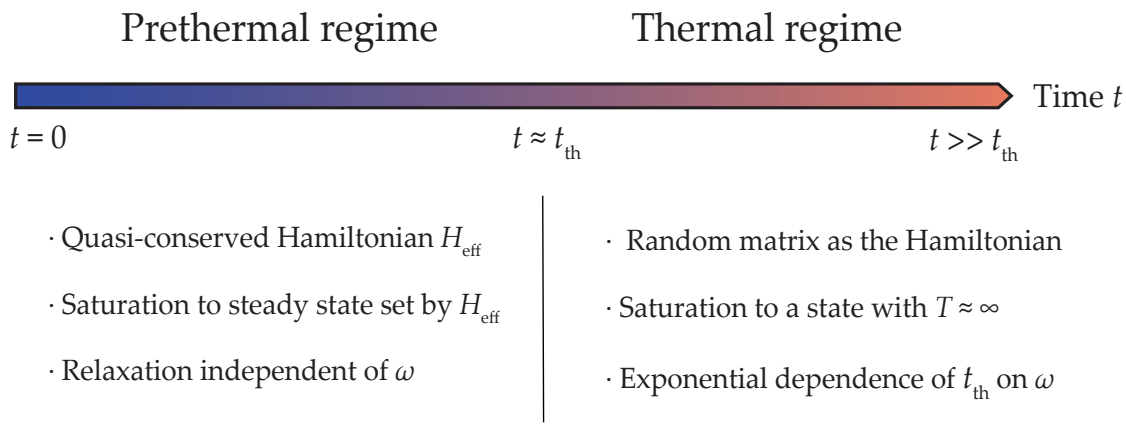

Figure 8.2: Schematic of the properties for the prethermal and thermal dynamics in driven many-body systems. For dynamics short in comparison to any Floquet thermalizing process, the system is well described by a prethermal Hamiltonian (blue range). This effective description eventually breaks down at longer times (red range).

above the accessible timescales of the setup (which could be technically limited).

Because of these arguments, which are schematically summarized in Fig. 8.2, an understanding of the heating processes taking place in many-body systems is of utmost importance, and has been recently intensely studied. Aside from any experimental implications, fundamental theoretical questions stem from this field such as the relation between the heating to infinite temperature and the divergence of the Magnus expansion, which are believed to be intimately connected [51]. A very important result, shown by many analytical and numerical studies, implies that for high frequencies of the drive, the prethermal Hamiltonian may capture the system dynamics for exponentially long times. This *more haste less speed* result implies that out-of-equilibrium phases of matter could be stabilized for arbitrarily times, even in the absence of MBL.

Exponential suppression of the heating

Recent studies have found that the thermalizing rates in some driven many-body systems can be exponentially suppressed as the driving frequency is increased [50, 51, 216–218]. While some of these rigorous analytical results have only been proven for lattice models with a bound local spectrum, such as for fermions or spin models, similar exponential bounds are expected for unbound bosonic systems [219]. The general idea is that for a system driven at a frequency $\omega \gg J_{\text{eff}}$, where J_{eff} denotes a typical local energy scale of the system, the thermalization time grows as $t_{\text{th}} \gtrsim O(e^{\hbar\omega/J_{\text{eff}}})$

(see Fig. 8.3). In general $\hat{H}_{\text{eff}}$ and t_{eff} would, however, not be modified for different frequencies. This exponential-in-frequency suppression of the Floquet heating rate is what is commonly referred to as "Floquet prethermalization".

To get more of a physical intuition into the origin of this phenomenon, let us consider a simple example. Take a physical system composed of many local degrees of freedom, each one of them displaying a non-interacting bandwidth E_{BW}. We now add to the system a periodic drive at frequency ω. In the absence of any interactions in the system, we expect the energy absorption from the drive to only take place when $\hbar\omega \lesssim E_{\text{BW}}$. If we now introduce a short-ranged interaction in the system, any frequency that falls within the many-body bandwidth (which will diverge in the thermodynamic limit) can be absorbed by the system. This means that the system will indefinitely absorb energy from a drive with an arbitrary frequency. However, due to the local character of the system, absorbing a single quantum of excitation from the drive will in general require a number $N \sim \hbar\omega/E_{\text{BW}}$ of rearrangements of its local degrees of freedom. This absorption process will become inefficient and be strongly reduced for higher frequencies, since it will involve high-order processes.

This kind of phenomenon, in which a single high-energy state gets converted into collective low-energy ones, is also similar to the one observed in the elastic decay of doublons in the Fermi-Hubbard model [220]. In that case, the interaction energy of the doublon U needs to be redistributed among the (bound) kinetic energies of several individual fermions in the lattice, which leads to an exponential-in-interaction lifetime of the doublons.

8.4 Ideal regimes for driven lattices

In this section we discuss what is the suitable range for the driving frequencies in real Floquet physical systems. In particular, we will consider a system of particles in a periodic potential, relevant for the description of ultracold atoms in optical lattices.

From the results discussed in this chapter, it seems obvious that to realize long prethermal regimes one must drive the system at frequencies as high as possible. While this might be technically limited, due to the unfeasibility of driving certain physical parameters arbitrarily fast (e.g. magnetic fields, laser intensities), a priori there seems to be no reason to avoid pushing in this direction. However most theoretical works dealing with Floquet prethermalization assume the absence of degrees of freedom additional to the ones that are explicit in the microscopic model. This assumption will not remain valid for most real physical systems, in particular for lattice models, where high-energy states will be inevitably present.

To provide a concrete example, consider how we commonly describe the physics

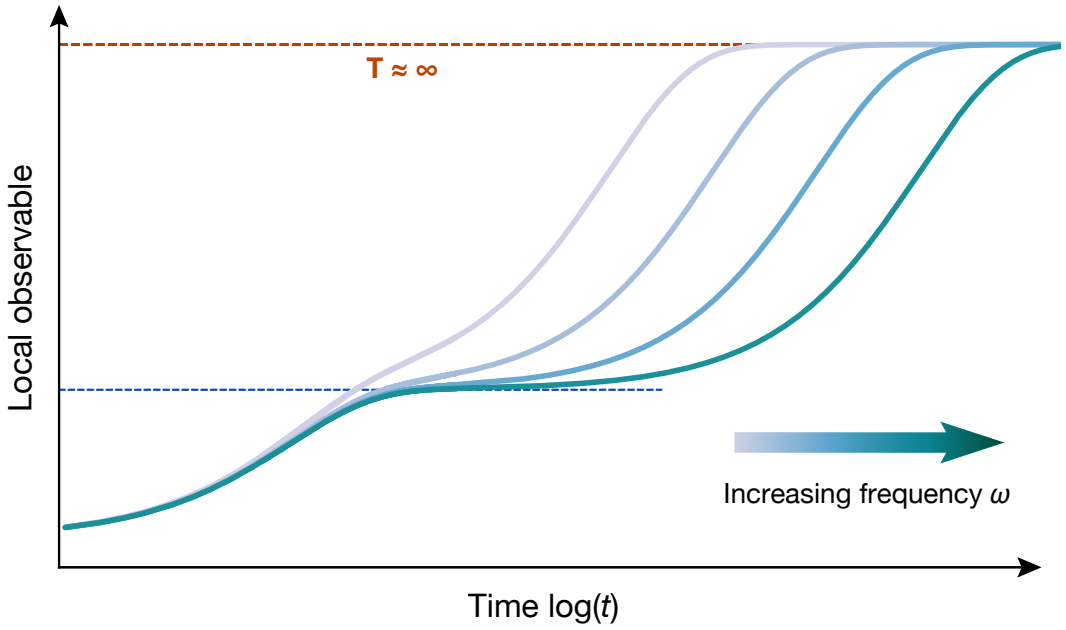

Figure 8.3: Floquet prethermal dynamics in a log-lin plot. Illustration of the evolution of a local observable in a driven system exhibiting Floquet prethermalization. After initiating the drive, the dynamics start and take the system towards a steady-state (dashed blue line), related to its effective prethermal Hamiltonian $\hat{H}_{\text{eff}}$. For much longer times, Floquet thermalization takes the system from this quasi-steady state to a featureless infinite-temperature one. This happens with a timescale that exponentially diverges as the frequency of the drive is linearly increased (gray-to-green colormap).

of ultracold bosonic atoms in an optical lattice with the Bose-Hubbard model, thereby restricting the effective energy subspace to the lowest Bloch band (see Ch. 2). The validity of this approximation is particularly challenged in the presence of a periodic drive, where resonant coupling to states $\hbar\omega$ apart in energy might take place. For any finite drive, these higher states will be populated at a certain rate, and we then rely on the timescales of the physics we explore to be much shorter than the emergence of those rates. For those rates to be small, the energy of the drive quantum $\hbar\omega$ needs to be well below the gap to the relevant excited band Δ. This is commonly called the "low-frequency approximation" [221]. However, even fulfilling $\hbar\omega \ll \Delta$, multiphoton interband transitions can take place for strong enough drives. Because of this, it is also required that the amplitude of the drive g remains low enough to avoid mth-order multiphoton transitions, with $m \approx \Delta/\hbar\omega$.

Putting everything together, we conclude that there is only a narrow range of

frequencies (if any at all) for which Floquet engineering is suitable in such lattice systems. On the one hand it is required to be in the high-frequency limit, $\hbar\omega \gg J$, (where J represents a local energy scale in the microscopic model), and on the other one $\hbar\omega \ll \Delta$ and $g \ll 1$ to ensure the low-frequency approximation. These conclusions will be used in the experiment in the following chapter, to ensure that no higher bands are populated due to the periodic drive.

8.5 Summary

In this chapter we have covered the basic concepts of Floquet quantum systems and their dynamics. We have also gone through the thermodynamical implications of ETH in the case of driven systems, which explains the process of Floquet thermalization. We have discussed in which cases one can approximate the dynamics of the system with an effective time-independent description, and discussed for how long. We have then seen that driving at high frequencies can dramatically increase the timescale for Floquet engineering, and explained its relation to the Magnus expansion.

Finally, we have also discussed how driving at arbitrarily high frequencies will lead to interband transitions and which criteria must be fulfilled in the driving of systems like our setup. Many of these ideas will be revisited again in the next chapter, in which we experimentally probe Floquet prethermalization.

Chapter 9

Floquet prethermalization in a Bose-Hubbard system

In this chapter we describe experiments in a driven quantum gas providing evidence of the phenomenon of Floquet prethermalization, taken as an exponential-in-frequency decrease in the heating. We first motivate the challenges and the importance of this research direction, which were already partially introduced in Ch. 8. We then continue with the experimental implementation of the driven system and the temperature measurement scheme. We present measurements of the dynamics of the system in two dimensions, which already illustrate the thermalization process and its rate reduction for high driving frequencies. We then turn to discuss the spectral response of the system in one and two dimensions, extracted from a single-site-resolved thermometry method, which shows indications of an exponential-in-frequency reduction. From comparing the experimental results with a spectrum obtained numerically we gain insight into the heating processes in our system. The contents of this chapter are based on the preprint article *Floquet prethermalization in a Bose-Hubbard system* [222].

9.1 Introduction

In the previous chapter we explained that generic many-body driven systems will thermalize to an infinite-temperature state. While systems with disorder or fine-tuned parameters might provide exceptions to this heating outcome [206–210, 215], we also saw that an alternative route is opened when the system is driven at high-enough frequencies. Even if heating must eventually take place in generic interacting and clean systems, the timescale at which this happens has been shown to be exponentially bounded for frequencies of the drive well above local energy scales in the system [50–52, 216–218, 223–231].

At the same time, many recent experiments have addressed the topic of heating in driven many-body systems, particularly in the field of ultracold atoms. The energy absorbed from the drive by the system has been probed in both fermionic and bosonic systems, by tracking the momentum distribution, the occupation in the bands, or the

production of doublons [179, 232–236]. In another very recent experiment, the band population of a condensate in an optical lattice was tracked under an extremely strong driving [237] and showed signatures of prethermal plateaux.

It has nonetheless remained elusive to experimentally identify Floquet prethermalization based on its frequency-dependent heating. One of the main challenges for such a demonstration is the necessity of probing dynamics in time ranges which can differ by few orders of magnitude. This means that the isolation of the system must be able to preserve the coherence of the system on times longer than the heating processes that are the goal of the study. Another big limitation, especially in trapped atomic systems, is the existence of degrees of freedom energetically above the low-energy microscopic model (such as higher bands on top of the Bose-Hubbard model). This means that the dynamic range for the driving frequency can easily become too small to appreciate any exponential dependence.

In this chapter we describe an experiment in which we observed evidence of an exponential-in-frequency suppression of the heating rates in a driven interacting lattice system. The driving is based on a periodic modulation of the amplitude of the optical lattices in the plane. This experiment mainly benefits from the low bare heating in our system (see Ch. 3) and from quantum-gas microscopy, which enables high-sensitivity thermometry [9]. These two properties make it possible to track the dependence of the heating dynamics while remaining in the weak-drive regime.

The optical-lattice tuning allows us to explore both the setting of one- and two-dimensional systems, and also a range of different interacting regimes. By studying the response of the system both in the superfluid and the Mott-insulator side, we appreciate that the exponential dependence is cleaner in the weakly interacting superfluid. Additional features on top of the overall exponential trend are associated to its Bogoliubov spectrum. On the other hand, the Mott insulator shows a highly non-monotonic response, directly explained by the excitation of higher occupations in each lattice site. In both of the regimes, we see the heating rate substantially reduced, even as much as by two orders of magnitude, while remaining in a modest frequency range. Numerically obtained spectra bring additional confidence to the interpretation based on the measured data.

9.2 The experimental setup

We start the experiment by preparing a two-dimensional cloud of ultracold ^{87}Rb atoms, which are trapped in a single antinode of a vertical optical lattice. The cloud is then slowly loaded into the in-plane optical lattices at depth V_0. The total atom number is fixed in such a way that the central part of the trap has an occupation close

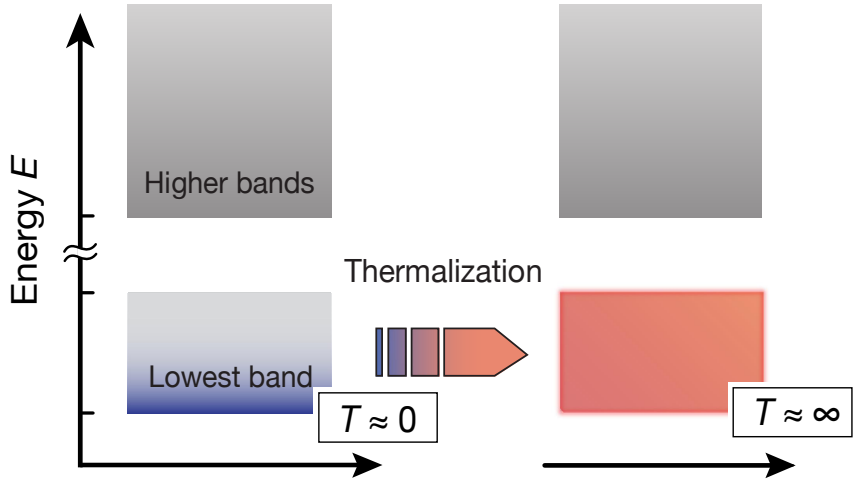

Figure 9.1: Schematic of the process of Floquet thermalization in our experiment. Starting from a low-temperature state in the lowest band of the system, the energy absorbed from the drive eventually brings the system to a single-band infinite-temperature state without populating any of the higher bands.

to one atom per lattice site, and that is $N_{\text{at}} \simeq 200$. At the cold temperature at which we prepare the cloud, all atoms populate only the ground band of the lattice potentials and, similarly to the rest of experiments in this thesis, can be captured by a 2D Bose-Hubbard model, described by the following Hamiltonian:

$$\hat{H}_0 = -J \sum_{\langle i,j \rangle} \hat{a}_i^\dagger \hat{a}_j + \frac{U}{2} \sum_i \hat{n}_i (\hat{n}_i - 1) + \sum_i \epsilon_i \hat{n}_i. \tag{9.1}$$

As in Eq. 2.1, $\hat{a}_i$, $\hat{a}_i^\dagger$ and $\hat{n}_i$ respectively denote the annihilation, creation and number operators at a site $\boldsymbol{i}$ of the square lattice [$\boldsymbol{i} = (i_x, i_y)$], J is the hopping amplitude, U the on-site interaction energy, and ϵ_i the potential of the harmonic trap. This is given by $\epsilon_i = m a_{\text{lat}}^2 (\omega_x^2 i_x^2 + \omega_y^2 i_y^2)/2$, where ω_x and ω_y are the frequencies of the harmonic trap. Notice that these frequencies will in general depend on the lattice depth. In this experiment they fall in the range of $2\pi \times 45\,\text{Hz} < \omega_x, \omega_y < 2\pi \times 55\,\text{Hz}$. Until this stage of the experiment, virtually no heating has taken place, and thereby the atoms are close to the ground state of $\hat{H}_0$. Now we proceed by modulating the depth of the in-plane lattices in a sinusoidal way, that is as $V(t) = V_0(1 + A\cos(\omega t))$ where A is the normalized modulation amplitude. This drive leads to a modulation of all the parameters in the Hamiltonian (see Fig. 9.2), but since the tunneling strength depends

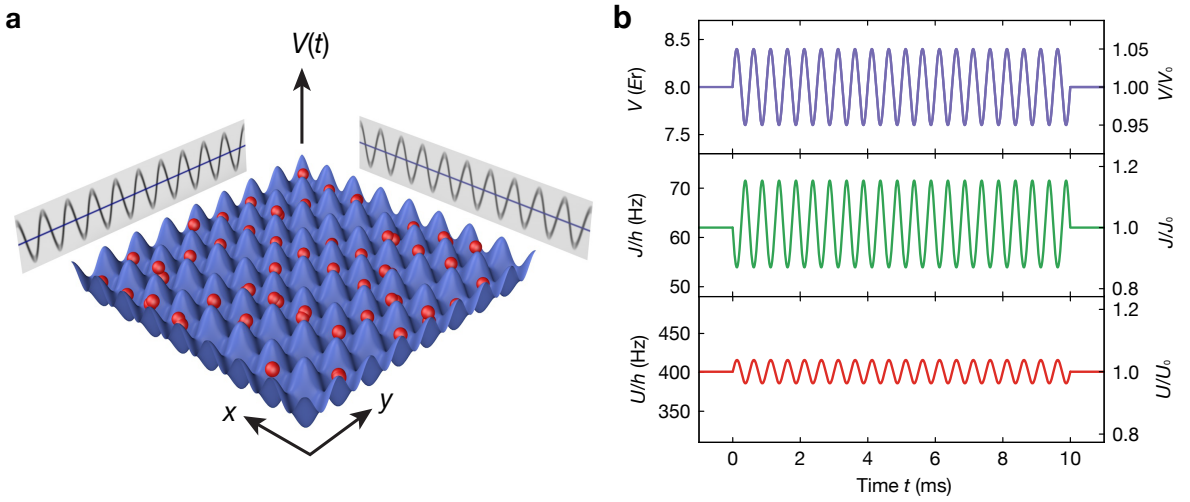

Figure 9.2: Schematic of the experimental setup and the lattice modulation. a Schematic drawing of the two-dimensional system of ultracold atoms loaded in a driven optical lattice. **b** Plots of the periodic modulation of the lattice depth V and the calculated dependence of the Bose-Hubbard parameters J and U. The modulation is done for a bare lattice depth of $V_0 = 8\,E_\mathrm{r}$ and a modulation frequency of $\omega = 2\pi \times 2\,\mathrm{kHz}$.

exponentially on the lattice depth, it has the biggest contribution. Hence,

$$\hat{H}(t) \approx \hat{H}_0 + g\cos(\omega t)\,\hat{O}_\mathrm{drv}, \tag{9.2}$$

where $g = \delta J/J$ and $\hat{O}_\mathrm{drv} = J\sum_{\langle i,j\rangle} \hat{a}_i^\dagger \hat{a}_j$ implements the drive. This driving technique is quite common in experiments of ultracold atoms in optical lattices [238, 239]. During the driving, the atoms can in principle be transferred into the higher bands of the system. To ensure that this is not the case, we track any atoms appearing in regions of high potential energy (far from the center of the cloud). This leads to the requirement of restricting the driving frequencies below the first bandgap [221] and using a weak modulation aplitude, $A \ll 1$, since multi-photon transitions are also expected to take place [240].

The system is driven for a certain duration, commensurate with the driving period, and stops after a number of Floquet cycles $N_\mathrm{cyc} = \omega\, t_\mathrm{drv}/2\pi$. Then, we ramp adiabatically the lattice depth to the atomic limit. In this regime, the tunneling dynamics is frozen and, if no energy is absorbed during the drive, results in a near unit-filling Mott insulator. Finally, we perform fluorescence imaging to extract the atomic occupation (see Ch. 3). Any heating processes during the driving of the cloud will lead

to the presence of defects in the atomic limit, which will increase the variance of the single-site occupation. Because of parity projection, this increase in temperature is directly linked to a growth of the density of measured empty sites (holes). Thus, we can use the density of holes as a proxy for the energy density of the system, and therefore track the heating dynamics.

9.3 Probing the thermalization dynamics

We now focus on following the heating dynamics in the cloud for very long times. The evolution of the density of holes ρ_h is plotted in Fig. 9.3 for four different driving frequencies. Those measurements were taken at a lattice depth of $V_0 = 8\,E_\mathrm{r}$ and with a modulation amplitude of $A = 0.05$. The four different datasets manifest a qualitatively similar evolution, though the rates of the thermalization are vastly different. An increase of less than twice in the driving frequency gives rise to a timescale difference over more than one and a half orders of magnitude. This strong dependence on the frequency of the drive is an indication of an exponential suppression of the heating, as is characteristic for Floquet prethermalization.

In terms of the energy density, in our experiment we expect a linear increase in time followed by a saturation at long times to the infinite-temperature energy density. We can describe then the dynamics of the density of holes ρ_h by the expression

$$\rho_\mathrm{h}(N_\mathrm{cyc}) \simeq \rho_0 + (\rho_\infty - \rho_0)\left[1 - \exp(-N_\mathrm{cyc}/N_\mathrm{cyc}^\mathrm{th})\right], \tag{9.3}$$

where ρ_0 is the low-temperature value measured in the absence of the drive, ρ_∞ the infinite-temperature value, and $N_\mathrm{cyc}^\mathrm{th}$ is the timescale of thermalization in number of Floquet cycles.

The solid lines in Fig. 9.3 are fits of the data based on Eq. 9.3, which show good agreement. The fitted values of $N_\mathrm{cyc}^\mathrm{th}$ go from 4×10^2 cycles for $\omega = 19.3\,J/\hbar$ to 10^4 cycles for $\omega = 35.5\,J/\hbar$. The longest measured times in those datasets are above $3000\,\hbar/J$, which indicates the high degree of isolation in our system. In contrast to what we discussed in Sec. 8.3.3, we do not expect any short-time dynamics during the prethermal regime in our experiment. This is explained by the fact that our initial state is already in thermal equilibrium with respect to the effective Hamiltonian $\hat{H}_\mathrm{eff}$.

In addition to these experimentally observed dynamics, in App. C we show numerical simulations based on Krylov subspace method for the time evolution [241], which indicates similar dynamics of the density of holes. By comparing the dependence of the simulated energy density and the simulated density of holes, we further support the interpretation of ρ_h as a proxy for the energy density.

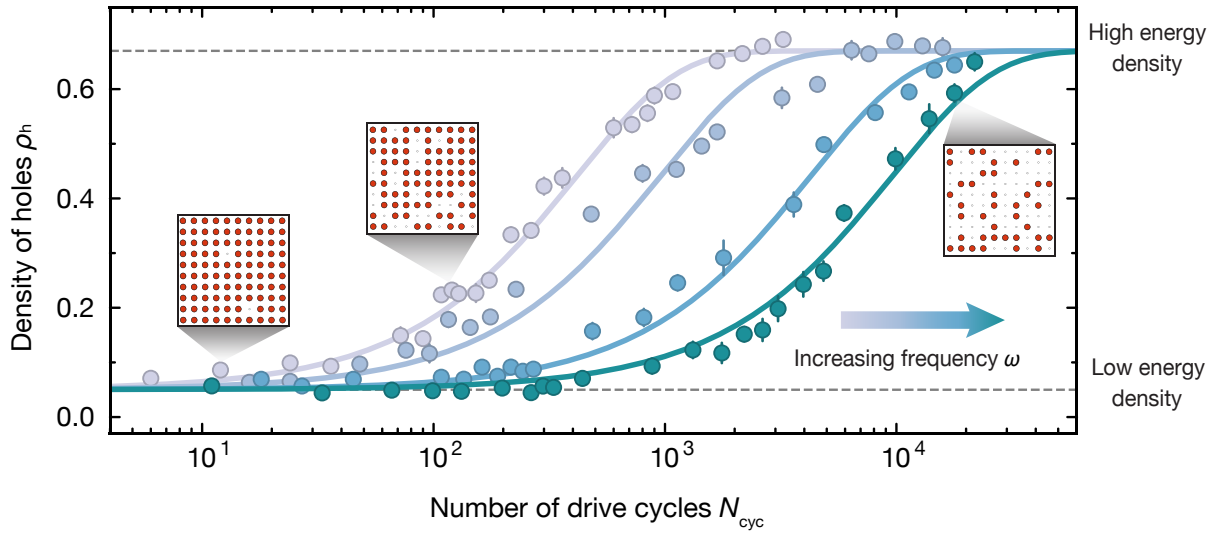

Figure 9.3: Floquet thermalization dynamics of the density of holes. Lin-log plot of the density of holes as a function of the number of Floquet cycles N_{cyc}. We show four different datasets, all in the superfluid regime at $V_0 = 8\,E_{\mathrm{r}}$ with a $J/U = 0.16$, at four different driving frequencies: $\omega = 19.3\,J/\hbar$ (gray), $\omega = 25.8\,J/\hbar$ (light blue), $\omega = 29.0\,J/\hbar$ (blue) and $\omega = 35.5\,J/\hbar$ (green). The density of holes is based on a region of interest of 10×10 sites in the center of the trap. The solid curves are the respective fits to the exponential form in Eq. 9.3. The separation between the different thermalization timescales separated is of more than an order of magnitude. The errorbars denote the standard error of the mean (s.e.m.). The box insets indicate the reconstructed atomic number distribution (red circles) in the center of the cloud for three example snapshots.

9.4 Dynamics in the linear regime

While by observing the dynamics of $\rho_{\mathrm{h}}(t)$ we obtain a qualitative illustration of the phenomenon of Floquet prethermalization, our quantum-gas microscope further allows for a precise characterization of the temperature of the cloud and hence of the heating rates. For this we use our thermometry method based on a grand-canonical fit [9, 239], which is described in Sec. 3.2.4.

This technique makes it possible to extract the temperature from a single shot, and allows us to quantiatively characterize the heating induced by the drive. A great advantage of it is that it is sensitive enough to allow us to remain in the regime of linear heating, such that even by driving the system with a relatively small amplitude A the heating rates can be identified. By remaining in the weak-drive regime, we can

strongly suppress any multiphoton interband transitions. This weak-drive probing contrasts with recent measurements of the response of Bose-Einstein condensates in one and two-dimensional optical lattices [235, 236], which focused on the emergence of parametric instabilities under strong drives.

In Fig 9.4 we plot the temperature dynamics of a superfluid driven at $V_0 = 6\,E_r$ for four different driving frequencies and with a relative driving amplitude $A = 0.05$. The time trace seems consistent with the linear regime of the heating processes. The heating rate per Floquet cycle $\phi(\omega)$ can be then extracted as $\phi(\omega) = k_B\, dT/dt \times 2\pi/\omega$, where k_B is the Boltzmann constant, T is the measured temperature, and $2\pi/\omega$ is the drive cycle period. Furthermore, we have studied the heating rates at a fixed drive frequency for different drive amplitudes A, plotted in Fig. 9.5, and which behaves according to the prediction of Fermi's Golden Rule, i.e. proportional to A^2. The fit of a power law, given by the function $\phi(A) = c\,A^{\alpha}$, gave consistently the result of $c = 4.0(4)$ and $\alpha = 2.11(4)$.

In summary, our sensitive thermometry technique allows us to faithfully compare the rates of heating per Floquet cycle $\phi(\omega)$ for different amplitudes and driving frequencies, which is a crucial requirement to identify Floquet prethermalization as an exponential-in-frequency dependence.

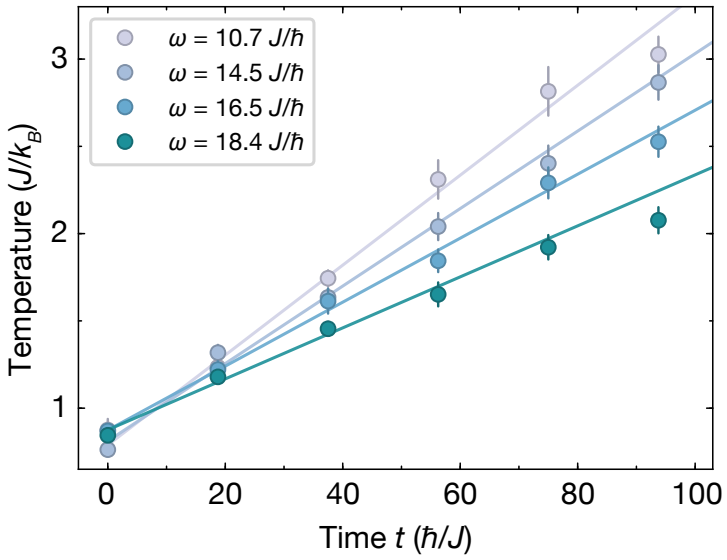

Figure 9.4: Heating dynamics in the linear regime. Temperature of a driven system with $V_0 = 6\,E_r$ for four different frequencies of the drive as a function of evolution time t. The continuous lines are linear fits. The errorbars denote the s.e.m.

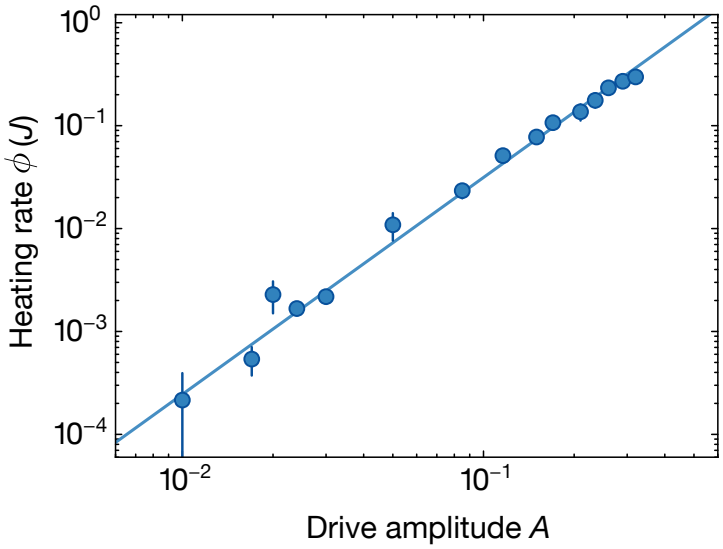

Figure 9.5: Fermi-golden-rule scaling. Heating rate as a function of the drive amplitude on a log-log scale. The data was taken at $V_0 = 8\,E_\mathrm{r}$ with driving frequency $\omega = 14.5\,J/\hbar$. The solid line is a power-law fit, compatible with a dependence on A^2. The errorbars denote the s.e.m.

9.5 1D spectrum from numerics

Before exploring the spectral results obtained in the experiment, let us first develop some intuition by considering few numerical results for the heating in the Bose-Hubbard model. These numerical calculations were carried out by Matteo Ippoliti and Vedika Khemani [222], and are based on numerical exact diagonalization.

While Floquet prethermalization is expected even for arbitrarily strong drives, this experiment remains in the regime of weak modulation, i.e. $g \ll 1$. Because of this, the energy absorbed per Floquet cycle is well captured by the linear response theory, identified with the dissipative part of the response function,

$$\Phi(\omega) = \sum_{n\neq 0} |\langle n|\hat{O}_\mathrm{drv}|0\rangle|^2\,\delta(E_n - \hbar\omega), \tag{9.4}$$

where $\{E_n, |n\rangle\}$ are the eigenvalues and eigenvectors of the average Hamiltonian $\hat{H}_0$ ($|0\rangle$ labels the ground state, with energy $E_0 = 0$), and the driven operator $\hat{O}_\mathrm{drv}$ is defined in Eq. 9.2.

The heating $\Phi(\omega)$ was bounded rigorously by an exponential envelope in Ref. [50]. It has units of energy and for weak drives is proportional to the energy

absorbed per Floquet cycle, $dE/dN_{\mathrm{cyc}} = \phi(\omega) \sim g^2\Phi(\omega)$.

By performing exact diagonalization (ED) we can compute $\Phi(\omega)$ for a 1D chain at unit filling with $L = 9$ sites. No harmonic potential is considered, due to the small system size, but instead open boundary conditions are used. While the ED approach is very limited in size, it offers great flexibility in choosing the ratio J/U and the driving frequency ω. At the same time, it allows us to probe almost arbitrary long timescales (while remaining in the linear response regime). We show the obtained results in two different plots, to stress the individual features of the two ground-state phases. In Fig 9.6 we plot the results in the superfluid side, with both Φ and ω expressed in units of the tunneling strength J. In Fig 9.7 the results in the Mott-insulator regime are instead expressed in units of the interaction strength U.

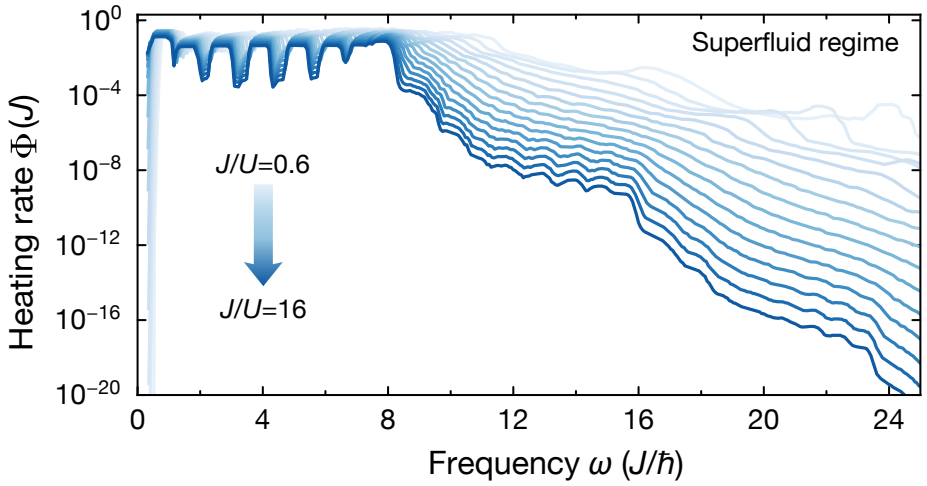

Figure 9.6: Numerical spectra of the heating rate $\Phi(\omega)$ in the superfluid regime in 1D. We plot the linear-response heating rate $\Phi(\omega)$ as a function of the driving frequency, obtained from an exact-diagonalization calculation on a unit-filling chain of $L = 9$ sites. Both Φ and ω are expressed in units of the tunneling strength J. The value of J/U varies from 0.6 (lightest blue) to 16 (darkest blue). The value of J/U at the critical point is approximately $(J/U)_{\mathrm{c}} = 0.26$.

In the weakly interacting limit of the the superfluid phase, the spectrum shows a very efficient heating for frequencies below $\omega = 8J/\hbar$ (with some dips, which are a finite-size feature of the numerics) followed by a sharp suppression, in an exponential way, together with additional kink-like features for multiples of $8J/\hbar$. These results directly suggest that the heating mechanism is based on a quasiparticle excitation on top of the condensate. Since the driving method used in our experiment, described by Eq. 9.2, does not transfer any net momentum, the excitation of quasiparticles must

take place in pairs of opposite momenta $\pm q$. If the driving frequency is set above Ω_{2qp}, which is twice the quasiparticle bandwidth, the absorption by the system of an energy quantum with energy $\hbar\omega$ must involve the scattering of multiple pairs, such that each additional scattering event will be suppressed by factors with $U/J \ll 1$. This directly connects with the intuition behind Floquet prethermalization, as discussed in Sec. 8.3.3, and explains the observed exponential scaling and the features seen in in Fig. 9.6 for multiples of $8J/\hbar$, which is twice the non-interacting bandwidth. As interactions are increased, i.e. a smaller J/U, many of the above features get washed out and the kink feature at Ω_{2qp} is shifted according to the prediction for the Bogoliubov bandwidth $\Omega_{2qp} \simeq 8J/\hbar\sqrt{1+U/2J}$.

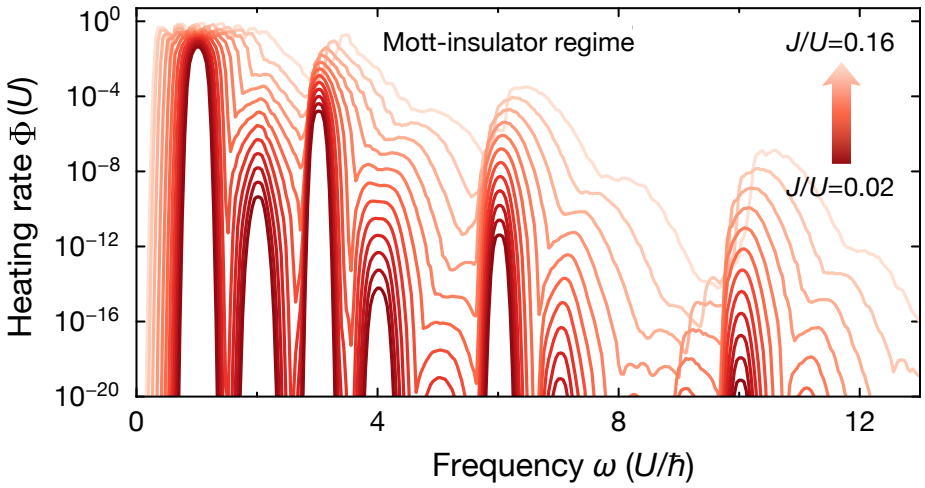

Figure 9.7: 1D numerical spectra of the heating rate $\Phi(\omega)$ in the Mott-insulating regime. We plot the linear-response heating rate $\Phi(\omega)$ as a function of the driving frequency, obtained from an exact-diagonalization calculation on a unit-filling chain of $L = 9$ sites. Both Φ and ω are expressed in units of the interaction strength U. The value of J/U varies from 0.02 (darkest red) to 0.16 (lightest red). The value of J/U at the critical point is approximately $(J/U)_c = 0.26$.

When increasing the interactions beyond the transition from superfluid to Mott insulator (see Fig. 9.7), new spectral features emerge given by sharp peaks for multiples of $U/\hbar$, which are associated to higher occupations in each lattice site (two, three, etc.). A more detailed discussion on the relative heights of those peaks and their derivation from perturbing an atomic-limit Mott insulator can be found in the Appendix of [222].

While these numerical results were restricted to the linear response regime, in App. C we verify that a qualitatively similar picture remains even outside of it, by

considering the exact time evolution of the system to infinite temperature.

9.6 Experimental spectrum in 2D

We now take a look at the spectra obtained experimentally, by measuring the heating rate per Floquet cycle $\phi(\omega)$, based on the method described in Sec. 9.4. We first consider a purely two-dimensional system with lattice depths within $V_0 = 5 - 11\,E_r$ and a drive set with a fixed modulation $A = 0.05$. The results are shown in units of the tunneling strength J in Fig. 9.8, and reveal a clear suppression of the heating as we increase the frequency, extending over more than two decades in the measured frequency range. Such a stark arrest of the rates of Floquet thermalization is evidence for a Floquet prethermal regime.

In the superfluid phase, that is for J/U higher than the critical point $(J/U)_c \simeq 0.06$ [242], the behavior is qualitatively the same for all datasets, consisting of a monotonic decrease of the heating rates. These datasets also display an approximately exponential dependence, and for the two weakest interacting sets we fit an exponential function of the form $\phi(\omega) = C\,e^{-\hbar\omega/J_{\text{eff}}}$, from which we obtain their effective local energy scales $J_{\text{eff},1} = 5.76(16)\,J$ and $J_{\text{eff},2} = 5.9(2)\,J$ (see dotted lines in Fig. 9.8). Note that, as expected, the extracted values of J_{eff} are on the same order of magnitude as J and U.

Shifting to stronger interactions, we observe a visible kink emerge in addition to the bare exponential trend. In Sec. 9.5 we discussed that the dominant heating process in the superfluid phase is the creation of quasiparticle pairs of opposite momenta. Based on this process we expect a reduction on the heating to take place for frequencies of the drive higher than twice the Bogoliubov bandwidth, which in the 2D case is $\Omega_{2\text{qp,2D}} = 2 \times 8J/\hbar\sqrt{1 + U/4J}$ [223]. Five small arrows indicate the position of $\Omega_{2\text{qp,2D}}$ in Fig. 9.8 for the first four datasets, showing a rough agreement with the kink-like features seen in the data.

We note that, however, the heating rates do not stay flat below twice the single-particle bandwidth ($2 \times 8J/\hbar$ in 2D), in contrast to what we observed in the 1D numerics. The reason for this difference can be explained by the shape of the density of states in the tight-binding model of a square lattice in two dimensions. In 2D, the density of states peaks in the middle of the band, making the quasiparticle excitation most efficient in the middle of the 2-quasiparticle bandwidth, which is roughly $\omega \approx 8J/\hbar$ [243]. One last point to notice is that, for higher J/U, the measured dynamic range of driving frequencies gets limited to lower values. The reason for this is that higher values of J require higher absolute frequencies for the drive to observe prethermalization, which poses a more severe limit due to an enhancement of interband transitions.

Considering now the regime of even stronger interactions, we see new features emerge. To better identify them, in Fig. 9.9 we plot the same results as in Fig. 9.8 but in units of the interaction strength U. The strongest interacting dataset was measured at $J/U = 0.06$, which is in fact the only one strictly in the Mott-insulating phase, and shows spectral peaks at $\omega = U/\hbar$ and $3\,U/\hbar$, asymptotically corresponding to the doublon and triplon resonances respectively. As interactions are reduced, one can see how these spectral features fade into a continuum towards the superfluid phase, in a similar fashion to what we saw in the numerics in Fig. 9.7.

Finally, notice that the smallest measured heating rates, appearing in the limit of high drive frequencies, reach the sensitivity limit of the experiment. Due to the very long measurement times and the contribution of background heating, this leads to a noise floor that will in general depend on the specific value of J/U.

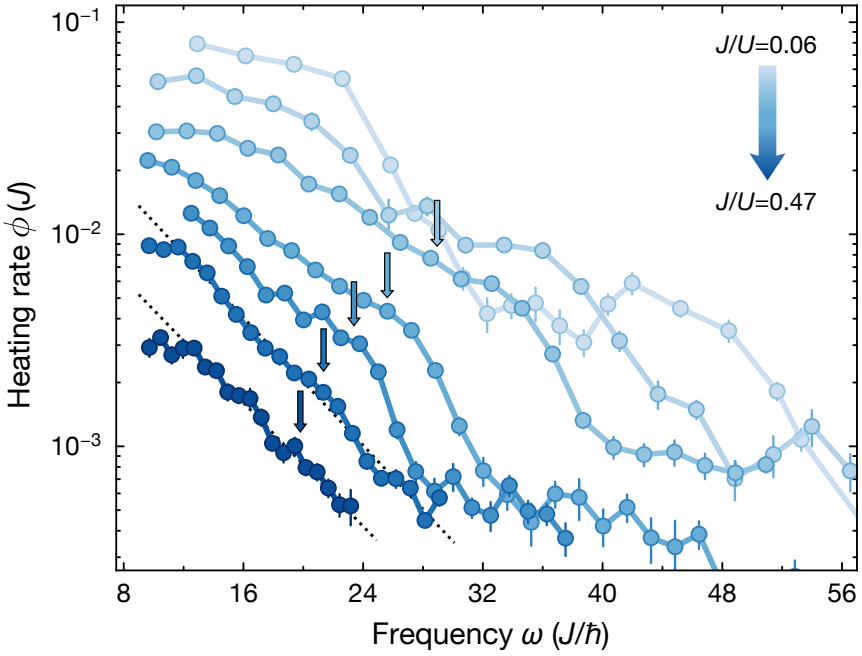

Figure 9.8: 2D experimental heating rates vs driving frequency in units of J. Measured heating rates per Floquet cycle $\phi(\omega)$, expressed in units of the tunneling strength J, for a two-dimensional system. The datasets were measured for the range of lattice depths $V_0 = 5 - 11\,E_r$, varying from shallower (dark blue) to deeper (light blue) lattices. The corresponding values of J/U are $0.47 - 0.06$. The errorbars denote the s.e.m. We indicate the value of $\Omega_{2qp,2D}$ for the first five datasets with five small arrows. Two dotted line indicates exponential fits to the first two datasets.

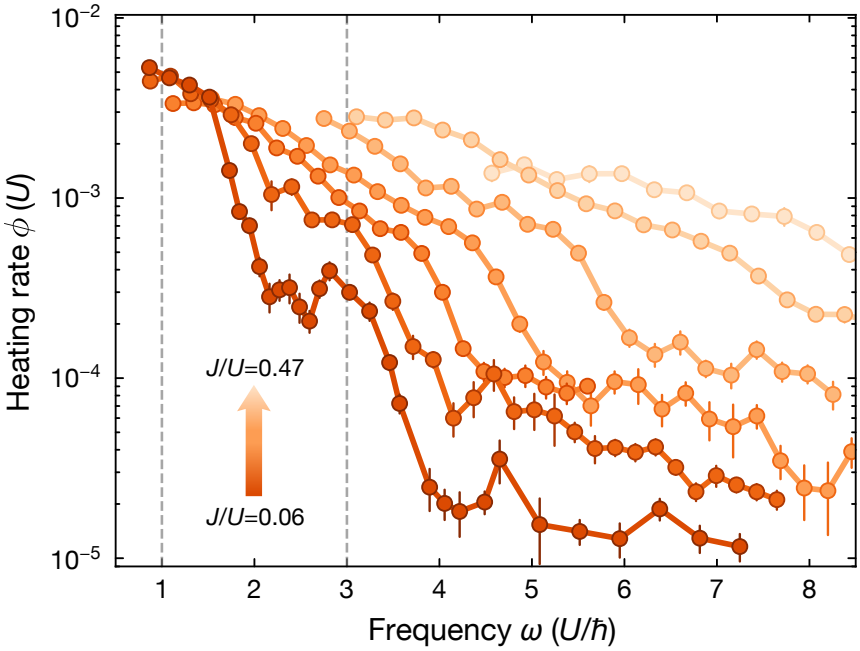

Figure 9.9: 2D experimental heating rates vs driving frequency in units of U. Measured heating rates per Floquet cycle $\phi(\omega)$, expressed in units of the on-site interaction strength U, for a two-dimensional system. The datasets are the same as in Fig. 9.8, measured in the range of lattice depths $V_0 = 5 - 11\,E_\mathrm{r}$, varying from deeper (dark orange) to shallower (light orange) lattices. The corresponding values of J/U are $0.47 - 0.06$. The errorbars denote the s.e.m. The dashed vertical gray lines indicate the doublon and triplon resonances at $\omega = U/\hbar$ and $3\,U/\hbar$ respectively.

9.7 Experimental spectrum in 1D

Our experimental setup also allows us to produce one-dimensional systems. This is achieved by ramping one of the in-plane lattices, in this case the one along the y axis, to an atomic-limit depth of $V_{0,y} = 20\,E_\mathrm{r}$ before the driving pulse starts. The confinement of the transverse lattice contributes to the harmonic trap with a roughly constant value of $\omega_x \simeq 2\pi \times 70\,\mathrm{Hz}$, and leads to the typical size of the system being of $N_\mathrm{at} \simeq 15$.

In Fig. 9.10 we plot the measured heating rates in the 1D geometry, in units of $J \equiv J_x$, for lattice depths in the range $V_{0,x} = 3 - 9\,E_\mathrm{r}$ and driven by a relative lattice modulation of $A_x = 0.1$ (while $A_y = 0$). In this case we also identify a sharp exponential suppression of the heating as the frequency of the drive ω is increased, though we note that for $\omega < 8\,J/\hbar$ we observe an almost flat dependence of $\phi(\omega)$, much in

agreement with the numerical results shown in Fig. 9.6. This behavior can be mainly explained in terms of twice the non-interacting bandwidth, $2 \times 4J/\hbar$, though we also observe a second kink-like behavior at slightly higher frequencies, which shifts to higher frequencies for stronger interactions. Four small arrows in Fig. 9.10 point the position of two times the Bogoliubov bandwidth $\Omega_{2\mathrm{qp,1D}} = 2 \times 4J/\hbar\sqrt{1 + U/2J}$ for the first four datasets. This shows a reasonable agreement which eventually gets discrepant for smaller J/U. For reference, we also fit an exponential to the dataset with $J/U = 0.62$, obtaining the local energy scale $J_{\mathrm{eff}} = 3.0(3)\,J$, which is roughly half of the one extracted in the 2D experiment. This difference seems consistent with the bandwidth of the system being also twice smaller. The stronger interactions in 1D lead to slight deviations respect to the simple exponential trend even for the weakest interactions.

The heating dependence becomes nonmonotonic for higher U, as seen in the numerics and 2D experiments, but the associated features are visibly less sharp, which can be partially explained by the inhomogeneity caused by the stronger harmonic trap in this 1D case.

9.8 Summary and outlook

9.8.1 Summary

In the experiments described in this chapter we have measured heating rates and characterized their dependence for a system of ultracold bosonic atoms in an intensity-driven optical lattice. The results indicate strong evidence for a thermalization time that exponentially diverges as the frequency of the drive is increased, which is one of the main predictions of Floquet prethermalization.

The observed results also shed light into the specific mechanisms involved in Floquet prethermalization for a real physical system. The general intuition is that quantum systems driven at high frequencies can only absorb energy at very slow rates due to the need for local rearrangements of its degrees of freedom. Such rearranging processes are directly consistent with the features experimentally observed, and reflect themselves quite differently for the two phases of the model, the superfluid and the Mott insulator.

9.8.2 Outlook

The techniques described in this chapter already allow for many extensions of the present work involving the characterization of heating rates in our experimental setup. One possibility is to study the present system in the limit of hard-core bosons in 1D, where due to its proximity to integrability, different dependences are expected to

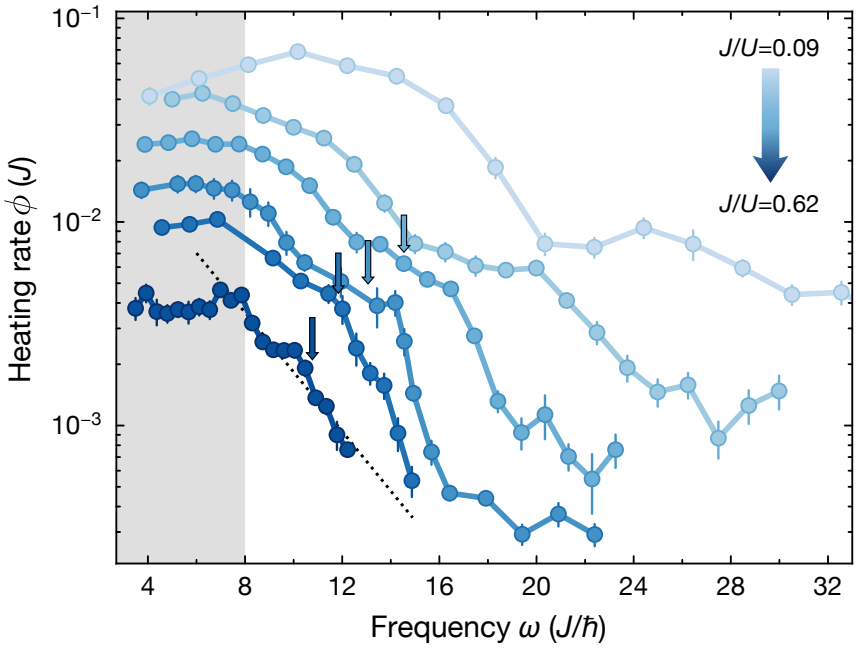

Figure 9.10: 1D experimental heating rates vs driving frequency in units of J. Measured heating rates per Floquet cycle $\phi(\omega)$, expressed in units of the tunneling strength J, for a one-dimensional system. The datasets were measured for the range of lattice depths $V_{0,x} = 3, 4, 5, 6, 7, 9\, E_r$, varying from shallow (dark blue) to deep (light blue) lattices. The corresponding values of J/U are $0.62 - 0.09$. The errorbars denote the s.e.m. We indicate the value of $\Omega_{2qp,1D}$ for the first four datasets with four small arrows. A dotted line indicates an exponential fit of the first dataset. We indicate the region below twice the non-interacting bandwidth, $\omega = 8\, J/\hbar$, by a grey shaded area.

emerge for Floquet prethermalization, as recently studied numerically [227]. Another option is to explore the dissipative response of the system in the presence of disorder, which can be realized in our system as described in Part II. This would allow for a microscopical characterization of the failure of MBL phase to thermalize in a driven system.

Further possibilites are the implementation of more exotic drives, such as quasiperiodic ones [230, 231], the use of strong drives to probe the heating in our system way beyond the linear response regime, and exploring the dependence on the temperature of the initially prepared state. Last, as we have motivated earlier, this first observation of this prethermal phenomenon (recently also observed in dipolar

spin chains [244]) paves the way for future realizations of novel prethermal phases of matter with no static analogs.

Chapter 10
Conclusion and outlook

10.1 Conclusion

In this thesis we have presented experiments performed in a two-dimensional system of ultracold bosonic atoms in optical lattices. By exploiting the tools and advantages provided by quantum-gas microscopy, we have made experimental progress into the fields of dirty bosons and out-of-equilibrium dynamics.

Introducing a projected disorder on top of our optical-lattice potentials has made it possible to directly look at glassy and localized phases. Close to equilibrium we saw signatures of the emergence of a Bose glass phase, based on site-resolved measurements and also phase coherence. Shifting away from equilibrium, we were able to probe the processes behind quantum thermalization and its breakdown in disordered systems. In particular, we have performed the first experiments of MBL in two dimensions, allowing us to estimate the position of the ergodic-MBL phase transition. These experiments represent a milestone of quantum simulation, since the exact simulation of such 2D systems still remains out of reach. In addition, we studied the delocalization processes that arise when coupling an MBL system to a quantum bath, that is a thermal system made up of few degrees of freedom. By tuning the number of particles that form the thermal component, we observed that a delocalization of the system takes place for a sufficiently large bath.

Last, we have studied periodically driven systems, by modulating the intensity of our optical lattices. Our main result has been the first experimental demonstration of the phenomenon of Floquet prethermalization. We have detected it as an exponential-in-frequency suppression of the drive-induced heating, by making use of a single-site thermometry technique. This effect remained for different interaction regimes of the model and was observed both in one and two dimensions. This prethermal behavior could open the door to new kinds of non-equilibrium phases of matter.

10.2 Outlook

Some possible future experimental directions have already been mentioned in the outlook of each experimental chapter in this thesis. In this final outlook section, we aim to focus on potential upgrades of our system, and the experiments that those could enable, as well as completely new experimental fields that go beyond the topics that have been discussed in the chapters of this thesis.

Upgrades to the system

The main technical direction currently pursued in our setup is the increase of the system size. Until now, the limitation in our cloud sizes has only been set by the confinement of the three optical lattice beams. Since these beams are used for both the physics and the imaging parts, their properties are strongly restricted by the pinning requirements during the optical-molasses imaging. The introduction of wider beams with higher powers, elliptical beams or independent lattices for dynamics and imaging are some of the ideas that will enable surpassing the current confinement. This is a particularly exciting direction for one-dimensional systems, which in our current setup are typically restricted to sizes below 20 lattice sites.

On another direction, improving the current imaging method could relax some of the conditions needed for faithful microscopy, and hence allow for bigger system sizes with the present lattice intensities. Using Raman cooling imaging [245] in a lattice, as has also been done for fermionic quantum-gas microscopes [12–14], could be very beneficial, since it would allow to work closer to the single-well ground state during the imaging. At the same time, the Raman sideband cooling process could also be useful to keep the atoms trapped and localized in experiments involving weak-intensity probing of the atoms [246]. While not described in this thesis, this imaging method has already been proven in our setup, though subsequent optimization is still required.

Another improvement of fundamental importance for quantum simulation, especially for experiments exploring long times as in this thesis, is the enhancement of the isolation of the system. In the course of this thesis, technical upgrades in the intensity stabilization of the lattices have taken the system to a next level, and the limiting heating mechanisms in the current system are believed to stem from mechanical vibrations of the optics. A precise characterization of these heating sources and the introduction of more stable optical mounts could reduce these detrimental effects further, allowing the exploration of quantum dynamics at much longer timescales.

Bose-Hubbard physics in equilibrium

The study of ground-state quantum phase transitions is at the heart of the field of quantum matter. While overcoming current finite-temperature limitations in our sys-

tem is unlikely, the constraints due to finite size and homogeneity could definitely be reduced. The technical upgrades described above, combined with the addition of repulsive barriers and deconfining potentials, would make it possible to prepare box potentials, which could allow for detailed studies of criticality [75]. A controlled tuning of the system size and the particle number could also provide insight into finite-size effects.

Bose-Hubbard physics out of equilibrium

Similar as in the equilibrium case, bigger system sizes and more homogeneous confinement would also benefit the study of dynamical quantum phase transitions. A precise characterization of the MBL-ergodic phase transition and the study of its size dependence are some of the open possibilities in 2D. In 1D, larger systems could enable more detailed studies of 1D MBL, of Heisenberg chains or the dynamical response of bosonic Luttinger liquids [247].

Additionally, many recent theoretical concepts and proposals have appeared in the out-of-equilibrium context, which make it hard to predict which new directions will be available for quantum-gas microscopes in the next few years. Some of the current trendy fields that are likely to be extensively studied in the near future are "Stark localization" [248, 249], which displays a breakdown of ergodicity in non-disordered systems under the presence of a tilted potential, quantum many-body scars [250–252] or the study of models displaying superdiffusion [253].

Experiments enabled by Rydberg atoms

A variety of experiments that has not been discussed in this thesis at all is that of Rydberg atoms, i.e. atoms in highly excited electronic states. In our setup, two-photon [78] as well as single-photon [80] excitation schemes are routinely used to, for example, probe long-range interacting systems [254] or the photoassociation of "macrodimer molecules" [255]. Many proposals involving novel out-of-equilibrium phases, such as the realization of Floquet symmetry-protected topological phases [256], could be realized in our system through chains of Rydberg-dressed atoms [89].

Going beyond these experiments, which until now were restricted to the frozen atomic limit, a major achievement would be the realization of extended Hubbard models based on Rydberg-interacting atoms tunneling in a lattice. While collective losses seem to limit such experiments, even when using off-resonant coupling to Rydberg states [257], new possibilities could be opened by considering dissipative models, based for example on the resonant excitation of macrodimers, which could enable distant hard-core interactions [258].

New directions

Aside from the routes explored in our setup so far, there is a myriad of new ideas that could be explored using some of the tools already demonstrated. One for which our setup is particularly suited is the study of collective light-matter interactions in atoms trapped tightly close to each other. Our very recent experiment [246] is a promising starting point for this direction, which could be enhanced by introducing tools like Rydberg excitation [259] or achieving the direct detection of single excitations in the cloud [78].

A related topic one could also consider is the simulation of light-emission processes using matter waves in optical lattices [260, 261]. This was recently experimentally demonstrated in a one-dimensional lattice with a single atom [262]. Our site-resolved addressing, together with the state-dependent potential explored in Ch. 7, could allow to explore similar systems in higher dimensions with well-defined initial states.

Overall, there are many exciting experiments which could be readily realized in our current setup with minor changes. However, soon-to-come upgrades could substantially push forward the possibilities for quantum-gas microscopes in the context of quantum simulation, and enable novel exotic models together with larger system sizes and longer evolution times.

Appendix A

Calculated Bose-Hubbard and band parameters

In this Appendix we present the calculated parameters, both for the Bose-Hubbard model and for the bandgaps, relevant for the experiments described in each chapter of the thesis. The calculations are based on numerics of the band structure (following the ideas described in Ch. 2). The values of the specific lattice depths V have been calibrated via lattice driving spectroscopy (see Ch. 3), and are estimated to have an uncertainty of roughly 2%.

A.1 Bose-Hubbard parameters

In this section we show different tables containing the calculated values of J and U for each of the lattice parameters used in the different experiments in this thesis.

A.1.1 Equilibrium disordered Bose-Hubbard experiments

In Ch. 4, we studied two different regimes of interactions and tunneling strengths. The first one, described in Sec. 4.3, considered the strongly interacting limit at a $V = 18\,E_r$. The second one, in Sec. 4.4, was performed at $V = 7\,E_r$.

Table A.1: Table of Bose-Hubbard parameters for the experiments in Ch. 4.

V (E_r)	J/h (Hz)	U/h (Hz)	J/U
18	7.3	658	0.01
7	80.0	363	0.22

A.1.2 MBL experiments

All the experiments on many-body localization, in both Ch. 6 and Ch. 7 were performed at the same lattice parameters of $V = 12\,E_r$.

Table A.2: Table of Bose-Hubbard parameters for the MBL experiments.

V (E_r)	J/h (Hz)	U/h (Hz)	J/U
12	24.8	602	0.04

A.1.3 Floquet experiments

Here, we show the calculated parameters for the relevant depths in the periodically driven experiments of Ch. 9. We present two different tables of parameters for the 2D and the 1D experiments. In the 2D experiment, the in-plane lattices were at the same depth and they were modulated by an amplitude $A = 0.05$ (see Tab. A.3). In the 1D case, the y-lattice was fixed to a depth of $20E_\mathrm{r}$ and the x-lattice to $V_{0,x}$ and modulated with an amplitude $A_x = 0.1$ (see Tab. A.4). We also plot the modulation of the tunneling strength δJ, defined as $\delta J = (J_{V_0-A} - J_{V_0+A})/2$.

Table A.3: Table of Bose-Hubbard parameters for the 2D Floquet experiments.

V_0 (E_r)	J/h (Hz)	U/h (Hz)	J/U	$\delta J/h$ (Hz)	$\delta J/J$
5	134.0	288	0.47	8.8	0.067
6	103.2	327	0.32	8.0	0.077
7	80.0	363	0.22	7.0	0.088
8	62.5	396	0.16	6.1	0.098
9	49.2	427	0.11	5.3	0.11
10	38.9	457	0.085	4.5	0.12
11	31.0	485	0.064	3.8	0.12

Table A.4: Table of Bose-Hubbard parameters for the 1D Floquet experiments.

$V_{0,x}$ (E_r)	J_x/h (Hz)	U/h (Hz)	J_x/U	$\delta J_x/h$ (Hz)	$\delta J_x/J_x$
3	229.1	288	0.62	18.7	0.08
4	174.9	412	0.42	18.8	0.11
5	134.0	446	0.30	17.7	0.13
6	103.2	475	0.22	16.0	0.16
7	80.0	500	0.16	14.1	0.18
9	49.2	543	0.09	10.6	0.22

A.2 Band structure

In this section we also pay attention to the higher-band structure of the system, which is important in the experiments with periodic driving.

A.2.1 Floquet experiments

As we discussed in Ch. 8, the frequencies of the drive have to be kept small enough and the amplitudes weak in order to not populate higher bands. Naively, this would only require to stay below the gap to the second excited band, $E_{g,2} = E_2(q = 0) - E_0(q = 0)$, since due to symmetry reasons there is no coupling to the first excited band with gap $E_{g,1} = E_1(q = \pi/a) - E_0(q = 0)$. Nonetheless, multiphoton resonances can trigger interband transfers even for drive frequencies well bellow the bandgaps, such that in practice one needs to identify in each regime where the onset of interband heating starts and avoid those limits. In Tab. A.5, we plot both $E_{g,1}$ and $E_{g,2}$, also obtained from numerics of the band structure, for five lattice depths within the explored range. The drive frequencies in the experiments of Ch. 9 are well below both $E_{g,1}$ and $E_{g,2}/3$.

Table A.5: Table with the bandgaps for different lattice depths.

V_0 (E_r)	$E_{g,1}/h$ (kHz)	$E_{g,1}$ (J)	$E_{g,2}/h$ (kHz)	$E_{g,2}$ (J)
3	3.9	17	9.1	40
5	5.5	41	10.6	79
7	7.1	89	12.5	156
9	8.7	176	14.7	298
11	10.1	328	16.9	544

Appendix B

Numerics for MBL simulation

In this appendix we show results obtained from an exact-diagonalization simulation of the disordered Bose-Hubbard model out of equilibrium. To perform the simulations, we use the package "QuSpin", which offers simplifies tool for the simulation of bosonic, fermionic and spin many-body systems [263].

B.1 Ladder system

Motivated to get some more insight into the observed dynamics in Ch. 7 for a dirty system, we have performed simulations of small disordered systems. Since the exact diagonalization of a reasonable size in two dimensions is extremely demanding for a Bose-Hubbard model, here we restrict ourselves to a ladder system. The simulated system consists of 5 bosons in a 2×6 lattice with periodic boundary conditions. The particles are prepared in a CDW-like pattern (see Fig. B.1).

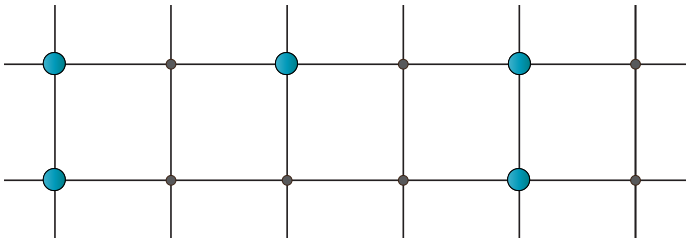

Figure B.1: Schematic of the ladder system simulated in this section. The initial density is in a CDW-like state, such that $\mathcal{I}(0) = 1$. The simulation is performed with periodic boundary conditions.

The chosen parameters for the system are taken close to the experimental ones. The quenched disorder distribution is given by a Gaussian with FWHM of $\Delta = 25\,J$ and we compare the non-interacting ($U = 0$) and a strongly interacting interacting case ($U = 25\,J$). In the non-interacting case, we see that the imbalance $\mathcal{I}$ quickly relaxes to a steady value of $\mathcal{I} \approx 0.7$, in less than $10\,\tau$ (see Fig. B.2a). In the presence of strong interactions, however, the relaxation process takes more than a $100\,\tau$, and two distinct timescales can be identified. A first one decaying to $\mathcal{I} \approx 0.6$ in less than

a tunneling time, and the second slow one reaching the value of $\mathcal{I} \approx 0.5$. Such a two-timescale slow relaxation is qualitatively similar to the experimental results in Fig. 7.5. Nonetheless, the final imbalance is way smaller in the experiment than in this small system, which is not surprising given the strong difference in dimensionality and number of particles.

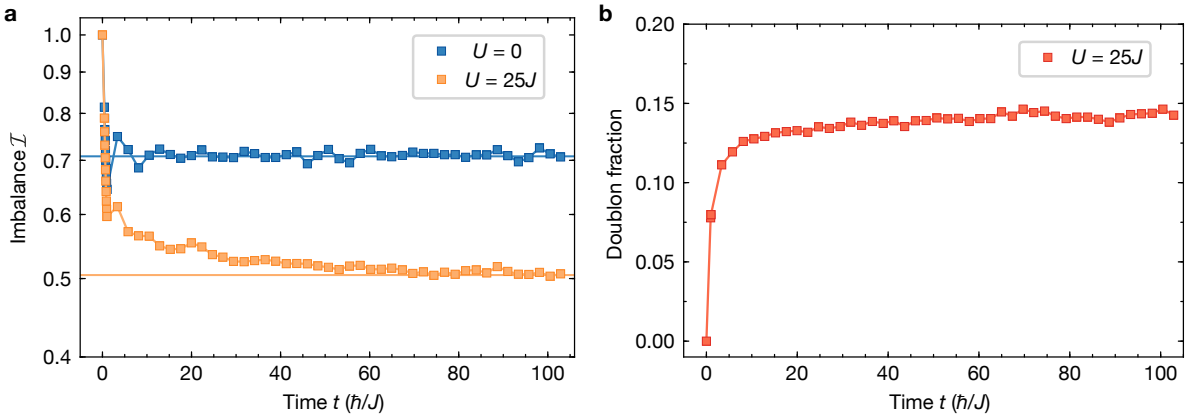

Figure B.2: Simulated imbalance and doublon dynamics for a ladder dBH system. a Imbalance dynamics for the non-interacting case ($U = 0$) and the strongly interacting one ($U = 25\,J$). **b** Doublon formation dynamics for the strongly interacting case ($U = 25\,J$).

Additionally, the simulation also allows us to study the process of doublon formation (see Fig. B.2b). We see that, as in the experiment, a quick formation of doublons takes place, and reaches a doublon fraction of $\sim 15\%$, also consistent with the experimental value.

Finally, it is worth noting that similar simulations in a purely 1D system did not show any second slow timescale, indicating the simulation of a ladder as one of the simplest models for 2D MBL.

Appendix C

Numerics on Floquet thermalization

In Ch. 9 we presented numerical results obtained from linear response theory and exact diagonalization. The results there were focused on the spectral response, and involved small system sizes ($L = 9$ sites) and weak drives. In this Appendix we show additional numerics for the driven BH model based on the Krylov subspace method for time evolution [241]. This method allows us to explore slightly bigger system sizes ($L = 12$ sites) and also stronger drives. These simulations were carried out by Matteo Ippoliti and Vedika Khemani.

C.1 The method and observables

By using the Krylov subspace method, the dynamics of a state $|\psi(t)\rangle$ at stroboscopic times $t = N_{\rm cyc}\, T$ can be simulated ($T = 2\pi/\omega$ is the drive period). We use this first to track the "energy" of the system, which we defined in relation to $\hat{H}_0$ as $E_{N_{\rm cyc}} \equiv \langle\psi(t)|\hat{H}_0|\psi(t)\rangle$. From this we can define the normalized energy density as

$$\varepsilon(N_{\rm cyc}) \equiv \frac{E_{N_{\rm cyc}} - E_0}{E_\infty - E_0}\,, \tag{C.1}$$

where $E_\infty \propto \mathrm{Tr}(\hat{H}_0)$ denotes the value of the energy at infinite temperature. In the Floquet thermalization dynamics, this will obey $0 \leq \varepsilon(N_{\rm cyc}) \leq 1$. In addition, we can also keep track of the "density of holes"

$$\rho_{\rm h}(N_{\rm cyc}) = \frac{1}{L}\sum_{i}\langle\psi((t))|\hat{\rho}_{{\rm h},i}|\psi((t))\rangle\,, \tag{C.2}$$

where $\hat{\rho}_{{\rm h},i}$ projector onto even occupation of site i, to take into account the experimental parity projection.

C.2 State preparation and dynamics

We take as initial state $|\psi(0)\rangle$ the ground state of $\hat{H}_0$ (obtained using the Lanczos method). The time evolution is then obtained by approximating each Floquet cycle by a sequence of s constant Hamiltonians, $\{\hat{H}(t = Tk/s) : k = 0, \dots s-1\}$, and time-evolve the state vector for time T/s with each of these Hamiltonians using the Krylov subspace method. In practice, using $s = 32$ steps suffices, and increasing s does not change the obtained results appreciably.

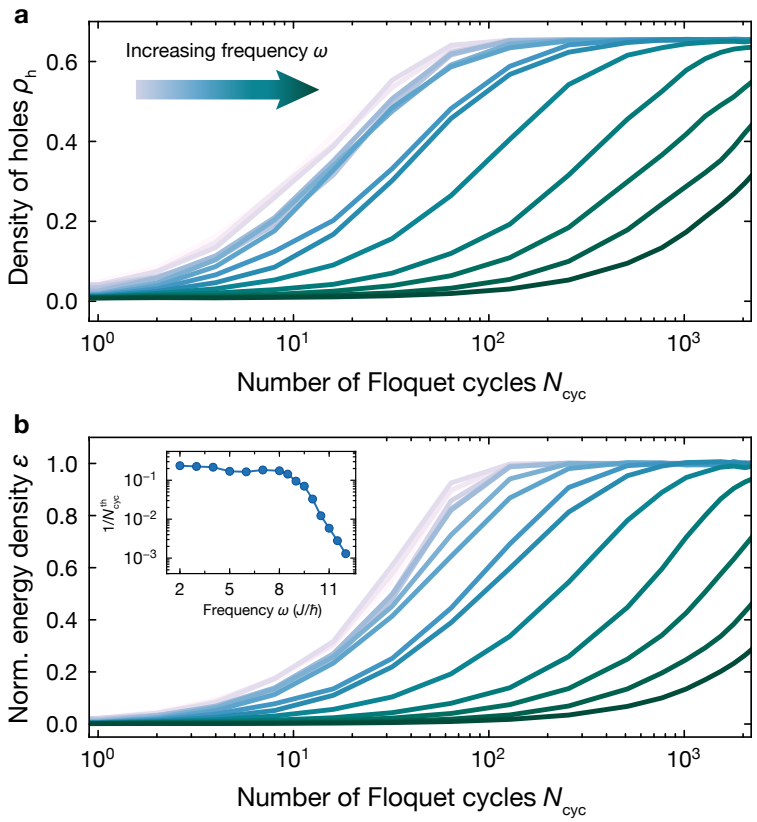

Figure C.1: Numerical simulation of Floquet thermalization. Simulation of a 1D BH chain of $L = 12$ sites at unit filling in the superfluid phase. The modulation amplitude is $g = 0.5$ and after the driving, the system is subsequently brought to the atomic limit. **a** Density of holes ρ_{h} and **b** normalized energy density ε as a function of the Floquet cycle number N_{cyc} . The results are shown for values of the drive frequency going from $\omega = 2\,J/\hbar$ (gray curves) to $\omega = 12\,J/\hbar$ (dark green curves). In the inset of **b**, the heating rate (defined as the inverse number of cycles N_{cyc} for ε to cross the threshold $\varepsilon^\star = 0.1$) is plotted against the frequency of the drive ω.

After the Floquet dynamics, we additionally "ramp" the system into the atomic-limit (a Mott insulator for zero temperature), to have a more analogous comparison with the experimental procedure. To do this, we first stop the drive and linear take $J \to 0$ in a long-enough timescale (here $\tau = 100\hbar/U$). This last evolution is also accomplished by time-evolving with piecewise constant Hamiltonians.

The simulated dynamics are shown in Fig. C.1, where we considered fairly strong amplitude of the drive $g = 0.5$ (in contrast to the weak driving in Ch. 9). The qualitative behavior of the time traces of ρ_h in Fig. C.1a, is the same as in the the experimental data in Fig. 9.3, and they also seem consistent with the dynamics of the energy density ε, plotted in Fig. C.1b.

In addition to the time evolution of ρ_h and ε, we also calculate heating rates, based on the inverse of the thermalization time $N^{\text{th}}_{\text{cyc}}$. We define $N^{\text{th}}_{\text{cyc}}$ as the number of cycles after which $\varepsilon(N_{\text{cyc}})$ surpasses some arbitrary threshold $\varepsilon^\star$ (here $\varepsilon^\star = 0.1$). This allows us to plot the dependence of the heating rate on the frequency of the drive (inset of Fig. C.1b), which can be directly compared to the results at weak drives. The results of the spectrum seem to agree with those obtained with linear response theory in the superfluid side (see Fig 9.6). The inverse of $N^{\text{th}}_{\text{cyc}}(\omega)$ remain roughly flat for $\omega \lesssim \Omega_{2\text{qp}}$, and gets exponentially suppressed above it.

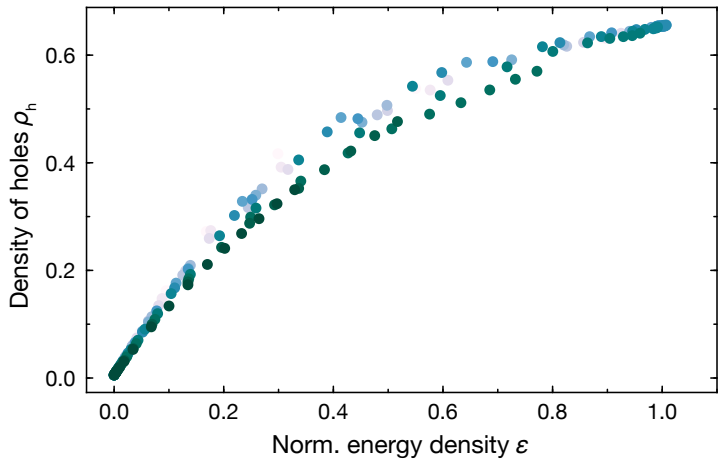

Figure C.2: Corroboration of the density of holes as a proxy for energy density. Plot of the density of holes ρ_h vs the energy density ε, from the dynamics simulated in Fig. C.1. The drive frequencies range from $\omega = 2\,J/\hbar$ (gray markers) to $\omega = 12\,J/\hbar$ (dark green markers).

Finally, to bring even further confidence into the use of ρ_h as a proxy for energy density, we directly plot these two quantities against each other in Fig. C.2. The plot

shows a similar dependence between the two variables for all driving frequencies, and one that seems roughly linear for short times (low temperatures).

More details into the numerical procedures, together with additional calculations for finite temperature can be found in the original publication [222].

Bibliography

[1] M. H. Anderson, J. R. Ensher, M. R. Matthews, C. E. Wieman, and E. A. Cornell. *Observation of Bose-Einstein condensation in a dilute atomic vapor*. Science **269**, 198–201 (1995). (Cited on page **1**)

[2] K. B. Davis, M. O. Mewes, M. R. Andrews, N. J. Van Druten, D. S. Durfee, D. M. Kurn, and W. Ketterle. *Bose-Einstein condensation in a gas of sodium atoms*. Phys. Rev. Lett. **75**, 3969–3973 (1995). (Cited on page **1**)

[3] I. Bloch, J. Dalibard, and W. Zwerger. *Many-body physics with ultracold gases*. Rev. Mod. Phys. **80**, 885–964 (2008). (Cited on pages **1** and **17**)

[4] T. Kinoshita, T. Wenger, and D. S. Weiss. *Observation of a one-dimensional Tonks-Girardeau gas*. Science **305**, 1125–1128 (2004). (Cited on page **1**)

[5] B. Paredes, A. Widera, V. Murg, O. Mandel, S. Fölling, I. Cirac, G. V. Shlyapnikov, T. W. Hansch, and I. Bloch. *Tonks-Girardeau gas of ultracold atoms in an optical lattice*. Nature **429**, 277–281 (2004). (Cited on page **1**)

[6] Z. Hadzibabic, P. Krüger, M. Cheneau, B. Battelier, and J. Dalibard. *Berezinskii-Kosterlitz-Thouless crossover in a trapped atomic gas*. Nature **441**, 1118–1121 (2006). (Cited on page **1**)

[7] M. Greiner, O. Mandel, T. Esslinger, T. Hänsch, and I. Bloch. *Quantum phase transition from a superfluid to a Mott insulator in a gas of ultracold atoms*. Nature **415**, 39–44 (2002). (Cited on pages **1** and **27**)

[8] T. Esslinger. *Fermi-Hubbard Physics with Atoms in an Optical Lattice*. Annu. Rev. Condens. Matter Phys. **1**, 129–152 (2010). (Cited on page **1**)

[9] J. F. Sherson, C. Weitenberg, M. Endres, M. Cheneau, I. Bloch, and S. Kuhr. *Single-atom-resolved fluorescence imaging of an atomic Mott insulator*. Nature **467**, 68 (2010). (Cited on pages **1**, **25**, **29**, **30**, **44**, **46**, **104**, and **108**)

[10] W. S. Bakr, A. Peng, M. E. Tai, R. Ma, J. Simon, J. I. Gillen, S. Foelling, L. Pollet, and M. Greiner. *Probing the Superfluid to Mott Insulator Transition at the Single Atom Level*. Science **329**, 547–550 (2010). (Cited on pages **1**, **25**, and **28**)

[11] E. Haller, J. Hudson, A. Kelly, D. A. Cotta, B. Peaudecerf, G. D. Bruce, and S. Kuhr. *Single-atom imaging of fermions in a quantum-gas microscope*. Nat. Phys. **11**, 738–742 (2015). (Cited on page **1**)

[12] L. W. Cheuk, M. A. Nichols, M. Okan, T. Gersdorf, V. V. Ramasesh, W. S. Bakr, T. Lompe, and M. W. Zwierlein. *Quantum-gas microscope for fermionic atoms*. Phys. Rev. Lett. **114**, 193001 (2015). (Cited on pages **1** and **120**)

[13] M. F. Parsons, F. Huber, A. Mazurenko, C. S. Chiu, W. Setiawan, K. Wooley-Brown, S. Blatt, and M. Greiner. *Site-Resolved imaging of fermionic ^{6}Li in an optical lattice*. Phys. Rev. Lett. **114**, 213002 (2015). (Cited on pages **1** and **120**)

[14] A. Omran, M. Boll, T. A. Hilker, K. Kleinlein, G. Salomon, I. Bloch, and C. Gross. *Microscopic Observation of Pauli Blocking in Degenerate Fermionic Lattice Gases*. Phys. Rev. Lett. **115**, 263001 (2015). (Cited on pages **1** and **120**)

[15] M. Endres, M. Cheneau, T. Fukuhara, C. Weitenberg, P. Schauß, C. Gross, L. Mazza, M. C. Bañuls, L. Pollet, I. Bloch, and S. Kuhr. *Observation of correlated particle-hole pairs and string order in low-dimensional Mott insulators*. Science **334**, 200–203 (2011). (Cited on page **1**)

[16] M. Boll, T. A. Hilker, G. Salomon, A. Omran, J. Nespolo, L. Pollet, I. Bloch, and C. Gross. *Spin- and density-resolved microscopy of antiferromagnetic correlations in Fermi-Hubbard chains*. Science **353**, 1257–1260 (2016). (Cited on page **1**)

[17] L. W. Cheuk, M. A. Nichols, K. R. Lawrence, M. Okan, H. Zhang, E. Khatami, N. Trivedi, T. Paiva, M. Rigol, and M. W. Zwierlein. *Observation of spatial charge and spin correlations in the 2D Fermi-Hubbard model*. Science **353**, 1260–1264 (2016). (Cited on page **1**)

[18] A. Mazurenko, C. S. Chiu, G. Ji, M. F. Parsons, M. Kanász-Nagy, R. Schmidt, F. Grusdt, E. Demler, D. Greif, and M. Greiner. *A cold-atom Fermi-Hubbard antiferromagnet*. Nature **545**, 462–466 (2017). (Cited on page **1**)

[19] I. Buluta and F. Nori. *Quantum simulators*. Science **326**, 108–111 (2009). (Cited on page **1**)

[20] I. Bloch, J. Dalibard, and S. Nascimbène. *Quantum simulations with ultracold quantum gases*. Nat. Phys. **8**, 267–276 (2012). (Cited on page **1**)

[21] C. Gross and I. Bloch. *Quantum simulations with ultracold atoms in optical lattices*. Science **357**, 995–1001 (2017). (Cited on page **1**)

[22] T. Langen, R. Geiger, and J. Schmiedmayer. *Ultracold Atoms Out of Equilibrium*. Annu. Rev. Condens. Matter Phys. **6**, 201–217 (2015). (Cited on pages **1** and **58**)

[23] M. Greiner, O. Mandel, T. W. Hänsch, and I. Bloch. *Collapse and revival of the matter wave field of a Bose-Einstein condensate*. Nature **419**, 51–54 (2002). (Cited on pages **1** and **13**)

[24] T. Kinoshita, T. Wenger, and D. S. Weiss. *A quantum Newton's cradle*. Nature **440**, 900–903 (2006). (Cited on pages **1** and **59**)

[25] L. E. Sadler, J. M. Higbie, S. R. Leslie, M. Vengalattore, and D. M. Stamper-Kurn. *Spontaneous symmetry breaking in a quenched ferromagnetic spinor Bose-Einstein condensate*. Nature **443**, 312–315 (2006). (Cited on page **1**)

[26] S. Trotzky, Y. A. Chen, A. Flesch, I. P. McCulloch, U. Schollwöck, J. Eisert, and I. Bloch. *Probing the relaxation towards equilibrium in an isolated strongly correlated one-dimensional Bose gas*. Nat. Phys. **8**, 325–330 (2012). (Cited on pages **1** and **58**)

[27] M. Gring, M. Kuhnert, T. Langen, T. Kitagawa, B. Rauer, M. Schreitl, I. Mazets, D. Adu Smith, E. Demler, and J. Schmiedmayer. *Relaxation and prethermalization in an isolated quantum system*. Science **337**, 1318–1322 (2012). (Cited on pages **1**, **59**, and **98**)

[28] F. Meinert, M. J. Mark, E. Kirilov, K. Lauber, P. Weinmann, A. J. Daley, and H. C. Nägerl. *Quantum quench in an atomic one-dimensional Ising chain*. Phys. Rev. Lett. **111**, 053003 (2013). (Cited on page **1**)

[29] S. Hild, T. Fukuhara, P. Schauß, J. Zeiher, M. Knap, E. Demler, I. Bloch, and C. Gross. *Far-from-equilibrium spin transport in Heisenberg quantum magnets*. Phys. Rev. Lett. **113**, 1–5 (2014). (Cited on page **1**)

[30] J. v. Neumann. *Beweis des Ergodensatzes und des H-Theorems in der neuen Mechanik*. Zeitschrift für Phys. **57**, 30–70 (1929). (Cited on pages **2** and **56**)

[31] A. Polkovnikov, K. Sengupta, A. Silva, and M. Vengalattore. *Colloquium: Nonequilibrium dynamics of closed interacting quantum systems*. Rev. Mod. Phys. **83**, 863–883 (2011). (Cited on pages **2**, **53**, and **56**)

[32] J. Eisert, M. Friesdorf, and C. Gogolin. *Quantum many-body systems out of equilibrium*. Nat. Phys. **11**, 124–130 (2015). (Cited on pages **2**, **53**, and **56**)

[33] L. D'Alessio, Y. Kafri, A. Polkovnikov, and M. Rigol. *From quantum chaos and eigenstate thermalization to statistical mechanics and thermodynamics*. Adv. Phys. **65**, 239–362 (2016). (Cited on pages **2**, **53**, **54**, **55**, **56**, **58**, and **61**)

[34] R. Nandkishore and D. A. Huse. *Many body localization and thermalization in quantum statistical mechanics*. Annu. Rev. Condens. Matter Phys. **6**, 15–38 (2015). (Cited on pages **2**, **56**, **60**, and **62**)

[35] J. M. Deutsch. *Quantum statistical mechanics in a closed system*. Phys. Rev. A **43**, 2046–2049 (1991). (Cited on pages **2** and **58**)

[36] M. Srednicki. *Chaos and quantum thermalization*. Phys. Rev. E **50**, 888–901 (1994). (Cited on pages **2** and **58**)

[37] H. Tasaki. *From Quantum Dynamics to the Canonical Distribution: General Picture and a Rigorous Example*. Phys. Rev. Lett. **80**, 1373–1376 (1998). (Cited on pages **2** and **58**)

[38] M. Rigol, V. Dunjko, and M. Olshanii. *Thermalization and its mechanism for generic isolated quantum systems*. Nature **452**, 854–858 (2008). (Cited on pages **2** and **58**)

[39] A. M. Kaufman, M. E. Tai, A. Lukin, M. Rispoli, R. Schittko, P. M. Preiss, and M. Greiner. *Quantum thermalization through entanglement in an isolated many-body system*. Science **353**, 794–800 (2016). (Cited on pages **2**, **29**, and **58**)

[40] P. W. Anderson. *Absence of diffusion in certain random lattices*. Phys. Rev. **109**, 1492–1505 (1958). (Cited on pages **2** and **59**)

[41] D. M. Basko, I. L. Aleiner, and B. L. Altshuler. *Metal-insulator transition in a weakly interacting many-electron system with localized single-particle states*. Ann. Phys. (Amsterdam) **321**, 1126–1205 (2006). (Cited on pages **2** and **59**)

[42] I. V. Gornyi, A. D. Mirlin, and D. G. Polyakov. *Interacting Electrons in Disordered Wires: Anderson Localization and Low-T Transport*. Phys. Rev. Lett. **95**, 206603 (2005). (Cited on pages **2** and **59**)

[43] C. D'Errico, E. Lucioni, L. Tanzi, L. Gori, G. Roux, I. P. McCulloch, T. Giamarchi, M. Inguscio, and G. Modugno. *Observation of a disordered bosonic insulator from weak to strong interactions*. Phys. Rev. Lett. **113**, 095301 (2014). (Cited on pages **2**, **42**, and **51**)

[44] M. Schreiber, S. S. Hodgman, P. Bordia, H. P. Lüschen, M. H. Fischer, R. Vosk, E. Altman, U. Schneider, and I. Bloch. *Observation of many-body localization of interacting fermions in a quasirandom optical lattice*. Science **349**, 842–845 (2015). (Cited on pages **2**, **42**, **63**, and **72**)

[45] A. Lukin, M. Rispoli, R. Schittko, M. E. Tai, A. M. Kaufman, S. Choi, V. Khemani,

J. Léonard, and M. Greiner. *Probing entanglement in a many-body-localized system*. Science **364**, 256–260 (2019). (Cited on pages **2**, **63**, **74**, and **76**)

[46] S. S. Kondov, W. R. McGehee, W. Xu, and B. Demarco. *Disorder-induced localization in a strongly correlated atomic Hubbard gas*. Phys. Rev. Lett. **114**, 083002 (2015). (Cited on pages **2**, **42**, and **63**)

[47] J.-y. Choi, S. Hild, J. Zeiher, P. Schauß, A. Rubio-Abadal, T. Yefsah, V. Khemani, D. A. Huse, I. Bloch, and C. Gross. *Exploring the many-body localization transition in two dimensions*. Science **352**, 1547–1552 (2016). (Cited on pages **2**, **33**, **36**, **63**, **64**, **69**, and **82**)

[48] P. Bordia, H. Lüschen, S. Scherg, S. Gopalakrishnan, M. Knap, U. Schneider, and I. Bloch. *Probing Slow Relaxation and Many-Body Localization in Two-Dimensional Quasiperiodic Systems*. Phys. Rev. X **7**, 41047 (2017). (Cited on pages **2**, **64**, **69**, and **72**)

[49] R. Moessner and S. Sondhi. *Equilibration and order in quantum Floquet matter*. Nat. Phys. **13**, 424–428 (2017). (Cited on pages **2**, **61**, **62**, **91**, **92**, **96**, and **97**)

[50] D. A. Abanin, W. De Roeck, and F. Huveneers. *Exponentially Slow Heating in Periodically Driven Many-Body Systems*. Phys. Rev. Lett. **115**, 1–5 (2015). (Cited on pages **2**, **99**, **103**, and **110**)

[51] T. Kuwahara, T. Mori, and K. Saito. *Floquet-Magnus theory and generic transient dynamics in periodically driven many-body quantum systems*. Ann. Phys. (N. Y). **367**, 96–124 (2016). (Cited on pages **2**, **99**, and **103**)

[52] D. Else, B. Bauer, and C. Nayak. *Prethermal Phases of Matter Protected by Time-Translation Symmetry*. Phys. Rev. X **7**, 011026 (2017). (Cited on pages **2** and **103**)

[53] *The Hubbard model at half a century*. Nat. Phys. **9**, 523 (2013). (Cited on page **9**)

[54] N. W. Ashcroft and N. D. Mermin. *Solid State Physics*. HRW international editions. Holt, Rinehart and Winston (1976). (Cited on pages **9**, **11**, and **16**)

[55] M. P. Fisher, P. B. Weichman, G. Grinstein, and D. S. Fisher. *Boson localization and the superfluid-insulator transition*. Phys. Rev. B **40**, 546–570 (1989). (Cited on pages **9**, **39**, **40**, and **41**)

[56] D. Jaksch, C. Bruder, J. I. Cirac, C. W. Gardiner, and P. Zoller. *Cold bosonic atoms in optical lattices*. Phys. Rev. Lett. **81**, 3108–3111 (1998). (Cited on pages **9** and **14**)

[57] S. Sachdev. *Quantum Phase Transitions*. Cambridge University Press, Cambridge (2011). (Cited on page **11**)

[58] F. Gerbier, A. Widera, S. Fölling, O. Mandel, T. Gericke, and I. Bloch. *Phase coherence of an atomic Mott insulator*. Phys. Rev. Lett. **95**, 1–4 (2005). (Cited on pages **12**, **27**, and **28**)

[59] M. Endres. *Probing correlated quantum many-body systems at the single-particle level*. PhD thesis, Ludwig-Maximilians-Universität München (2013). (Cited on pages **12**, **21**, **22**, **23**, and **30**)

[60] M. Inguscio and L. Fallani. *Atomic Physics: Precise Measurements and Ultracold Matter*. OUP Oxford (2013). (Cited on page **12**)

[61] S. Will, T. Best, U. Schneider, L. Hackermüller, D. S. Lühmann, and I. Bloch. *Time-resolved observation of coherent multi-body interactions in quantum phase revivals*. Nature **465**, 197–201 (2010). (Cited on page **13**)

[62] T. Hartmann, F. Keck, H. J. Korsch, and S. Mossmann. *Dynamics of Bloch oscillations*. New J. Phys. **6**, 2 (2004). (Cited on pages **14** and **35**)

[63] C. Weitenberg, M. Endres, J. F. Sherson, M. Cheneau, P. Schauß, T. Fukuhara, I. Bloch, and S. Kuhr. *Single-Spin Addressing in an Atomic Mott Insulator*. Nature **471**, 319–324 (2011). (Cited on pages **14**, **31**, and **32**)

[64] M. Karski, L. Förster, J. M. Choi, A. Steffen, W. Alt, D. Meschede, and A. Widera. *Quantum walk in position space with single optically trapped atoms*. Science **325**, 174–177 (2009). (Cited on page **14**)

[65] P. M. Preiss, R. Ma, M. E. Tai, A. Lukin, M. Rispoli, P. Zupancic, Y. Lahini, R. Islam, and M. Greiner. *Strongly correlated quantum walks in optical lattices*. Science **347**, 1229–1233 (2015). (Cited on page **14**)

[66] Z. Yan, Y. R. Zhang, M. Gong, Y. Wu, Y. Zheng, S. Li, C. Wang, F. Liang, J. Lin, Y. Xu, C. Guo, L. Sun, C. Z. Peng, K. Xia, H. Deng, H. Rong, J. Q. You, F. Nori, H. Fan, X. Zhu, and J. W. Pan. *Strongly correlated quantum walks with a 12-qubit superconducting processor*. Science **364**, 753–756 (2019). (Cited on page **14**)

[67] R. Grimm, M. Weidemüller, and Y. B. Ovchinnikov. *Optical Dipole Traps for Neutral Atoms*. Adv. At. Mol. Opt. Phys. **42**, 95–170 (2000). (Cited on page **15**)

[68] M. Greiner. *Ultracold quantum gases in three-dimensional optical lattice*. PhD thesis, Ludwig-Maximilians-Universität München (2003). (Cited on page **16**)

[69] S. Will. *From Atom Optics to Quantum Simulation*. PhD thesis, Ludwig-Maximilians-Universität München (2011). (Cited on page **16**)

[70] J. C. Slater. *A soluble problem in energy bands*. Phys. Rev. **87**, 807–835 (1952). (Cited on page **16**)

[71] T. R. Carver. *Mathieu's Functions and Electrons in a Periodic Lattice*. Am. J. Phys. **39**, 1225–1230 (1971). (Cited on page **16**)

[72] W. Kohn. *Analytic properties of Bloch waves and Wannier functions*. Phys. Rev. **115**, 809–821 (1959). (Cited on page **16**)

[73] C. Pethick and H. Smith. *Bose-Einstein Condensation in Dilute Gases*. Cambridge University Press (2002). (Cited on page **17**)

[74] M. Lewenstein, A. Sanpera, and V. Ahufinger. *Ultracold Atoms in Optical Lattices: Simulating quantum many-body systems*. OUP Oxford (2012). (Cited on page **17**)

[75] S. Wessel, F. Alet, M. Troyer, and G. G. Batrouni. *Quantum Monte Carlo simulations of confined bosonic atoms in optical lattices*. Phys. Rev. A **70**, 053615 (2004). (Cited on pages **20** and **121**)

[76] A. J. Daley. *Manipulation and Simulation of Cold Atoms in Optical Lattices*. PhD thesis, Leopold-Franzens-Universität Innsbruck (2005). (Cited on page **20**)

[77] C. Weitenberg. *Single-atom resolved imaging and manipulation in an atomic Mott insulator*. PhD thesis, Ludwig-Maximilians-Universität München (2011). (Cited on pages **21**, **22**, **25**, **30**, and **31**)

[78] P. Schauß. *High-resolution imaging of ordering in Rydberg many-body systems*. PhD thesis, Ludwig-Maximilians-Universität München (2014). (Cited on pages **21**, **24**, **25**, **26**, **35**, **121**, and **122**)

[79] S. Hild. *High-resolution imaging quantum many-body dynamics*. PhD thesis, Ludwig-Maximilians-Universität München (2016). (Cited on pages **21**, **23**, **32**, **35**, and **36**)

[80] J. Zeiher. *Realization of Rydberg-dressed quantum magnets*. PhD thesis, Ludwig-Maximilians-Universität München (2017). (Cited on pages **21** and **121**)

[81] O. Loesdau. *Aufbau und Charakterisierung eines Doppel-MOT-Systems*. Diploma thesis, Johannes-Gutenberg-Universität Mainz (2008). (Cited on page **21**)

[82] S. Hollerith. *Shaping of Optical Dipole Potentials for Ultracold 87 Rb Atoms in Optical Lattices*. Master thesis, Ludwig-Maximilians-Universität München (2016). (Cited on page **23**)

[83] E. Hecht. *Optics*. Pearson education. Addison-Wesley (2002). (Cited on page **24**)

[84] B. Zhang, J. Zerubia, and J.-C. Olivo-Marin. *Gaussian approximations of fluorescence microscope point-spread function models*. Appl. Opt. **46**, 1819–1829 (2007). (Cited on page **25**)

[85] C. Weitenberg, P. Schauß, T. Fukuhara, M. Cheneau, M. Endres, I. Bloch, and S. Kuhr. *Coherent light scattering from a two-dimensional Mott insulator*. Phys. Rev. Lett. **106**, 215301 (2011). (Cited on page **26**)

[86] P. A. Murthy, D. Kedar, T. Lompe, M. Neidig, M. G. Ries, A. N. Wenz, G. Zürn, and S. Jochim. *Matter-wave Fourier optics with a strongly interacting two-dimensional Fermi gas*. Phys. Rev. A **90**, 1–6 (2014). (Cited on page **28**)

[87] A. Rubio-Abadal, J. Y. Choi, J. Zeiher, S. Hollerith, J. Rui, I. Bloch, and C. Gross. *Many-Body Delocalization in the Presence of a Quantum Bath*. Phys. Rev. X **9**, 041014 (2019). (Cited on pages **29**, **36**, **64**, **68**, **77**, and **82**)

[88] T. Fukuhara, S. Hild, J. Zeiher, P. Schauß, I. Bloch, M. Endres, and C. Gross. *Spatially Resolved Detection of a Spin-Entanglement Wave in a Bose-Hubbard Chain*. Phys. Rev. Lett. **115**, 035302 (2015). (Cited on pages **29** and **76**)

[89] J. Zeiher, J. Y. Choi, A. Rubio-Abadal, T. Pohl, R. Van Bijnen, I. Bloch, and C. Gross. *Coherent many-body spin dynamics in a long-range interacting Ising chain*. Phys. Rev. X **7**, 041063 (2017). (Cited on pages **29** and **121**)

[90] F. Gerbier. *Boson Mott insulators at finite temperatures*. Phys. Rev. Lett. **99**, 120405 (2007). (Cited on pages **29** and **30**)

[91] L. J. Leblanc and J. H. Thywissen. *Species-specific optical lattices*. Phys. Rev. A **75**, 26–31 (2007). (Cited on page **31**)

[92] P. Zupancic, P. M. Preiss, R. Ma, A. Lukin, M. Eric Tai, M. Rispoli, R. Islam, and M. Greiner. *Ultra-precise holographic beam shaping for microscopic quantum control*. Opt. Express **24**, 13881 (2016). (Cited on page **31**)

[93] D. Bellem. *Generation of Spatially and Temporally Varying Light Potentials in Optical Lattices*. Diploma thesis, Ludwig-Maximilians-Universität München (2011). (Cited on page **32**)

[94] O. Morsch and M. Oberthaler. *Dynamics of Bose-Einstein condensates in optical lattices*. Rev. Mod. Phys. **78**, 179–215 (2006). (Cited on page **34**)

[95] S. Friebel, C. D'Andrea, J. Walz, M. Weitz, and T. W. Hänsch. *CO_2-laser optical lattice with cold rubidium atoms*. Phys. Rev. A **57**, R20–R23 (1998). (Cited on page **34**)

[96] D. Wei. *Development of a Spatially Incoherent Laser Source*. Master thesis, Technische Universität München (2019). (Cited on page **36**)

[97] A. Mosk. *Tutorial on Experimental Physics of Ultracold Gases*. In *Interacting Ultracold Gases*, M. Weidemüller and C. Zimmermann (Eds.). John Wiley & Sons, p. 215–256 (2005). (Cited on page **36**)

[98] D. Finotello, K. A. Gillis, A. Wong, and M. H. Chan. *Sharp heat-capacity signature at the superfluid transition of helium films in porous glasses*. Phys. Rev. Lett. **61**, 1954–1957 (1988). (Cited on pages **39** and **41**)

[99] T. Giamarchi and H. J. Schulz. *Localization and interaction in one-dimensional quantum fluids*. EPL **3**, 1287–1293 (1987). (Cited on page **40**)

[100] P. B. Weichman. *Dirty bosons: Twenty years later*. Mod. Phys. Lett. B **22**, 2623–2647 (2008). (Cited on page **40**)

[101] V. Gurarie, L. Pollet, N. V. Prokof'ev, B. V. Svistunov, and M. Troyer. *Phase diagram of the disordered Bose-Hubbard model*. Phys. Rev. B **80**, 214519 (2009). (Cited on pages **41** and **48**)

[102] S. G. Söyler, M. Kiselev, N. V. Prokof'ev, and B. V. Svistunov. *Phase diagram of the commensurate two-dimensional disordered Bose-Hubbard model*. Phys. Rev. Lett. **107**, 185301 (2011). (Cited on pages **41** and **48**)

[103] L. Pollet, N. V. Prokof'ev, B. V. Svistunov, and M. Troyer. *Absence of a direct superfluid to Mott insulator transition in disordered Bose systems*. Phys. Rev. Lett. **103**, 140402 (2009). (Cited on page **41**)

[104] R. B. Griffiths. *Nonanalytic Behavior above the Critical Point in a Random Ising Ferromagnet*. Phys. Rev. Lett. **23**, 17–19 (1969). (Cited on page **41**)

[105] R. Yu, L. Yin, N. S. Sullivan, J. S. Xia, C. Huan, A. Paduan-Filho, N. F. Oliveira, S. Haas, A. Steppke, C. F. Miclea, F. Weickert, R. Movshovich, E. D. Mun, B. L. Scott, V. S. Zapf, and T. Roscilde. *Bose glass and Mott glass of quasiparticles in a doped quantum magnet*. Nature **489**, 379–384 (2012). (Cited on page **41**)

[106] L. Fallani, J. E. Lye, V. Guarrera, C. Fort, and M. Inguscio. *Ultracold atoms in a disordered crystal of light: Towards a bose glass*. Phys. Rev. Lett. **98**, 130404 (2007). (Cited on pages **42** and **51**)

[107] M. Pasienski, D. McKay, M. White, and B. Demarco. *A disordered insulator in an optical lattice*. Nat. Phys. **6**, 677–680 (2010). (Cited on pages **42** and **51**)

[108] C. Meldgin, U. Ray, P. Russ, D. Chen, D. M. Ceperley, and B. DeMarco. *Probing the Bose glass-superfluid transition using quantum quenches of disorder*. Nat. Phys. **12**, 646–649 (2016). (Cited on pages **42** and **51**)

[109] J. Billy, V. Josse, Z. Zuo, A. Bernard, B. Hambrecht, P. Lugan, D. Clément, L. Sanchez-Palencia, P. Bouyer, and A. Aspect. *Direct observation of Anderson localization of matter waves in a controlled disorder*. Nature **453**, 891–894 (2008). (Cited on pages **42**, **59**, and **74**)

[110] G. Roati, C. D'Errico, L. Fallani, M. Fattori, C. Fort, M. Zaccanti, G. Modugno, M. Modugno, and M. Inguscio. *Anderson localization of a non-interacting Bose-Einstein condensate*. Nature **453**, 895–898 (2008). (Cited on page **42**)

[111] D. Clément, A. F. Varón, J. A. Retter, L. Sanchez-Palencia, A. Aspect, and P. Bouyer. *Experimental study of the transport of coherent interacting matter-waves in a 1D random potential induced by laser speckle*. New J. Phys. **8**, 165 (2006). (Cited on page **42**)

[112] L. Fallani, C. Fort, and M. Inguscio. *Bose-Einstein Condensates in Disordered Potentials*. Adv. At. Mol. Opt. Phys. **56**, 119–160 (2008). (Cited on page **42**)

[113] S. Aubry and G. André. *Analyticity breaking and Anderson localization in incommensurate lattices*. Ann. Isr. Phys. Soc. **3** (1980). (Cited on page **42**)

[114] S. Morrison, A. Kantian, A. J. Daley, H. G. Katzgraber, M. Lewenstein, H. P. Büchler, and P. Zoller. *Physical replicas and the Bose glass in cold atomic gases*. New J. Phys. **10**, 73032 (2008). (Cited on page **46**)

[115] S. J. Thomson, L. S. Walker, T. L. Harte, and G. D. Bruce. *Measuring the Edwards-Anderson order parameter of the Bose glass: A quantum gas microscope approach*. Phys. Rev. A **94**, 1–6 (2016). (Cited on pages **46** and **47**)

[116] S. F. Edwards and P. W. Anderson. *Theory of spin glasses*. J. Phys. F Met. Phys. **5**, 965–974 (1975). (Cited on pages **46** and **51**)

[117] A. Niederle and H. Rieger. *Superfluid clusters, percolation and phase transitions*

in the disordered, two-dimensional Bose-Hubbard model. New J. Phys. **15**, 075029 (2013). (Cited on page **49**)

[118] M. Yan, H. Y. Hui, and V. W. Scarola. *Dynamics of disordered states in the Bose-Hubbard model with confinement*. Phys. Rev. A **95**, 053624 (2017). (Cited on page **51**)

[119] J. Hardy, Y. Pomeau, and O. De Pazzis. *Time evolution of a two-dimensional classical lattice system*. Phys. Rev. Lett. **31**, 31, 276 (1973). (Cited on page **54**)

[120] E. Fermi, J. Pasta, and S. Ulam. *Studies of nonlinear problems*. Los Alamos, Rep. LA-1940 (1955). (Cited on page **56**)

[121] E. Altman and R. Vosk. *Universal Dynamics and Renormalization in Many-Body-Localized Systems*. Annu. Rev. Condens. Matter Phys. **6**, 383–409 (2015). (Cited on page **56**)

[122] C. Neill, P. Roushan, M. Fang, Y. Chen, M. Kolodrubetz, Z. Chen, A. Megrant, R. Barends, B. Campbell, B. Chiaro, A. Dunsworth, E. Jeffrey, J. Kelly, J. Mutus, P. J. O'Malley, C. Quintana, D. Sank, A. Vainsencher, J. Wenner, T. C. White, A. Polkovnikov, and J. M. Martinis. *Ergodic dynamics and thermalization in an isolated quantum system*. Nat. Phys. **12**, 1037–1041 (2016). (Cited on page **58**)

[123] M. Rigol, V. Dunjko, V. Yurovsky, and M. Olshanii. *Relaxation in a completely integrable many-body quantum system: An ab initio study of the dynamics of the highly excited states of 1D lattice hard-core bosons*. Phys. Rev. Lett. **98**, 050405 (2007). (Cited on page **59**)

[124] M. Rigol. *Breakdown of Thermalization in Finite One-Dimensional Systems*. Phys. Rev. Lett. **103**, 100403 (2009). (Cited on page **59**)

[125] Y. Tang, W. Kao, K.-Y. Li, S. Seo, K. Mallayya, M. Rigol, S. Gopalakrishnan, and B. L. Lev. *Thermalization near integrability in a dipolar quantum Newton's cradle*. Phys. Rev. X **8**, 21030 (2017). (Cited on page **59**)

[126] G. Roati, C. D'Errico, L. Fallani, M. Fattori, C. Fort, M. Zaccanti, G. Modugno, M. Modugno, and M. Inguscio. *Anderson localization of a non-interacting Bose-Einstein condensate*. Nature **453**, 895–898 (2008). (Cited on page **59**)

[127] T. Schwartz, G. Bartal, S. Fishman, and M. Segev. *Transport and Anderson localization in disordered two-dimensional photonic lattices*. Nature **446**, 52–55 (2007). (Cited on page **59**)

[128] R. Dalichaouch, J. P. Armstrong, S. Schultz, P. M. Platzman, and S. L. McCall. *Microwave localization by two-dimensional random scattering*. Nature **354**, 53–55 (1991). (Cited on page **59**)

[129] H. Hu, A. Strybulevych, J. H. Page, S. E. Skipetrov, and B. A. Van Tiggelen. *Localization of ultrasound in a three-dimensional elastic network*. Nat. Phys. **4**, 945–948 (2008). (Cited on page **59**)

[130] C. J. Turner, A. A. Michailidis, D. A. Abanin, M. Serbyn, and Z. Papić. *Weak ergodicity breaking from quantum many-body scars*. Nat. Phys. **14**, 745–749 (2018). (Cited on page **60**)

[131] H. Bernien, S. Schwartz, A. Keesling, H. Levine, A. Omran, H. Pichler, S. Choi, A. S. Zibrov, M. Endres, M. Greiner, V. Vuletic, and M. D. Lukin. *Probing many-body dynamics on a 51-atom quantum simulator*. Nature **551**, 579–584 (2017). (Cited on page **60**)

[132] V. Oganesyan and D. A. Huse. *Localization of interacting fermions at high temperature*. Phys. Rev. B **75**, 155111 (2007). (Cited on pages **60** and **61**)

[133] A. Pal and D. A. Huse. *Many-body localization phase transition*. Phys. Rev. B **82**, 174411 (2010). (Cited on page **60**)

[134] D. J. Luitz, N. Laflorencie, and F. Alet. *Many-body localization edge in the random-field Heisenberg chain*. Phys. Rev. B **91**, 081103(R) (2015). (Cited on page **60**)

[135] J. A. Kjäll, J. H. Bardarson, and F. Pollmann. *Many-body localization in a disordered quantum Ising chain*. Phys. Rev. Lett. **113**, 107204 (2014). (Cited on pages **60** and **61**)

[136] D. A. Huse, R. Nandkishore, V. Oganesyan, A. Pal, and S. L. Sondhi. *Localization-protected quantum order*. Phys. Rev. B **88**, 014206 (2013). (Cited on page **61**)

[137] D. Pekker, G. Refael, E. Altman, E. Demler, and V. Oganesyan. *Hilbert-glass transition: New universality of temperature-tuned many-body dynamical quantum criticality*. Phys. Rev. X **4**, 011052 (2014). (Cited on page **61**)

[138] J. Eisert, M. Cramer, and M. B. Plenio. *Colloquium: Area laws for the entanglement entropy*. Rev. Mod. Phys. **82**, 277–306 (2010). (Cited on page **61**)

[139] H. Kim and D. A. Huse. *Ballistic Spreading of Entanglement in a Diffusive Nonintegrable System*. Phys. Rev. Lett. **111**, 127205 (2013). (Cited on page **62**)

[140] J. H. Bardarson, F. Pollmann, and J. E. Moore. *Unbounded growth of entanglement in models of many-body localization*. Phys. Rev. Lett. **109**, 017202 (2012). (Cited on page **62**)

[141] J. Smith, A. Lee, P. Richerme, B. Neyenhuis, P. W. Hess, P. Hauke, M. Heyl, D. A. Huse, and C. Monroe. *Many-body localization in a quantum simulator with programmable random disorder*. Nat. Phys. **12**, 907 (2016). (Cited on pages **63** and **98**)

[142] T. Brydges, A. Elben, P. Jurcevic, B. Vermersch, C. Maier, B. P. Lanyon, P. Zoller, R. Blatt, and C. F. Roos. *Probing Rényi entanglement entropy via randomized measurements*. Science **364**, 260–263 (2019). (Cited on page **63**)

[143] P. Roushan, C. Neill, J. Tangpanitanon, V. M. Bastidas, A. Megrant, R. Barends, Y. Chen, Z. Chen, B. Chiaro, A. Dunsworth, A. Fowler, B. Foxen, M. Giustina, E. Jeffrey, J. Kelly, E. Lucero, J. Mutus, M. Neeley, C. Quintana, D. Sank, A. Vainsencher, J. Wenner, T. White, H. Neven, D. G. Angelakis, and J. Martinis. *Spectroscopic signatures of localization with interacting photons in superconducting qubits*. Science **358**, 1175–1179 (2017). (Cited on page **63**)

[144] K. Xu, J. J. Chen, Y. Zeng, Y. R. Zhang, C. Song, W. Liu, Q. Guo, P. Zhang, D. Xu, H. Deng, K. Huang, H. Wang, X. Zhu, D. Zheng, and H. Fan. *Emulating Many-Body Localization with a Superconducting Quantum Processor*. Phys. Rev. Lett. **120**, 1–6 (2018). (Cited on page **63**)

[145] B. Chiaro, C. Neill, A. Bohrdt, M. Filippone, F. Arute, K. Arya, R. Babbush, D. Bacon, J. Bardin, R. Barends, S. Boixo, D. Buell, B. Burkett, Y. Chen, Z. Chen, R. Collins, A. Dunsworth, E. Farhi, A. Fowler, B. Foxen, C. Gidney, M. Giustina, M. Harrigan, T. Huang, S. Isakov, E. Jeffrey, Z. Jiang, D. Kafri, K. Kechedzhi, J. Kelly, P. Klimov, A. Korotkov, F. Kostritsa, D. Landhuis, E. Lucero, J. McClean, X. Mi, A. Megrant, M. Mohseni, J. Mutus, M. McEwen, O. Naaman, M. Neeley, M. Niu, A. Petukhov, C. Quintana, N. Rubin, D. Sank, K. Satzinger, A. Vainsencher, T. White, Z. Yao, P. Yeh, A. Zalcman, V. Smelyanskiy, H. Neven, S. Gopalakrishnan, D. Abanin, M. Knap, J. Martinis, and P. Roushan. *Growth and preservation of entanglement in a many-body localized system*. arXiv:1910.06024 (2019). (Cited on page **63**)

[146] K. X. Wei, C. Ramanathan, and P. Cappellaro. *Exploring Localization in Nuclear Spin Chains*. Phys. Rev. Lett. **120**, 070501 (2018). (Cited on page **63**)

[147] H. P. Lüschen, P. Bordia, S. S. Hodgman, M. Schreiber, S. Sarkar, A. J. Daley, M. H. Fischer, E. Altman, I. Bloch, and U. Schneider. *Signatures of Many-Body*

Localization in a Controlled Open Quantum System. Phys. Rev. X **7**, 11034 (2017). (Cited on pages **64** and **77**)

[148] S. A. Weidinger, S. Gopalakrishnan, and M. Knap. *Self-consistent Hartree-Fock approach to many-body localization*. Phys. Rev. B **98**, 224205 (2018). (Cited on pages **65** and **72**)

[149] V. Khemani, D. N. Sheng, and D. A. Huse. *Two Universality Classes for the Many-Body Localization Transition*. Phys. Rev. Lett. **119**, 075702 (2017). (Cited on page **69**)

[150] P. Naldesi, E. Ercolessi, and T. Roscilde. *Detecting a many-body mobility edge with quantum quenches*. SciPost Phys. **1**, 010 (2016). (Cited on page **72**)

[151] Q. Guo, C. Cheng, Z.-H. Sun, Z. Song, H. Li, Z. Wang, W. Ren, H. Dong, D. Zheng, Y.-R. Zhang, R. Mondaini, H. Fan, and H. Wang. *Observation of energy resolved many-body localization*. arXiv:1912.02818 (2019). (Cited on page **72**)

[152] M. Yan, H. Y. Hui, M. Rigol, and V. W. Scarola. *Equilibration Dynamics of Strongly Interacting Bosons in 2D Lattices with Disorder*. Phys. Rev. Lett. **119**, 073002 (2017). (Cited on page **72**)

[153] T. B. Wahl, A. Pal, and S. H. Simon. *Signatures of the many-body localized regime in two dimensions*. Nat. Phys. **15**, 164–169 (2019). (Cited on page **76**)

[154] A. Geißler and G. Pupillo. *Many-body localization in the two dimensional Bose-Hubbard model*. arXiv:1909.09247 (2019). (Cited on page **76**)

[155] E. V. H. Doggen, I. V. Gornyi, A. D. Mirlin, and D. G. Polyakov. *Slow many-body delocalization beyond one dimension*. arXiv:2002.07635 (2020). (Cited on page **76**)

[156] K. Agarwal, E. Altman, E. Demler, S. Gopalakrishnan, D. A. Huse, and M. Knap. *Rare-region effects and dynamics near the many-body localization transition*. Ann. Phys. (Berlin) **529**, 1600326 (2017). (Cited on pages **77** and **88**)

[157] W. De Roeck and F. Huveneers. *Stability and instability towards delocalization in many-body localization systems*. Phys. Rev. B **95**, 155129 (2017). (Cited on pages **77** and **88**)

[158] X. Li, S. Ganeshan, J. H. Pixley, and S. Das Sarma. *Many-Body Localization and Quantum Nonergodicity in a Model with a Single-Particle Mobility Edge*. Phys. Rev. Lett. **115**, 186601 (2015). (Cited on page **77**)

[159] W. De Roeck, F. Huveneers, M. Müller, and M. Schiulaz. *Absence of Many-Body Mobility Edges*. Phys. Rev. B **93**, 014203 (2016). (Cited on page 77)

[160] H. P. Lüschen, S. Scherg, T. Kohlert, M. Schreiber, P. Bordia, X. Li, S. D. Sarma, and I. Bloch. *Exploring the Single-Particle Mobility Edge in a One-Dimensional Quasiperiodic Optical Lattice*. Phys. Rev. Lett. **120**, 160404 (2018). (Cited on page 77)

[161] T. Kohlert, S. Scherg, X. Li, H. P. Lüschen, S. Das Sarma, I. Bloch, and M. Aidelsburger. *Observation of Many-Body Localization in a One-Dimensional System with a Single-Particle Mobility Edge*. Phys. Rev. Lett. **122**, 170403 (2019). (Cited on page 77)

[162] R. Nandkishore, S. Gopalakrishnan, and D. A. Huse. *Spectral Features of a Many-Body-Localized System Weakly Coupled to a Bath*. Phys. Rev. B **90**, 064203 (2014). (Cited on page 77)

[163] S. Johri, R. Nandkishore, and R. N. Bhatt. *Many-Body Localization in Imperfectly Isolated Quantum Systems*. Phys. Rev. Lett. **114**, 117401 (2015). (Cited on page 77)

[164] E. Levi, M. Heyl, I. Lesanovsky, and J. P. Garrahan. *Robustness of Many-Body Localization in the Presence of Dissipation*. Phys. Rev. Lett. **116**, 237203 (2016). (Cited on page 77)

[165] M. H. Fischer, M. Maksymenko, and E. Altman. *Dynamics of a Many-Body-Localized System Coupled to a Bath*. Phys. Rev. Lett. **116**, 160401 (2016). (Cited on page 77)

[166] R. Nandkishore. *Many-body localization proximity effect*. Phys. Rev. B **92**, 245141 (2015). (Cited on pages 78, 85, and 88)

[167] K. Hyatt, J. R. Garrison, A. C. Potter, and B. Bauer. *Many-body localization in the presence of a small bath*. Phys. Rev. B **95**, 035132 (2017). (Cited on pages 78, 85, and 88)

[168] J. Marino and R. M. Nandkishore. *Many-body localization proximity effects in platforms of coupled spins and bosons*. Phys. Rev. B **97**, 054201 (2018). (Cited on page 78)

[169] U. Gavish and Y. Castin. *Matterwave localization in disordered cold atom lattices*. Phys. Rev. Lett. **95**, 020401 (2005). (Cited on page 88)

[170] B. Gadway, D. Pertot, J. Reeves, M. Vogt, and D. Schneble. *Glassy behavior in a*

binary atomic mixture. Phys. Rev. Lett. **107**, 1–5 (2011). (Cited on page **88**)

[171] G. Floquet. *Sur les équations différentielles linéaires à coefficients périodiques*. Ann. Sci. l'École Norm. supérieure **12**, 47–88 (1883). (Cited on page **91**)

[172] P. Kapitza. *Dynamics stability of a pendulum with vibrating suspension point*. Sov. Phys. - JETP **21**, 588–597 (1951). (Cited on page **91**)

[173] D. H. Dunlap and V. M. Kenkre. *Dynamic localization of a charged particle moving under the influence of an electric field*. Phys. Rev. B **34**, 3625–3633 (1986). (Cited on page **91**)

[174] A. Eckardt. *Colloquium: Atomic quantum gases in periodically driven optical lattices*. Rev. Mod. Phys. **89**, 1–30 (2017). (Cited on pages **91** and **92**)

[175] T. Oka and S. Kitamura. *Floquet Engineering of Quantum Materials*. Annu. Rev. Condens. Matter Phys. **10**, 387–408 (2019). (Cited on page **91**)

[176] F. Harper, R. Roy, M. S. Rudner, and S. Sondhi. *Topology and Broken Symmetry in Floquet Systems*. Annu. Rev. Condens. Matter Phys. **11** (2020). (Cited on page **91**)

[177] M. Bukov, L. D'Alessio, and A. Polkovnikov. *Universal high-frequency behavior of periodically driven systems: From dynamical stabilization to Floquet engineering*. Adv. Phys. **64**, 139–226 (2015). (Cited on pages **91** and **94**)

[178] K. W. Madison, M. C. Fischer, R. B. Diener, Q. Niu, and M. G. Raizen. *Dynamical Bloch band suppression in an optical lattice*. Phys. Rev. Lett. **81**, 5093–5096 (1998). (Cited on page **92**)

[179] H. Lignier, C. Sias, D. Ciampini, Y. Singh, A. Zenesini, O. Morsch, and E. Arimondo. *Dynamical control of matter-wave tunneling in periodic potentials*. Phys. Rev. Lett. **99**, 220403 (2007). (Cited on pages **92** and **104**)

[180] A. Eckardt, M. Holthaus, H. Lignier, A. Zenesini, D. Ciampini, O. Morsch, and E. Arimondo. *Exploring dynamic localization with a Bose-Einstein condensate*. Phys. Rev. A **79**, 1–7 (2009). (Cited on page **92**)

[181] J. Struck, C. Ölschläger, M. Weinberg, P. Hauke, J. Simonet, A. Eckardt, M. Lewenstein, K. Sengstock, and P. Windpassinger. *Tunable gauge potential for neutral and spinless particles in driven optical lattices*. Phys. Rev. Lett. **108**, 1–5 (2012). (Cited on page **92**)

[182] M. Aidelsburger, M. Atala, M. Lohse, J. T. Barreiro, B. Paredes, and I. Bloch.

Realization of the Hofstadter hamiltonian with ultracold atoms in optical lattices. Phys. Rev. Lett. **111**, 1–5 (2013). (Cited on page **92**)

[183] G. Jotzu, M. Messer, R. Desbuquois, M. Lebrat, T. Uehlinger, D. Greif, and T. Esslinger. *Experimental realization of the topological Haldane model with ultracold fermions*. Nature **515**, 237–240 (2014). (Cited on page **92**)

[184] J. Struck, C. Ölschläger, R. Le Targat, P. Soltan-Panahi, A. Eckardt, M. Lewenstein, P. Windpassinger, and K. Sengstock. *Quantum simulation of frustrated classical magnetism in triangular optical lattices*. Science **333**, 996–999 (2011). (Cited on page **92**)

[185] J. Cayssol, B. Dóra, F. Simon, and R. Moessner. *Floquet topological insulators*. Phys. Status Solidi - Rapid Res. Lett. **7**, 101–108 (2013). (Cited on page **92**)

[186] N. H. Lindner, G. Refael, and V. Galitski. *Floquet topological insulator in semiconductor quantum wells*. Nat. Phys. **7**, 490–495 (2011). (Cited on page **92**)

[187] Y. H. Wang, H. Steinberg, P. Jarillo-Herrero, and N. Gedik. *Observation of Floquet-Bloch states on the surface of a topological insulator*. Science **342**, 453–457 (2013). (Cited on page **92**)

[188] V. Khemani, A. Lazarides, R. Moessner, and S. L. Sondhi. *Phase Structure of Driven Quantum Systems*. Phys. Rev. Lett. **116**, 1–5 (2016). (Cited on pages **92** and **97**)

[189] C. W. Von Keyserlingk, V. Khemani, and S. L. Sondhi. *Absolute stability and spatiotemporal long-range order in Floquet systems*. Phys. Rev. B **94**, 1–11 (2016). (Cited on pages **92** and **97**)

[190] D. V. Else, B. Bauer, and C. Nayak. *Floquet Time Crystals*. Phys. Rev. Lett. **117**, 1–5 (2016). (Cited on pages **92** and **97**)

[191] N. Y. Yao, A. C. Potter, I. D. Potirniche, and A. Vishwanath. *Discrete Time Crystals: Rigidity, Criticality, and Realizations*. Phys. Rev. Lett. **118**, 1–6 (2017). (Cited on pages **92** and **97**)

[192] S. Choi, J. Choi, R. Landig, G. Kucsko, H. Zhou, J. Isoya, F. Jelezko, S. Onoda, H. Sumiya, V. Khemani, C. Von Keyserlingk, N. Y. Yao, E. Demler, and M. D. Lukin. *Observation of discrete time-crystalline order in a disordered dipolar many-body system*. Nature **543**, 221–225 (2017). (Cited on pages **92** and **97**)

[193] J. Zhang, P. W. Hess, A. Kyprianidis, P. Becker, A. Lee, J. Smith, G. Pagano, I. D.

Potirniche, A. C. Potter, A. Vishwanath, N. Y. Yao, and C. Monroe. *Observation of a discrete time crystal*. Nature **543**, 217–220 (2017). (Cited on pages **92** and **97**)

[194] K. Sacha and J. Zakrzewski. *Time crystals: a review*. Rep. Prog. Phys. **81**, 016401 (2018). (Cited on page **92**)

[195] D. V. Else, C. Monroe, C. Nayak, and N. Y. Yao. *Discrete Time Crystals*. arXiv:1905.13232 (2019). (Cited on page **92**)

[196] V. Khemani, R. Moessner, and S. Sondhi. *A Brief History of Time Crystals*. arXiv:1910.10745 (2019). (Cited on pages **92** and **97**)

[197] N. Y. Yao and C. Nayak. *Time crystals in periodically driven systems*. Phys. Today **71**, 40–47 (2018). (Cited on page **92**)

[198] M. S. Rudner, N. H. Lindner, E. Berg, and M. Levin. *Anomalous Edge States and the Bulk-Edge Correspondence for Periodically Driven Two-Dimensional Systems*. Phys. Rev. X **3**, 031005 (2013). (Cited on page **92**)

[199] P. Titum, E. Berg, M. Rudner, G. Refael, and N. Lindner. *Anomalous Floquet-Anderson Insulator as a Nonadiabatic Quantized Charge Pump*. Phys. Rev. X **6**, 021013 (2016). (Cited on page **92**)

[200] F. Nathan, D. Abanin, E. Berg, N. Lindner, and M. Rudner. *Anomalous Floquet insulators*. Phys. Rev. B **99**, 195133 (2019). (Cited on page **92**)

[201] S. Blanes, F. Casas, J. A. Oteo, and J. Ros. *The Magnus expansion and some of its applications*. Phys. Rep. **470**, 151–238 (2009). (Cited on page **94**)

[202] W. Magnus. *On the exponential solution of differential equations for a linear operator*. Commun. Pure Appl. Math. **7**, 649–673 (1954). (Cited on page **94**)

[203] A. Lazarides, A. Das, and R. Moessner. *Periodic thermodynamics of isolated quantum systems*. Phys. Rev. Lett. **112**, 150401 (2014). (Cited on page **97**)

[204] A. Lazarides, A. Das, and R. Moessner. *Equilibrium states of generic quantum systems subject to periodic driving*. Phys. Rev. E **90**, 012110 (2014). (Cited on page **97**)

[205] V. Gritsev and A. Polkovnikov. *Integrable Floquet dynamics*. SciPost Phys. **2**, 21 (2017). (Cited on page **97**)

[206] A. Lazarides, A. Das, and R. Moessner. *Fate of Many-Body Localization Under Periodic Driving*. Phys. Rev. Lett. **115**, 030402 (2015). (Cited on pages **97** and **103**)

[207] P. Ponte, Z. Papić, F. Huveneers, and D. A. Abanin. *Many-Body Localization in Periodically Driven Systems*. Phys. Rev. Lett. **114**, 140401 (2015). (Cited on pages **97** and **103**)

[208] P. Ponte, A. Chandran, Z. Papic, and D. A. Abanin. *Periodically driven ergodic and many-body localized quantum systems*. Ann. Phys. (Amsterdam) **353**, 196 – 204 (2015). (Cited on pages **97** and **103**)

[209] D. A. Abanin, W. De Roeck, and F. Huveneers. *Theory of many-body localization in periodically driven systems*. Ann. Phys. (Amsterdam) **372**, 1–11 (2016). (Cited on pages **97** and **103**)

[210] P. Bordia, H. Lüschen, U. Schneider, M. Knap, and I. Bloch. *Periodically driving a many-body localized quantum system*. Nat. Phys. **13**, 460 (2017). (Cited on pages **97** and **103**)

[211] G. Kucsko, S. Choi, J. Choi, P. C. Maurer, H. Zhou, R. Landig, H. Sumiya, S. Onoda, J. Isoya, F. Jelezko, E. Demler, N. Y. Yao, and M. D. Lukin. *Critical Thermalization of a Disordered Dipolar Spin System in Diamond*. Phys. Rev. Lett. **121**, 023601 (2018). (Cited on page **98**)

[212] T. Mori, T. N. Ikeda, E. Kaminishi, and M. Ueda. *Thermalization and prethermalization in isolated quantum systems: A theoretical overview*. J. Phys. B At. Mol. Opt. Phys. **51**, 112001 (2018). (Cited on page **98**)

[213] J. Berges, S. Borsányi, and C. Wetterich. *Prethermalization*. Phys. Rev. Lett. **93**, 142002 (2004). (Cited on page **98**)

[214] K. Mallayya, M. Rigol, and W. De Roeck. *Prethermalization and Thermalization in Isolated Quantum Systems*. Phys. Rev. X **9**, 021027 (2019). (Cited on page **98**)

[215] L. D'Alessio and M. Rigol. *Long-time Behavior of Isolated Periodically Driven Interacting Lattice Systems*. Phys. Rev. X **4**, 041048 (2014). (Cited on pages **98** and **103**)

[216] D. A. Abanin, W. De Roeck, W. W. Ho, and F. Huveneers. *Effective Hamiltonians, prethermalization, and slow energy absorption in periodically driven many-body systems*. Phys. Rev. B **95**, 1–8 (2017). (Cited on pages **99** and **103**)

[217] D. Abanin, W. De Roeck, W. W. Ho, and F. Huveneers. *A Rigorous Theory of Many-Body Prethermalization for Periodically Driven and Closed Quantum Systems*. Commun. Math. Phys. **354**, 809–827 (2017). (Cited on pages **99** and **103**)

[218] T. Mori, T. Kuwahara, and K. Saito. *Rigorous Bound on Energy Absorption and*

Generic Relaxation in Periodically Driven Quantum Systems. Phys. Rev. Lett. **116**, 1–5 (2016). (Cited on pages **99** and **103**)

[219] A. Eckardt and E. Anisimovas. *High-frequency approximation for periodically driven quantum systems from a Floquet-space perspective*. New J. Phys. **17**, 93039 (2015). (Cited on page **99**)

[220] N. Strohmaier, D. Greif, R. Jördens, L. Tarruell, H. Moritz, T. Esslinger, R. Sensarma, D. Pekker, E. Altman, and E. Demler. *Observation of elastic doublon decay in the Fermi-hubbard model*. Phys. Rev. Lett. **104**, 1–4 (2010). (Cited on page **100**)

[221] G. Sun and A. Eckardt. *Optimal frequency window for Floquet engineering in optical lattices*. Phys. Rev. Res. **2**, 013241 (2020). (Cited on pages **101** and **106**)

[222] A. Rubio-Abadal, M. Ippoliti, S. Hollerith, D. Wei, J. Rui, S. L. Sondhi, V. Khemani, C. Gross, and I. Bloch. *Floquet Prethermalization in a Bose-Hubbard System*. Phys. Rev. X **10**, 021044 (2020). (Cited on pages **103**, **110**, **112**, and **132**)

[223] M. Bukov, S. Gopalakrishnan, M. Knap, and E. Demler. *Prethermal Floquet Steady States and Instabilities in the Periodically Driven, Weakly Interacting Bose-Hubbard Model*. Phys. Rev. Lett. **115**, 205301 (2015). (Cited on pages **103** and **113**)

[224] F. Machado, G. D. Kahanamoku-Meyer, D. V. Else, C. Nayak, and N. Y. Yao. *Exponentially slow heating in short and long-range interacting Floquet systems*. Phys. Rev. Res. **1** (2019). (Cited on page **103**)

[225] S. Vajna, K. Klobas, T. Prosen, and A. Polkovnikov. *Replica Resummation of the Baker-Campbell-Hausdorff Series*. Phys. Rev. Lett. **120**, 200607 (2018). (Cited on page **103**)

[226] D. J. Luitz, R. Moessner, S. L. Sondhi, and V. Khemani. *Prethermalization without Temperature*. Phys. Rev. X **10**, 021046 (2020). (Cited on page **103**)

[227] K. Mallayya and M. Rigol. *Heating rates in periodically driven strongly interacting quantum many-body systems*. Phys. Rev. Lett. **123**, 240603 (2019). (Cited on pages **103** and **117**)

[228] A. Haldar, R. Moessner, and A. Das. *Onset of Floquet thermalization*. Phys. Rev. B **97**, 1–8 (2018). (Cited on page **103**)

[229] O. Howell, P. Weinberg, D. Sels, A. Polkovnikov, and M. Bukov. *Asymptotic Prethermalization in Periodically Driven Classical Spin Chains*. Phys. Rev. Lett. **122**, 10602 (2019). (Cited on page **103**)

[230] D. V. Else, W. W. Ho, and P. T. Dumitrescu. *Long-Lived Interacting Phases of Matter Protected by Multiple Time-Translation Symmetries in Quasiperiodically Driven Systems*. Phys. Rev. X **10**, 021032 (2020). (Cited on pages **103** and **117**)

[231] W. De Roeck and V. Verreet. *Very slow heating for weakly driven quantum many-body systems*. arXiv:1911.01998 (2019). (Cited on pages **103** and **117**)

[232] G. Jotzu, M. Messer, F. Görg, D. Greif, R. Desbuquois, and T. Esslinger. *Creating State-Dependent Lattices for Ultracold Fermions by Magnetic Gradient Modulation*. Phys. Rev. Lett. **115**, 073002 (2015). (Cited on page **104**)

[233] M. Reitter, J. Näger, K. Wintersperger, C. Sträter, I. Bloch, A. Eckardt, and U. Schneider. *Interaction Dependent Heating and Atom Loss in a Periodically Driven Optical Lattice*. Phys. Rev. Lett. **119**, 200402 (2017). (Cited on page **104**)

[234] M. Messer, K. Sandholzer, F. Görg, J. Minguzzi, R. Desbuquois, and T. Esslinger. *Floquet Dynamics in Driven Fermi-Hubbard Systems*. Phys. Rev. Lett. **121**, 1–6 (2018). (Cited on page **104**)

[235] T. Boulier, J. Maslek, M. Bukov, C. Bracamontes, E. Magnan, S. Lellouch, E. Demler, N. Goldman, and J. V. Porto. *Parametric Heating in a 2D Periodically Driven Bosonic System: Beyond the Weakly Interacting Regime*. Phys. Rev. X **9**, 11047 (2019). (Cited on pages **104** and **109**)

[236] K. Wintersperger, M. Bukov, J. Näger, S. Lellouch, E. Demler, U. Schneider, I. Bloch, N. Goldman, and M. Aidelsburger. *Parametric Instabilities of Interacting Bosons in Periodically Driven 1D Optical Lattices*. Phys. Rev. X **10**, 011030 (2020). (Cited on pages **104** and **109**)

[237] K. Singh, C. J. Fujiwara, Z. A. Geiger, E. Q. Simmons, M. Lipatov, A. Cao, P. Dotti, S. V. Rajagopal, R. Senaratne, T. Shimasaki, M. Heyl, A. Eckardt, and D. M. Weld. *Quantifying and Controlling Prethermal Nonergodicity in Interacting Floquet Matter*. Phys. Rev. X **9**, 041021 (2019). (Cited on page **104**)

[238] T. Stöferle, H. Moritz, C. Schori, M. Köhl, and T. Esslinger. *Transition from a strongly interacting 1D superfluid to a Mott insulator*. Phys. Rev. Lett. **92**, 1–4 (2004). (Cited on page **106**)

[239] M. Endres, T. Fukuhara, D. Pekker, M. Cheneau, P. Schauß, C. Gross, E. Demler, S. Kuhr, and I. Bloch. *The 'Higgs' amplitude mode at the two-dimensional superfluid/Mott insulator transition*. Nature **487**, 454–458 (2012). (Cited on pages **106** and **108**)

[240] M. Weinberg, C. Ölschläger, C. Sträter, S. Prelle, A. Eckardt, K. Sengstock, and J. Simonet. *Multiphoton interband excitations of quantum gases in driven optical lattices*. Phys. Rev. A **92**, 43621 (2015). (Cited on page **106**)

[241] S. R. Manmana, A. Muramatsu, and R. M. Noack. *Time evolution of one-dimensional Quantum Many Body Systems*. AIP Conference Proceedings **789**, 269–278 (2005). (Cited on pages **107** and **129**)

[242] B. Capogrosso-Sansone, S. G. Söyler, N. Prokof'ev, and B. Svistunov. *Monte Carlo study of the two-dimensional Bose-Hubbard model*. Phys. Rev. A **77**, 015602 (2008). (Cited on page **113**)

[243] S. D. Huber, B. Theiler, E. Altman, and G. Blatter. *Amplitude mode in the quantum phase model*. Phys. Rev. Lett. **100**, 1–4 (2008). (Cited on page **113**)

[244] P. Peng, C. Yin, X. Huang, C. Ramanathan, and P. Cappellaro. *Observation of Floquet prethermalization in dipolar spin chains*. arXiv:1912.05799 (2019). (Cited on page **118**)

[245] B. J. Lester, A. M. Kaufman, and C. A. Regal. *Raman cooling imaging: Detecting single atoms near their ground state of motion*. Phys. Rev. A **90**, 011804 (2014). (Cited on page **120**)

[246] J. Rui, D. Wei, A. Rubio-Abadal, S. Hollerith, J. Zeiher, D. M. Stamper-Kurn, C. Gross, and I. Bloch. *A subradiant optical mirror formed by a single structured atomic layer*. arXiv:2001.00795 (2020). (Cited on pages **120** and **122**)

[247] R. Citro, E. Demler, T. Giamarchi, M. Knap, and E. Orignac. *Lattice modulation spectroscopy of one-dimensional quantum gases:Universal scaling of the absorbed energy*. arXiv:2003.05373 (2020). (Cited on page **121**)

[248] M. Schulz, C. A. Hooley, R. Moessner, and F. Pollmann. *Stark Many-Body Localization*. Phys. Rev. Lett. **122**, 040606 (2019). (Cited on page **121**)

[249] E. Van Nieuwenburg, Y. Baum, and G. Refael. *From Bloch oscillations to many-body localization in clean interacting systems*. Proc. Natl. Acad. Sci. **116**, 9269–9274 (2019). (Cited on page **121**)

[250] A. Hudomal, I. Vasić, N. Regnault, and Z. Papić. *Quantum scars of bosons with correlated hopping*. Commun. Phys. **3**, 99 (2020). (Cited on page **121**)

[251] H. Zhao, J. Vovrosh, F. Mintert, and J. Knolle. *Quantum Many-Body Scars in Optical Lattices*. Phys. Rev. Lett. **124**, 160604 (2020). (Cited on page **121**)

[252] W. Kao, K.-Y. Li, K.-Y. Lin, S. Gopalakrishnan, and B. L. Lev. *Creating quantum many-body scars through topological pumping of a 1D dipolar gas*. arXiv:2002.10475 (2020). (Cited on page **121**)

[253] E. Ilievski, J. De Nardis, M. Medenjak, and T. Prosen. *Superdiffusion in One-Dimensional Quantum Lattice Models*. Phys. Rev. Lett. **121**, 230602 (2018). (Cited on page **121**)

[254] P. Schauß, M. Cheneau, M. Endres, T. Fukuhara, S. Hild, A. Omran, T. Pohl, C. Gross, S. Kuhr, and I. Bloch. *Observation of spatially ordered structures in a two-dimensional Rydberg gas*. Nature **491**, 87–91 (2012). (Cited on page **121**)

[255] S. Hollerith, J. Zeiher, J. Rui, A. Rubio-Abadal, V. Walther, T. Pohl, D. M. Stamper-Kurn, I. Bloch, and C. Gross. *Quantum gas microscopy of Rydberg macrodimers*. Science **364**, 664–667 (2019). (Cited on page **121**)

[256] I. D. Potirniche, A. C. Potter, M. Schleier-Smith, A. Vishwanath, and N. Y. Yao. *Floquet Symmetry-Protected Topological Phases in Cold-Atom Systems*. Phys. Rev. Lett. **119**, 123601 (2017). (Cited on page **121**)

[257] J. Zeiher, R. Van Bijnen, P. Schauß, S. Hild, J. Y. Choi, T. Pohl, I. Bloch, and C. Gross. *Many-body interferometry of a Rydberg-dressed spin lattice*. Nat. Phys. **12**, 1095–1099 (2016). (Cited on page **121**)

[258] C. Ates, B. Olmos, W. Li, and I. Lesanovsky. *Dissipative binding of lattice bosons through distance-selective pair loss*. Phys. Rev. Lett. **109**, 233003 (2012). (Cited on page **121**)

[259] R. Bekenstein, I. Pikovski, H. Pichler, E. Shahmoon, S. F. Yelin, and M. D. Lukin. *Quantum metasurfaces with atom arrays*. Nat. Phys. p. 1–6 (2020). (Cited on page **122**)

[260] I. De Vega, D. Porras, and J. Ignacio Cirac. *Matter-wave emission in optical lattices: Single particle and collective effects*. Phys. Rev. Lett. **101**, 260404 (2008). (Cited on page **122**)

[261] C. Navarrete-Benlloch, I. De Vega, D. Porras, and J. I. Cirac. *Simulating quantum-optical phenomena with cold atoms in optical lattices*. New J. Phys. **13**, 23024 (2011). (Cited on page **122**)

[262] L. Krinner, M. Stewart, A. Pazmiño, J. Kwon, and D. Schneble. *Spontaneous emission of matter waves from a tunable open quantum system*. Nature **559**, 589–592 (2018). (Cited on page **122**)

[263] P. Weinberg and M. Bukov. *QuSpin: a Python package for dynamics and exact diagonalisation of quantum many body systems part I: spin chains*. SciPost Phys **2**, 003 (2017). (Cited on page **127**)

Acknowledgments

It has been roughly 4 and a 1/2 years since I crossed the *Bodensee* to start working in MPQ. Over this time in Munich and Garching I have gone through burning devices, water inundations and unexpected pandemics, all of which required the knowledge, support and company of a diverse range of great people that I want to thank.

In the first place I would like to thank my supervisor, Immanuel Bloch, for giving me the opportunity of working in this exciting field. His contagious passion for optical lattices was what brought me to MPQ, and he welcomed me in the *single atoms* team despite my little previous experience in laser experiments. His interest when hearing about new results and his ability to bring highly talented scientists to collaborate with us have been key to the success of our experiments. I also want to thank him for ensuring the funding of the lab, allowing for summer schools, workshops, and quick surprise reparations. Finally, I have also benefited from his impulse for sports, leading me through the *Englischer Garten* to probably the longest runs of my life.

I am also very grateful to Christian Gross for the direct supervision and management of the lab. Christian efficiently kept the labwork flowing, either by bringing up solutions to technical problems or by suggesting an idea for the next measurement. He always brought a positive mood to our meetings and many new ways to improve the setup or our internal communication. Even after moving to Tübingen, his assistance and discussions have remained vital towards the end of my PhD.

Without a doubt, I am mostly indebted to all the members of the *single atoms lab* with whom I have worked over these years. I want to start (in chronological order) by thanking Sebastian Hild, who took a lot of time and patience to help me in the basics of MPQ and explaining me many details of the lab. Aside from the work in the lab, he introduced me to many members of MPQ and LMU and helped me feel welcomed in Munich through hiking and bouldering. At that time, Tarik Yefsah was also fundamental in my initial knowledge process and for the upgrade of our vertical lattice. I learned a lot about optics and rotating condensates with him. After beginning, I spent much time working with Jae-yoon Choi, whose ideas and previous experiments are at the heart of the second part of this thesis. I learned how to run the experiment with him, as well as many of the basic ideas surrounding many-body localization.

Over most of my time as a PhD, I was blessed to work with Johannes Zeiher. From him I learned the most about the setup, and he was the person to go to with my

technical and scientific doubts. I enjoyed a lot our discussions on a range of physical phenomena, many of them while going back to Munich (while I still lived there), or while having a beer. Simon Hollerith is definitely the team member with whom I have spent the most time both inside and outside MPQ: From the first day, building a new breadboard in the preplab, to these last months, giving me most of the feedback for this thesis. I have profited from many discussions about the lab, physics in general, music, climate change or our views on capitalism. I also enjoyed many nice times in Freising, Garching or Munich. Around the middle of my PhD, Jun Rui arrived as a postdoc, from whom I learned a lot of atomic physics, due to his extensive knowledge on all the parts of a cold-atom setup. He was essential in getting the system back to work after the "rain in the lab" and his constant motivation has pushed us to bring the system forward. We have had many stimulating discussions comparing our cultures, and he made my visit to Shanghai possible.

Getting towards the end of my thesis, it was a pleasure to work with David Wei during his Master thesis and now as a PhD student. His critical questions while discussing technical and physical topics, made me think twice about points I believed I had understood. He has also been a motivation for me to improve my coding skills. Very recently Kritsana (Cake) Srakaew also joined our team. His questions, suggestions and feedback during this last year has been very important for me. I wish this new generation of PhD students a lot of success in the months/years to come! I also thank Simon Evered, particularly for his overseas proofreading of my thesis.

Aside from experimental efforts, this thesis has benefited from collaborations with theory colleagues. The second part of the dissertation has benefited a lot from discussions with David Huse, who was directly involved in the first MBL experiment in our lab. The third part of the thesis has been the result of a fruitful collaboration with Vedika Khemani, Matteo Ippoliti and Shivaji Sondhi from Stanford and Princeton universities. I am particularly grateful to Vedika, who triggered and pushed the project forward, and was also involved in our first experimental work in MBL. I also acknowledge Dan Stamper-Kurn, for his engagement in our group meetings and many stimulating discussions during his stay in Germany.

I continue by thanking the staff of the *AG-Bloch* group. I would like to start by thanking Kristina Schuldt as well as Doreen Seidl, for all their work concerning contract updates, organization of internal workshops and many other efforts to make our experience in the group better. I also thank Ildiko Kecskesi, for making all LMU matters easier, and especially in these last steps of the PhD, by organizing (twice) the date for my PhD defense, and providing guidance of all the necessary steps. También quiero agredecer a Sonya Gzyl por todo su esfuerzo en la coordinación del IMPRS QST, sobretodo su apoyo para organizar el ICFO-IMPRS workshop en Castelldefels,

que fue una gran experiencia. In the technical side, I am most grateful to Karsten Förster. The high isolation of our quantum systems stems from the low-noise PID stabilization, for which Karsten was fundamental. I also want to thank Bodo Hecker, Anton Mayer and Olivia Mödl for their patience and help.

I would like to thank all the members of the team in MPQ for both a great time together as well as many scientific discussions. I want to mention André Heinz, Annie Jihyun Park, Lorenzo Festa, Jayadev Vijayan and Niko Lorenz, with whom I shared most time as a PhD student, and master students Nejc Janša, Rodrigo González Escudero, Scott Eustice, Stephan Wissenberg and Anne-Sophie Walter. I also acknowledge many useful discussions with Guillaume Salomon, Ahmed Omran and Christoph Gohle. In the LMU side (aside from those great GoT evenings), I am grateful for many useful scientific discussions, in particular to Sebastian Scherg, Karen Wintersperger, Pranjal Bordia, Christian Schweizer, Simon Fölling and Monika Aidelsburger. Outside of the *Bloch* group, I also want to thank Fabian Schmid and Severin Daiß, with whom I shared my time as a PhD representative in MPQ. Y quiero también dar las gracias a Juan Ignacio Cirac por su interés en nuestros proyectos, y por hacer posible que les diera un labtour a la audiencia de *La 2*.

In my time outside of the institute, I have been able to explore the city of Munich with many amazing people. The list is way too long, but I want to mention Xabi, Mathilde, Anna, Jessica, Josué, Arianna, Leticia and Marta. I also kept meeting here and there some of the closest friends I met in Zürich. Thank you Maud, Yolanda, Rahel, Alessandro, and Katrin. I evidentment, vull donar les gràcies a les meves amigues i amics de Barcelona, amb qui he seguit compartint grans moments aquests últims anys. Especialment a tots amb els qui he compartit alguna (e)tapa d'*el Camino* (que encara he d'acabar), i als que m'heu visitat aquí durant el doctorat: Alba, Popep, Marc, Gemma, Elis, Judit i Laura. Ens veiem molt aviat.

Deep in the third page of acknowledgments, it's about time for me to thank Sarah Hirthe for many, many things. I have enjoyed a lot these last years by your side (learning *a lot* about world history, gastronomy and even how to drive from you), and I want to especially thank you for you moral and scientific support towards the last part of the thesis. After long days in MPQ, you listened to my struggles in the lab and suggested useful ideas. I am writing these lines because you made it possible!

Finalment, com no podia ser d'altra manera, vull acabar donant les gràcies a la meva família, que m'ha acompanyat durant aquests últims 6 anys a l'estranger. A les meves dues germanes, Cristina i Elena, i a la resta de la família (amb noves incorporacions): Abel, Anna, Csaba, Júlia, Leo, Marc i Ramon. Per últim, agraïr als meus pares, Antonio i Cristina, per tot el suport que he rebut aquests anys, i per acollir-me a Rosés cada vegada que he tornat. Moltes gràcies.